UMCS

MARII CURIE SKŁODOWSKA UNIVERSITY
IN LUBLIN

Doctoral School of Quantitative and Natural Sciences

Scientific field: Physics
Discipline: Nuclear Physics

José Marín Blanco
nr album: 300127

Study of Spontaneous Fission of Actinide and Super-Heavy Elements

Doctoral dissertation prepared under the scientific supervision of
Auxiliary supervisor: **dr hab. Artur Dobrowolski**

LUBLIN, 30 September 2023

Acknowledgements

After 4 years of work on this project, there are undoubtedly countless people without whom it would have been impossible to carry it out or would have been infinitely more difficult.

The day-to-day work would often not have been possible without the help and advice of so many colleagues such as Bartłomiej Baran, Bartłomiej Kiciek, Szczepan Głodzik, Irene Dedes, Anna Zdeb, Anna Wielgus, Piotr Mendel and Pavel Kostriukov.

I also express my thanks for their lessons and patience to the professors in the department Michał Warda, Nicholas Sedlmayr, Karol Wysokiński, Bożena Pomorska and Tadeus Domański.

And finally to the three people with whom I have worked and collaborated most closely without whose contribution this project would not have been possible Johann Bartel, Krzysztof Pomorski and my supervisor and friend Artur Dobrowolski.

Lublin, September 2023   José Marín Blanco

Abstract

The thesis is devoted to a theoretical description of the nuclear fission phenomenon. Apart from an extended review of theoretical models used by the author, it contains essential estimates of fundamental parameters that decide the occurrence of fission. The macroscopic, microscopic nuclear energy model is used to predict the ground and isomeric state energies, fission barrier heights, and fission paths leading to fission.

The Lublin-Strasbourg drop was used to evaluate the macroscopic part of the energy, and the microscopic energy correction was obtained using the Strutinsky shell correction method and the BCS formalism. The Yukawa-folded mean-field potential was used to describe the single-particle structure of nuclei. An extended calculation of the potential energy surfaces (PES) in the up-to-date 4D Fourier shape parametrization is performed for 261 even-even nuclei with the proton numbers from Z=90 to 120, taking into account the deformation parameters describing the elongation of a nucleus, left-right mass asymmetry, neck shape and the nonaxiality. The calculation is made in two steps. The first one evaluated the PES for actinide nuclei using a universal expression for the pairing strength, which describes the average properties of nuclei from different mass regions. Using the equilibrium deformations of nuclei obtained in this calculation, we have refitted the pairing strength to the experimental mass difference of the actinide nuclei. This new local fit of the pairing strength used in the second-step calculations allows for a more precise description of the properties of the heavy and super-heavy nuclei.

The PES analysis results are presented in several tables and are used for the spontaneous fission lifetimes. The fission barrier's penetration probability was estimated in the multidimensional WKB approximation using the irrotational-flow estimate of the inertia tensor. The most probable paths for fission in the 4D space are found within a variational calculation based on the Fourier expansion of the fission path. Obtained in such a way estimates of the spontaneous fission half-lives and the barrier heights are close to existing experimental data, which is a good sign for the predictive power of our model. Such calculations are essential to estimate and predict the stability of unknown isotopes, including the region of super-heavy nuclei.

Keywords – Nuclear fission, fission half-lives, potential energy surfaces, fission barrier,

pairing correlations, shell correction, least action path, nuclear deformation.

Contents

List of Figures

List of Tables

1   Introduction

Nuclear fission is a process that has been known and used for decades, but the global energy crisis of the last year, as well as the issue of climate change, has brought the importance of recovering fission energy as a source of energy back into the spotlight, both from the point of view of energy security for countries, reducing their dependence on other countries for raw materials, and for environmental protection and reducing emissions of gases that contribute to the greenhouse effect. Also related to the possible uses of fission is the synthesis of new elements and isotopes within the rare earths that are essential in industry today. Rare earths are of vital importance for technological advances and industry that have a direct impact on our lives. The discovery of new elements thanks to controlled fission processes opens the way to obtaining new elements with new physical properties, which would represent a new step in progress.

Obviously, these topics are totally beyond the scope of this work, but they serve to help highlight the enormous importance of work like this based on the nuclear fission process that facilitates a better understanding of the physics of this process, which supports the implementation of new and better processes for obtaining energy, as well as new elements or isotopes with innumerable applications in industry and everyday life. This shows that the advancement and understanding of the fission process is of fundamental importance today more than ever.

There are several competing decay modes, such as α particle, γ quanta, neutron, proton or light cluster emission, but nuclear fission is one of the most interesting decays for the description of the stability of heavy and superheavy nuclei. In 1938, nuclear fission induced by neutron bombardment was observed for the first time in an experiment performed by Hahn and Strassman (1). The theoretical explanation for this newly discovered phenomenon came a few weeks later from Meitner and Frisch (2), they introduced the idea of the low-energy fission process, in which the energy released in this fission process would be approximately 200 MeV and it origins mostly from the Coulomb repulsion of the produced fragments. In addition, the authors estimated that the number of neutrons emitted in each nuclear fission process was greater than one, so it would be possible that a chain process of further fission could be created. A year and a half later, Flerov and

Petrzak discovered the spontaneous fission of uranium (3).

Since those early years, there has been great interest in physics in the process of spontaneous fission. A first description was based on the theoretical model of the nucleus in which it is likened to a charged liquid droplet, and fission would be a collective motion of the constituent particles in which the nucleus would deform in a process of evolution from a shape close to a sphere to a new elongated shape (4). Thus, the deformation of the nucleus shape is in turn related to the evolution of the nuclear energy, which increases as the deformation increases. When the elongation of the nucleus exceeds a certain limit, the energy decreases again and the nucleus breaks into two separate fragments. This fission process it can be explained by quantum mechanics, as a tunneling process through a potential energy barrier. The shape of the fission barrier, both the height and the width, has an enormous influence on the tunneling probability and thus also on the spontaneous fission half-life.

In recent years, several models have been proposed to describe the fission process and to predict more accurately the spontaneous fission half-lives. What must be taken into account for a good quality descriptive fission model is that a small change in the energy barrier, especially in its height, will have a large impact on the prediction of the fission half-life. One of the most successful models with a global scope in its description of spontaneous fission half-lives was the semi-empirical formula proposed by W.J. Świątecki in 1955 (5).

The most important idea of this model comes from the large correlation observed between the logarithm of the spontaneous fission half-lives and the microscopic corrections of the ground state energy due to the shell effects and the pairing corrections. Updates were added to this early nuclear model based on experimental results (6; 7) and implemented in a more modern and improved version of the liquid drop model, which is now known as the Lublin-Strasbourg Drop (LSD) model (8). To this model can also be added several attempts to apply fully microscopic and self-consistent methods to describe experimental observations of spontaneous fission (9; 10), but the accuracy in reproducing these experimental results is not yet fully satisfactory.

For a description closer to the experimental results, one can also take into account the pairing between particles as a dynamical degree of freedom (see Refs. (11; 12)), it is

also useful to use some of the improvements for the collective inertia (13), but these approximations are numerically computationally expensive. In general, spontaneous fission half-life calculations require not only a description of the collective potential energy surface (a macroscopic-microscopic model will be used in this work), but also of the collective inertia tensor.

The collective inertia tensor may be obtained using the cranking approximation (14; 15) or the Generator Coordinate Method (GCM) with the generalized Gaussian Overlap Approximation (GOA) (16; 17). In this study the irrotational-flow approach of Ref. (18) (see also (19)) will be use to calculate the inertia tensor.

This work will be devoted to present predictions of the spontaneous fission half-lives, obtained within that approach, and their comparison with experimental data.

In this manuscript, we have used the tunneling model in the WKB approximation though a multidimensional potential-energy barrier (20; 21; 22). A study will be made on the half-lives for even-even actinide and super-heavy nuclei from $Z = 90$ to 110. Thus, listing these nuclei with their corresponding isotopes within the actinides: Th, U, Pu, Cm, Cf, Fm and No; and within the super-heavy elements: Rf, Sg, Hs, and Ds.

The theoretical framework of our approach will be based on the parametrization of the nuclear shape, the macroscopic-microscopic approach with the Lublin-Strasbourg Drop model is used to describe the energy of the nuclear system from the ground state to the scission as a function of the deformation parameters.

Prior to the calculations of the spontaneous fission half-lives, an improvement step has been made in the way of calculating the pairing corrections. Namely, the average strength of the pairing force G was adjusted to the experimental energy gap values δ evaluated using the mass table (23) as described in Chapter 6.

These theoretical results on half-life predictions are compared with the corresponding available experimental data. Since the theoretical results obtained have been quite close to the experimental ones, half-life predictions have also been made for nuclei for which experimental data are not yet available.

Before embarking on the results and their interpretations, we include in this work a theoretical introduction, the theory on which all calculations and results of this work will

be based.

To understand the fission process, a comprehensive approach to the whole process is necessary, a description of the physical form of the nucleus and its evolution from its lowest energy and therefore most stable state to the final fission break-up. During the fission process, the nucleus goes through multiple intermediate states, where the nucleus deforms towards an elongation in which the formation of two distinct parts joined by a narrow neck can be seen until a certain critical limit is reached where the nucleus breaks into two new fragments.

For the description of the shape of the nucleus and its evolution, we have made use of the Fourier parametrization, restricting the possible deformation parameters to 4, which would be the nonaxiality, the elongation, the left-right mass asymmetry, and the parameter which corresponds nearly to the width of the neck between the two fragments before they separate. More higher rank deformation parameters could be used, but this would imply a very high increase in the number of variables, increases the computational burden and make the analyses much more complicated and involved. As we will see later in this work, restricting the dimensions to the 4 dimensions mentioned above satisfies a compromise between an adequate and sufficient physical description of the shape of the nucleus and the computational load. This description of the nucleus shape will be dealt with in Chapter 3 of this thesis.

Also, the shape of non-spherical nuclei in their ground state and their deformation will be discussed in Chapter 7.

In addition to the shape evolution of the nucleus, we must study the changes in the energy of the nucleus, since it is this energy that governs and drives the whole fission process. For this energy description, we have used the macroscopic Liquid Drop Model with some improvements implemented in the Lublin-Strasbourg Drop (LSD) formula described in Chapter 2.

The energy barriers that must be overcome to reach fission are described in Chapter 4. From the ground state to fission, the nucleus goes through different energy changes, and it is the differences between the highest energy points and the lowest energy points that give us the energy barriers that the nucleus must overcome to reach fission.

For a more refined description of the energy than that obtained with the macroscopic LSD model, we add some quantum-mechanical energy corrections expressed by the microscopic energy which is the sum of the shell correction energy evaluated using the Strutinsky prescription and the pairing energy estimated using the BCS approximation, as shown in Chapters 6 and 8.

After this important theoretical introduction, we move on to the results.

In Chapter 9, we show the results obtained on the evolution of the energy from the ground state to fission, passing through the saddle points in the multidimensional potential energy surfaces (PES). The difference between the maximum and minimum energies is used to calculate the barrier heights.

In Chapter 10, we search for an improvement in the pairing correction, comparing with experimental data, a general improvement in the description of the energies of the isotopes studied can be seen. After this improvement of the pairing correction, we have recalculated the isotope energies, which are shown in the maps and graphs in Chapter 11.

Using the results of the calculated energies, the half-lives of the spontaneous fission of the actinide and the super-heavy nuclei have been estimated using the multidimensional WKB method. The predicted values of these half-lives are shown in Chapter 12.

In Chapter 13, we recalculate the potential energy surfaces (PES) of the nuclei selected odd-even nuclei with the charge number $Z \geq 89$.

This has been the work of 4 years with thousands of calculations, repetitions, corrections and recalculations always with the same goal: to find the closest and most realistic description of the spontaneous fission process.

2 Liquid Drop Model

The Liquid Drop Model (LDM), since its first proposal by George Gamow in 1930 and later developed by Niels Bohr and John Archibald Wheeler, has evolved and improved over time, with special milestones that we will review.

It is assumed that the nucleus is composed of an incomprehensible fluid, which assumption is the opposite to the Fermi's gas model. Although this model is an early approximation and does not explain all fine details, it is a model that does manage to explain many important features of the nucleus.

This nuclear charged liquid drop is composed of protons and neutrons. Its density is approximately constant and does not depend on the mass number as the nuclear radius is proportional to the number of nucleons. Moreover, as the nucleus is composed of individual nucleons, an extraordinary peculiarity is that the sum of the masses of the individual nucleons is larger than the sum of the nucleus composed of the same nucleons, which has been called the mass defect, the energy equivalent of this "lost" mass difference being the binding energy between the nucleons:

$$\Delta M(N, Z) = N M_n + Z M_H - M(N, Z) \tag{2.1}$$

Where M_n and M_H are the masses of neutron and Hydrogen atom respectively while N and Z are the neutron and proton numbers. Note that $\Delta M > 0$. The mass defect provides the binding energy of the system:

$$B(N, Z) = \Delta M(N, Z) c^2 \tag{2.2}$$

In the following graph 2.1, we can see the binding energies per nucleon as a function of mass number A:

We can establish that the maximum value of B/A is $8.8 MeV$ in $A \approx 70$. For the heaviest known nucleus, $A \approx 250$, the binding energy is approximately $7.5 MeV$. The LDM reproduces well the average binding energy on nuclei from the lightest ones to the super-heavy nuclei.
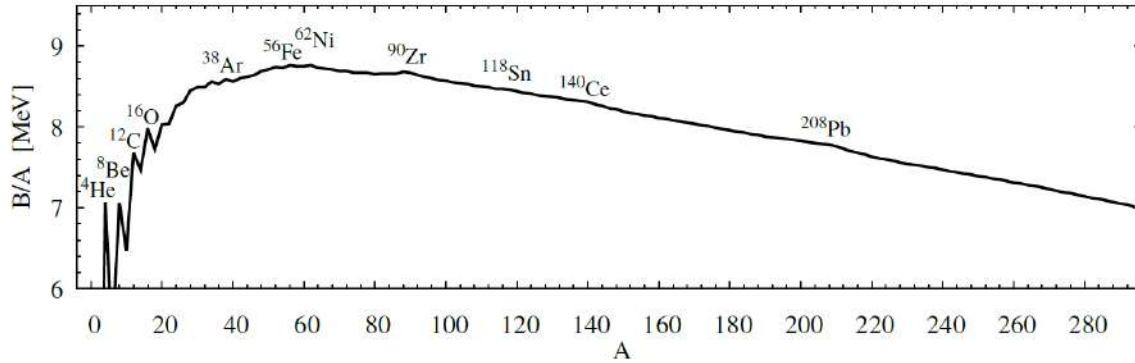
Figure 2.1: Nuclear binding energy per nucleon as a function of mass number A.

Despite the high binding energy, the existence of an energy difference of $1MeV$ between $A \approx 100$ and $A \approx 240$, points to a break-up of the heavy nuclei into two lighter ones. The energy released in a fission process is approximately 1/1000 of the mass of the nucleus.

If we consider the energy released in the fission of $1Kg$ of Uranium:

$$E = 10^{-3}kg \cdot (3 \cdot 10^8 m/s)^2 = 9 \cdot 10^{13} J \qquad (2.3)$$

We see that $1kg$ of uranium is equivalent to approximately 1000 tonnes of coal.

Having seen the origin of the binding energy, let us now look at the properties of nuclear interaction deduced from by the above model:

1. Strong: the binding energy is expressed in MeV.

2. Attractive: the distance between nucleons is larger than their size $(r \geq 1fm)$

3. Strongly repulsive: occurs when the nucleons come to closely.

4. Short range: disappearing for $r \geq 2fm$

5. Charge invariant: the nuclear interaction is the same for p-p, n-n, and n-p.

6. Depend mostly on the with the distance between nucleons: $(V_{12} = V(|\vec{r}_{12}|))$.

The first semi-empirical expression was proposed by Bethe and Weizsäcker (24) (25), where only three parameters to the binding energy are considered:

$$B = a_{vol}A - a_{surf}A^{2/3} + E_{Coul} \qquad (2.4)$$

where the constant nuclear energy per nucleon is described as approximately $8MeV$. Although the total energy decreases due to the fact that closer to the surface of the nucleus there are fewer bound nucleons as there are no nucleons outside the nucleus, and those on the surface only have binding forces inside the nucleus, which is described by the minus sign in the surface part of the equation, this fact is related to the surface tension of a liquid drop. In addition, the Coulomb repulsion of the protons must be taken into account.

In the equation, we have a part proportional to the nucleon number $A = N + Z$ describing the volume contributions to the binding energy, while the term proportional to $A^{2/3}$ describes the effect of reducing the binding energy due to surface tension.

This first approach to the description of the binding energy of the nucleus would have a long road of improvement. One of them was proposed in 1953 by Green and Bethe, which took into account the isospin symmetry like a similar term in the Fermi gas model (26), which presupposes that due to the Pauli principle and the conservation of momentum and energy, fermions can be considered as particles which move independently of each other.

The isospin symmetry energy would be proportional to the nuclear reduced isospin defined as $I = \frac{N-Z}{A}$. This term expresses the dependence of the energy on the unequal number of protons and neutrons in the nucleus.

A decade and a half later, in 1967, Myers and Swiatecki improved the equation by taking into account not only the isospin dependence of the volume and surface terms but also the effect of the diffusivity of the charge distribution which decreases slightly of the Coulomb interaction (27). The most important aspect of this new improvement is the incorporation of the dependence of the deformation on the binding energy into the model. This is achieved by adding the deformation dependence of the surface B_{surf} and the Coulomb energy B_{Coul}, leaving the equation for the binding energy as follows:

$$B(A, Z, def) = a_{vol}(1 - \kappa_{vol}I^2)A - a_{surf}(1 - \kappa_{surf}I^2)A^{2/3}B_{surf}+$$
$$+\frac{3}{5}\frac{e^2 Z^2}{r_0^{ch} A^{1/3}}B_{Coul} - \frac{C_4 Z^2}{A}, \tag{2.5}$$

where $B_{surf} = \frac{S(def)}{4/3\pi R_0^3}$ is the ratio of the surface area of the deformed drop to the surface area of another spherical drop of equal volume and $B_{Coul} = \frac{E_{Coul}(def)}{E_{Coul}(sph)}$ describes the relative change of the Coulomb energy. The parameters a_{vol}, κ_{vol}, a_{surf}, $K\kappa_{surf}$, r_0 and C_4 were adjusted using the experimental masses of 1200 nuclei measured so far.

As can be seen, the functions B_{surf} and B_{Coul} depend on the classical deformation of the drop which can be described by a set of deformation parameters that will be discussed in the next chapters.

To make a short historical review of the evolution of the Liquid Drop Model, we will briefly mention the Droplet Model. The Droplet Model (DM) gives to the previous liquid drop model some important improvements, it manages to describe the effect of the surface curvature and the deviation of the nuclear density from its constant value assumed in the liquid drop model. Now, with the DM, the surface area term of the equation is no longer proportional to $I^2 A^{2/3}$ like it is in the LDM, eq. 2.5 but achieves a more exact description, since the increase in nuclear energy is also due to the excess of neutrons displaced to the surface of the nucleus. This DM would reflect the fact of a not entirely equal distribution between protons and neutrons. For the description of this model, we will introduce some new parameters:

1. t: thickness of the neutron skin,

2. δ: relative excess of the neutron density,

3. ϵ: relative deviation of the density from its nuclear mater value ρ_0,

4. Σ: the effective nuclear surface situated between proton and neutron distributions.

To neutralize the repulsion between protons, the heavy nuclei have a larger number of neutrons than protons ($N > Z$), but these excess neutrons are expelled from the inner region, moving towards the nuclear surface, forming an outer layer, which is called the neutron skin, so that symmetry in the number of protons and neutrons remains in the inner region of the nucleus.

The repulsive forces of the protons due to the electric charge pull them apart, bringing them closer to the surface, and compensating for the previous effect of the symmetry. Taking into account these two counteracting effects, the neutron skin can be understood

as the distance t between the positions of the diffuse proton and neutron profiles, or in other words, the displacement needed to place one profile on top of the other. This results in an enrichment of the neutron surface layer, but with some admixture of protons.

Thus, the force responsible for the formation of this surface neutron skin can be expressed by:

$$t = \frac{3}{2} r_0 JI/Q \ , \tag{2.6}$$

where r_0 is the nuclear radius constant, J the nuclear symmetry energy coefficient and Q the effective surface stiffness coefficient.

Coulomb energy of protons defined as $c_1 Z^2/A^{1/3}$, where $c_1 = 3e^2/5r_0 \approx 0.7322 MeV$, decreases the force JI, which modifies the distance t, which is as follows:

$$t = \frac{3}{2} r_0 \frac{JI - \frac{1}{12} c_1 Z A^{-1/3}}{Q}. \tag{2.7}$$

Further considerations lead to the modification of the denominator:

$$t = \frac{3}{2} r_0 \frac{JI - \frac{1}{12} c_1 Z A^{-1/3}}{Q + \frac{9}{4} J A^{-1/3}}. \tag{2.8}$$

We present a modification of the above equation that better reproduces the fact that when a nucleus of net charge 0, all the excess neutrons are displaced towards the surface $(t \longrightarrow t_{max} = 2/3R_0 I)$. For a nucleus of arbitrary shape, the equation for t has the form $t = \widetilde{t} + \bar{t}$, where

$$\bar{t} = \frac{3}{2} r_0 \frac{JI - \frac{1}{12} c_1 Z A^{-1/3}(B_{vol}/B_{surf})}{Q + \frac{9}{4} J A^{-1/3} B_{surf}}, \tag{2.9}$$

and $\widetilde{t} = \frac{3}{8} r_0 \frac{e}{Q}(\widetilde{v}_s - \overline{\widetilde{v}})$. Here $\widetilde{v}$ is the deviation of the electrostatic potential v generated by the uniform charge distribution Ze, while $\widetilde{v}_s$ is the value of $\widetilde{v}$ on the surface and $\overline{\widetilde{v}}$ is the surface average of $\widetilde{v}_s$.

Taking all these factors into account, the macroscopic binding energy of the Droplet Model is (28):

$$B(A, Z, def) = (-a_1 + J\overline{\delta}^2 - \frac{1}{2}K\overline{\epsilon}^2 + \frac{1}{2}M\overline{\delta}^4)A + (a_2 + \frac{9}{4}\frac{J^2}{Q}\overline{\delta^2})A^{2/3}B_{surf} +$$

$$+a_3A^{1/3}B_{curv} + +c_1Z^2A^{-1/3}B_{Coul} - c_2Z^2A^{1/3}B_r(def) - c_5Z^2B_w(def) - \quad (2.10)$$

$$-\frac{c_3Z^2}{A} - \frac{c_4Z}{\sqrt[3]{2}} + E_{Wig} ,$$

where B_{Coul}, B_{surf} and B_{curv} are functions representing the deformation dependencies of the electromagnetic, surface, and curvature energies. The parameters $B_r(def)$ and $B_w(def)$ correspond respectively to the inhomogeneous charge distribution inside the nucleus and on its surface. The Wigner term E_{wig} is assumed in the following form (29):

$$E_{Wig}(A, Z) = -10MeV \cdot \exp(-42|I|/10) . \quad (2.11)$$

The variables $\overline{\delta}$ and $\overline{\epsilon}$ are the average δ and ϵ over the effective surface Σ and they are equal to:

$$\overline{\delta} = \frac{I + \frac{3}{16}\frac{c_1}{Q}ZA^{2/3}f(def)}{1 + \frac{9}{4}\frac{J}{Q}A^{-1/3}B_{surf}} \quad (2.12)$$

and

$$\overline{\epsilon} = \frac{1}{K}[-2a_2A^{-1/3}f(def) + L\overline{\delta^2} + C_1Z^2A^{-4/3}g(def)] . \quad (2.13)$$

The coefficients c_i are:

$$c_1 = \frac{3}{5}\frac{e^2}{r_0} = 0.73531 ,$$

$$c_2 = \frac{c_1^2}{336}(\frac{1}{J} + \frac{18}{K}) = 0.00016477 ,$$

$$c_3 = \frac{5}{2}c_1(\frac{b}{r_0}) = 1.30501 , \quad (2.14)$$

$$c_4 = \frac{5}{4}(\frac{3}{2\pi})^{2/3} = 0.56149 ,$$

$$c_5 = \frac{1}{64}\frac{c_1^2}{Q} = 0.00049695 .$$

And the rest of the DM coefficients have the following values:

$$a_2 = 20.69 MeV$$
$$K = 240.0 MeV$$
$$L = 100.0 MeV$$
$$r_0 = 1.18 fm$$
$$J = 36.8 MeV \tag{2.15}$$
$$Q = 17.0 MeV$$
$$e^2 = 1.44 MeV \cdot fm$$
$$b = 1.0 fm$$

The above 9 parameters of the Droplet model were adjusted to the experimental masses and fission barriers of nuclei known at the time.

The next model to be considered, the Lublin-Strasbourg Drop (LSD), combines the most significant features of these previous models, the Liquid Drop Model and the Droplet Model.

2.1   Lublin-Strasbourg Drop (LSD) model

This model is an improvement over the Liquid Drop Model in which one takes into account the nuclear curvature term proportional to $A^{1/3}$ (30). The parameters of the LSD model were adjusted to the binding energies of 2766 nuclei, known at that time. No fitting was performed to the experimental fission barrier heights.

Although the Liquid Drop model obtained fairly good results, the introduction of the surface curvature term was an important correction. For example, the new r.m.s. deviation $< \delta M >= 0.698 MeV$, slightly lower than the value obtained with the previous model of $< \delta M >= 0.732 MeV$. Also with the LSD model, the new fission barrier deflection r.m.s. for nuclei with $Z > 70$ is $< \delta V_B >= 0.698 MeV$ compared to the previous value $< \delta M >= 5.58 MeV$.

A previous step towards LSD, where the curvature term was already taken into account, was the liquid drop model proposed by Myers and Swiatecki (MS-LD) (27). With this

model, it is possible to reproduce the values of the nuclear masses, but for light nuclei, the model overestimates the heights of the fission barriers by up to $10 MeV$. The MS-LD barriers are also higher than those obtained by Sierk (31) using the macroscopic Yukawa-folded model.

We can express the Lublin-Strasbourg Drop (LSD) with the following formula for the binding energy (32):

$$
\begin{aligned}
B(Z, N, def) = a_{vol}(1 - \kappa_{vol}I^2)A - a_{surf}(1 - \kappa_{surf}I^2)A^{2/3}B_{surf}(def) + \\
+ a_{cur}(1 - \kappa_{cur}I^2)A^{1/3}B_{cur}(def) + \frac{3}{5}\frac{e^2 Z^2}{r_0^{ch}A^{1/3}}B_{Coul}(def) - C_4\frac{Z^2}{A} - E_{congr},
\end{aligned}
\tag{2.16}
$$

where $B_{surf}(def)$, $B_{cur}(def)$ and $B_{Coul}(def)$ have been calculated from the Funny-Hills parameters.

The following parameters of the LSD formula have been fitted with the binding energies of 2766 nuclei known experimentally so far from the tables (33), also introducing microscopic corrections from (34) and the estimated congruence energy E_{congr} from (35):

Table 2.1: Parameters of the LSD model.

$a_{vol} = -15.492$ MeV	$\kappa_{vol} = 1.8601$
$a_{surf} = 16.9707$ MeV	$\kappa_{surf} = 2.2938$
$a_{cur} = 3.8602$ MeV	$\kappa_{cur} = -2.3764$
$r_0^{ch} = 1.21725$ fm	$C_4 = 0.9181$ MeV

3   Description of nuclear shape parametrization

In the study of nuclear reactions (fusion, fission, rotations, collective vibrations or reactions with heavy ions) it is very important to describe accurately of the shape of the nucleus. Also, the nucleus shape variance when the reaction evolves dramatically influence the energy of the nucleus, which is what will ultimately govern and guide any process in the nucleus.

In order to get a description of the shape of the nuclear surface, a parametrization that meets a number of conditions is used:

1. A good description of the shape of the nucleus, especially along the fission path,

2. Simple to calculate,

3. Flexible with changes of the number of deformation parameters.

One of the parametrizations that has been a kind of reference for more than 30 years due to its correct description of the nuclear form and its relative simplicity is the so-called "Funny-Hills" (36).

3.1   The Funny-Hills parametrization (FH)

Proposed more than 50 years ago, in 1972 (36), it was a very simple mathematical form, especially useful in the description of the fission process, without losing a great simplicity that facilitates the calculations of the shape during the evolution of the reaction.

$$\rho_s^2(u) = R_0^2 c^2 (1 - u^2)(A + \alpha u + B u^2) \ , \tag{3.1}$$

where $\rho_s(u)$ is the distance from the symmetry axis (z-axis) to the nuclear surface. The left and right-hand "tips" of the nucleus are placed at $z_{min} = -z_0 + zsh$ and $z_{max} = z_0 + zsh$, respectively. Here $z_0 = cR_0$ is the half-length of the nucleus. The parameter z_{sh} is the shift of the z coordinate which holds that the center of mass of the nucleus always remains at $z = 0$.

The dimensionless coordinate u is defined as follows:

$$u = \frac{z - z_{sh}}{z_0} \ .$$

(3.2)

Although the shape of the nucleus may vary, the volume of the nucleus is considered to remain constant at all times, whether it is spherical or any other shape, so we can consider:

$$V = \frac{4\pi}{3} R_0^3 = \int_0^{2\pi} d\psi \int_{z_{min}}^{z_{max}} dz \int_0^{\rho_s(z)} \rho \, d\rho =$$
$$= z_0 c^2 R_0^2 \pi \int_{-1}^1 (1 - u^2)(A + \alpha u + Bu^2) \, du,$$

(3.3)

This volume conservation condition leads to the relation:

$$c = (A + \frac{1}{5}B)^{-1/3} \ .$$

(3.4)

This parameter c is the nuclear elongation in units of the radius R_0 of the spherical nucleus of the same volume.

If we take into account that the center of masses stays at $z = 0$:

$$z_{cm} = \frac{2\pi \int_{z_{min}}^{z_{max}} \rho_s^2(z) z \, dz}{2\pi \int_{z_{min}}^{z_{max}} \rho_s^2(z) \, dz} = \frac{R_0 c \int_{-1}^1 (1 - u^2)(A + \alpha u + Bu^2) u \, du}{\int_{-1}^1 (1 - u^2)(A + \alpha u + Bu^2) \, du} = 0 \ ,$$

(3.5)

we can calculate the value of z_{sh}:

$$z_{sh} = -\frac{1}{5}\alpha c^3 z_0 \ .$$

(3.6)

There are two parameters that have a great contribution in the Funny-Hills parametric description, which are the elongation parameter c and the neck parameter h, which measures the thickness of the part that joins the two regions of the nucleus when it starts to separate on its way to fission and could be defined as the neck. With these two parameters, one can define the deformation parameter h:

$$B = 2h + \frac{1}{2}(c - 1)$$

(3.7)

In the Funny-hills parametrization, $h = 0$ corresponds roughly to the LD path to fission.

The parameter A in Eq. (3.1) can be easily expressed by c and h

$$A = \frac{1}{c^3} - \frac{1}{10}(c-1) - \frac{2}{5}h ,$$

(3.8)

which play a role in the fundamental deformation parameters in the Funny Hills classes of shapes.

All allowed Funny Hills shapes correspond to $\rho_s^2 < 0$ which gives certain limits for possible values of c and h. In addition, in order to also describe the diamond-like shapes that have some actinide nuclei in the ground state, an analytical variation has been proposed for negative values of the B parameter, so that we can separate the Funny Hills description into two:

$$\rho_s^2(u) = \begin{cases} R_0^2 c^2 (1-u^2)(A + \alpha u + B u^2) & , B \geq 0 \\ R_0^2 c^2 (1-u^2)(A + \alpha u) exp(Bc^3 u^2) & , B < 0 \end{cases}$$

(3.9)

For a uniform density distribution we can find the multipole moments are the following integral:

$$Q_{n0} = \frac{2}{R_0^3} \int \rho_0(\vec{r}) r^n P_n(x) \, d^3x,$$

(3.10)

where $\rho_0(\vec{r})$ is the nuclear density distribution. The variable x is calculated as $x = \rho_s/\sqrt{\rho_s^2 + z^2}$, $\rho_s^2 = x^2 + y^2$ and $P_n(x)$ is the nth order Legendre polynomial of x.

3.1.1   The Modified Funny-Hills parametrization

We can also see a new variant of the Funny Hills parametrization, the Modified Funny-Hills parametrization, the symmetric shape parameter with a Gaussian neck is introduced. By using cylindrical coordinates, it is possible to simplify and achieve a small number of degrees of deformation of the nucleus relevant to the system under study. In this way, a correct description of the nuclear fission process is achieved, as well as the energy barriers of the process. For the cases of actinide elements, a high number of octupole, hexadecapole, even up to a multipolarity deformation degree of 14, are used. But these extremes with so many multipolarity degrees have a major drawback, which is the enormous computational burden of calculation required, which forces to take into account only the multipolarity

deformations that are most relevant for a correct description of the fission process. For each degree of freedom of deformation, a mesh of at least 20 points must be considered. If, for example, we only consider a 4-dimensional deformation, the total number of points to consider in this case would be at least $N_g = 20^4 = 1.6 \cdot 10^5$, for the case of a 5-dimensional space it would be $N_g = 3.2 \cdot 10^6$.

It is not our aim to use a new parametrization, but to try to improve the existing ones and to avoid some common problems, also to try to minimize the average liquid drop energy on its way to fission.

Taking all this into account, this modification of the Funny Hills Parametrization can be defined with the following formula:

$$\rho_s^2(z) = 1 - \frac{R_0^2}{cf(a,B)}(1-u^2)(1+\alpha u - Be^{-a^2 u^2}) \tag{3.11}$$

This formula will give a good approximation to the cases we will discuss. As in the previous parametrization, c also designates the nucleus elongation, B is the parameter describing the neck size, which becomes smaller as fission approaches, and, finally, $alpha$ describes the left-right mass asymmetry. The neck width parameter a is obtained from the minimization of the liquid drop energy along the fission path and has a value $a = 1$. The parameters z_0 and u are defined in two previous parametrization and the function $f(a, B)$ is defined as:

$$f(a, B) = 1 - \frac{3B}{4a^2}[e^{-a^2} + \sqrt{\pi}(a - \frac{1}{2a})\text{Erf}(a)] \ . \tag{3.12}$$

In this way, the necessary condition of conservation of the volume of the nucleus in any deformation situation is maintained.

It is helpful to use a new parameter h coming from the combination of B and c:

$$h = \frac{1}{2}[B - (c-1)] \ , \tag{3.13}$$

This new parameter will be designated as the neck parameter. When $h = 0$ in the limited deformation space $\{c, h\}$, it corresponds to the average of the liquid path to fission.

The shift of the z-coordinate z_{sh} is obtained as:

$$z_{sh} = -\frac{4}{15}\alpha z_0/f(a, B), \tag{3.14}$$

where the factor $f(a, B)$ is described above in Eq. (3.12).

The Modified Funny-Hills parametrization achieves a better description of the diamond-like shapes than the original version from which it starts, and this shape is important since it has many nuclei in its equilibrium state.

The main advantage of the Modified Funny-Hills parametrization over the original version is that no more than three-body non-physical shapes are obtained, for example, the case when $\rho_s^2(z) < 0$, which is physically impossible but was possible with the original Funny-Hills parametrization. The point of separation of the nucleus into two fragments happens when $z_{sc} = 0$, and that happens when $B = 1$ for the left-right symmetric shapes $\alpha = 0$ and

$$B \approx 1 - \frac{\alpha^2}{4a^2} \quad \text{at} \quad u_{sc} \approx \frac{-\alpha}{2B_{sc}} \ . \tag{3.15}$$

3.1.2   Axial shapes with Lorentzian neck

Let us discuss another variant of the FH parametrization in which is also possible to describe the shape of the nuclei in the fission process:

$$\rho_s^2(z) = R_0^2 c^2 (1 - u^2)(A + \alpha u + f(u)) \ , \tag{3.16}$$

where z and u are defined above, and

$$f(u) = \text{sign}(B)(1 - \frac{1}{1 + |B|u^2}). \tag{3.17}$$

The parameter c is the nucleus elongation parameter, B describes as before the neck formation and *alpha* corresponds to the left-right asymmetry. As above, it is useful to introduce the parameter h, a linear combination of c and B, which will be the neck parameter, of the form:

$$h = \frac{1}{2}B - \frac{1}{4}(c - 1) \ . \tag{3.18}$$

.

The case $h = 0$ corresponds to the average liquid drop path to fission. The volume conservation condition:

$$\frac{3}{4}\pi R_0^3 = 2\pi \int_{z_{min}}^{z_{max}} \rho_s^2(z)\, dz = 2\pi R_0^3 c^3 \int_{-1}^{1} (1-u^2)[A + \alpha u + f(u)]\, du \qquad (3.19)$$

with $z_{min} = -z_0 + Z_{sh}$ and $z_{max} = z_0 + Z_{sh}$ leads to the following expression for the parameter A:

$$A = \frac{1}{c^3} - \frac{3}{4}I \; , \qquad (3.20)$$

In this case, the value I is calculated:

$$I = \text{sign}(B) \int_{-1}^{1} (1 - \frac{1}{1+|B|u^2})(1-u^2)\, du =$$
$$= \text{sign}(B)[\frac{4}{3} - \frac{2}{\sqrt{|B|}}\arctan(\sqrt{|B|}) + 2\frac{\sqrt{|B|} - \arctan(\sqrt{|B|})}{\sqrt{|B|}^3}] \; . \qquad (3.21)$$

The shift z_{sh} can be obtained from the center of mass condition:

$$z_{cm} = \frac{2\pi \int_{z_{min}}^{z_{max}} \rho_s^2(z) z\, dz}{\int_{z_{min}}^{z_{max}} \rho_s^2(z)\, dz} = \frac{R_0 c \int_{z_{-1}^1}(1-u^2)(A+\alpha u + f(u))u\, du}{\int_{z_{-1}^1}(1-u^2)(A+\alpha u + f(u))\, du} = 0 \; , \qquad (3.22)$$

and it is equal to:

$$z_{sh} = -\frac{1}{5}\alpha c^3 z_0 \; . \qquad (3.23)$$

3.2 Fourier shape parametrization

There are a number of possibilities for the shapes that nuclei can take, such as oblate shapes in nuclei in the transition region, which correspond to the $p - f$ layers, as well as prolate deformations found in the rare-earth region. In addition, the highly elongated shapes and necked-in shapes that appear in fission processes must be taken into account. It is of vital importance to get models capable of describing all these shapes and fulfilling a number of constraints, they must be flexible and close to the shape they are meant to describe, but they must also be able to describe various deformation parameters as closely and realistically as possible.

An example of such a parametrization was the series expansion of the nuclear radius in spherical harmonics proposed by Lloyd Rayleigh in the 19th century, and this model is still one of the most widely used shape parametrization in nuclear structures today.

However, in fission processes, we find highly elongated shapes, for the description of which a large number of deformation parameters $\beta_{\lambda\mu}$ are necessary. For a correct description of the height barriers in the actinide region, at least 6-8 parameters are required, even when constraints to axial and left-right symmetry have already been applied.

But, the need to use so many parameters implies handling very high-dimensional functions in the attempt to get the stationary points in a multi-dimensional deformation space, so that the ground state, isomeric states, saddle points, valleys and ridges, points encountered on the way to fission, can be located.

Since Lord Rayleigh's model, many other shape parametrization have been proposed. Among these, some of the most successful have been the *quadratic surfaces of revolution*, the Cassini ovals, those seen above of the *Funny-Hills* shapes and their later variations, also important are the description of the expansion of the nuclear surface in a series of Legendre polynomials.

With all these shape parametrization it is possible to achieve a fairly good description of nuclear potential-energy surfaces, and with a reasonably small number of collective variables. But all these parametrizations have a common drawback, it is not possible to control their convergence. This drawback can be overcome by using a Fourier expansion of the nuclear surface in cylindrical coordinates. With this expansion, it is possible to quickly reach convergence and to describe correctly the nuclear ground states, as well as the very elongated shapes, which are found in the final stages of fission during the nucleus separation process.

In the following, the equation that represents axially symmetric shapes the square of the distance from the symmetry axis in cylindrical coordinates z to a point on the surface is represented by the Fourier series:

$$\frac{\rho_s^2(z)}{R_0^2} = \sum_{n=1}^{\infty}\left[a_{2n}\cos\left(\frac{(2n-1)\pi}{2}\frac{z-z_{sh}}{z_0}\right) + a_{2n+1}\sin\left(\frac{2n\pi}{2}\frac{z-z_{sh}}{z_0}\right)\right] . \qquad (3.24)$$

Here R_0 is the radius of the spherical shape associated with the nucleus with the same

volume. The nucleus length along the symmetry axis z is $2z_0 = 2cR_0$, with left and right ends located at $z_{min} = z_{sh} - z_0$ and $z_{max} = z_{sh} + z_0$, where $\rho_s^2(z) = 0$. The auxiliary parameter $c = z_0/R_0$ is the same elongation parameter that appeared in the Funny-Hills model, if $c < 1$ we are in the case of an oblate shape, if $c > 1$ it will be prolate. c is related to even Fourier deformation parameters by the volume conservation relation:

$$\frac{\pi}{3c} = \sum_{n=1}^{\infty} (-1)^{n-1} \frac{a_{2n}}{2n - 1} \tag{3.25}$$

Below is a schematic shape of a nucleus represented by the equation 3.24:
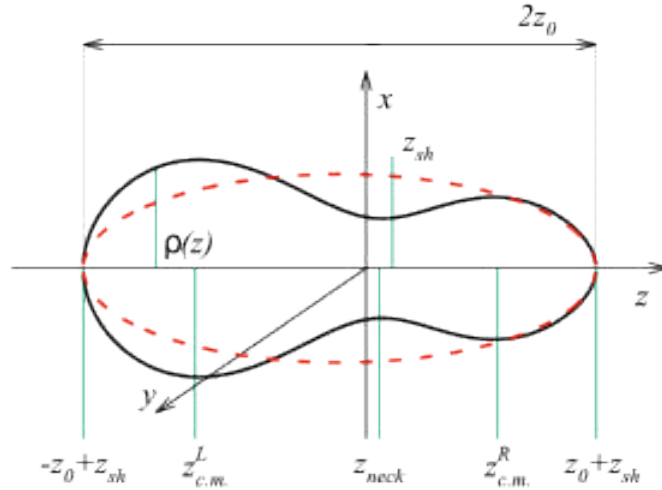
Figure 3.1: Schematic representation of a nuclear shape in cylindrical coordinates of the equation 3.24.

The displacement coordinate z_{sh} is defined so that the center of mass of the nucleus coincides with the origin of the coordinates system. The parameters a_2, a_3 and a_4 are, respectively, the quadrupole, hexadecapole and octupole deformation types, which in the fission process correspond also to the elongation, the left-right asymmetry and the neck thickness, respectively.

To describe the non-axial shapes, we must consider the assumption that the cross section

perpendicular to the symmetry $z-$axis can be considered to be ellipsoidal in shape, whereby the nonaxiality parameter is defined as:

$$\eta = \frac{b-a}{b+a}. \tag{3.26}$$

This parameter represents the relative difference of the semi-axis a and b of the cross section perpendicular to the symmetry axis. Since this parameter is the same all across the nuclear surface, the profile function can then be described in cylindrical coordinates:

$$\varrho_s^2(z,\phi) = \rho_s^2(z)\frac{1-\eta^2}{1+\eta^2+2\eta\cos(2\varphi)}, \tag{3.27}$$

where $\rho_s^2(z)$ is defined in Eq. 3.24.

Once the Fourier parametrization is defined, we can say that one of its advantages is fast convergence, even in the cases of highly deformed shapes. On the other hand, one of the drawbacks of this parametrization is the definition of the Fourier coefficients a_n, because unlike the Funny-Hills elongation parameter c, the Fourier coefficient a_2 decreases with increasing elongation. To solve this contradiction, new collective, "physical" coordinates will be introduced:

$$\begin{aligned}
q_2 &= \frac{a_2^{(0)}}{a_2} - \frac{a_2}{a_2^{(0)}} \\
q_3 &= a_3, \\
q_4 &= a_4 + \sqrt{\left(\frac{q_2}{9}\right)^2 + \left(a_4^{(0)}\right)^2} \\
q_5 &= a_5 - (q_2-2)\frac{a_3}{10} \\
q_6 &= a_6 + \sqrt{\left(\frac{q_2}{100}\right)^2 + \left(a_6^{(0)}\right)^2}
\end{aligned} \tag{3.28}$$

The newly introduced parameters $a_n^{(0)}$ are the Fourier coefficients for the spherical shape.

$$a_{2n}^{(0)} = (-1)^{n-1}32/[\pi(2n-1)]^3 \tag{3.29}$$

correspond to the values of the a_{2n}

These collectives q_n with $n > 2$ are close to zero or vanish along the LD path to fission parametrized by q_2.
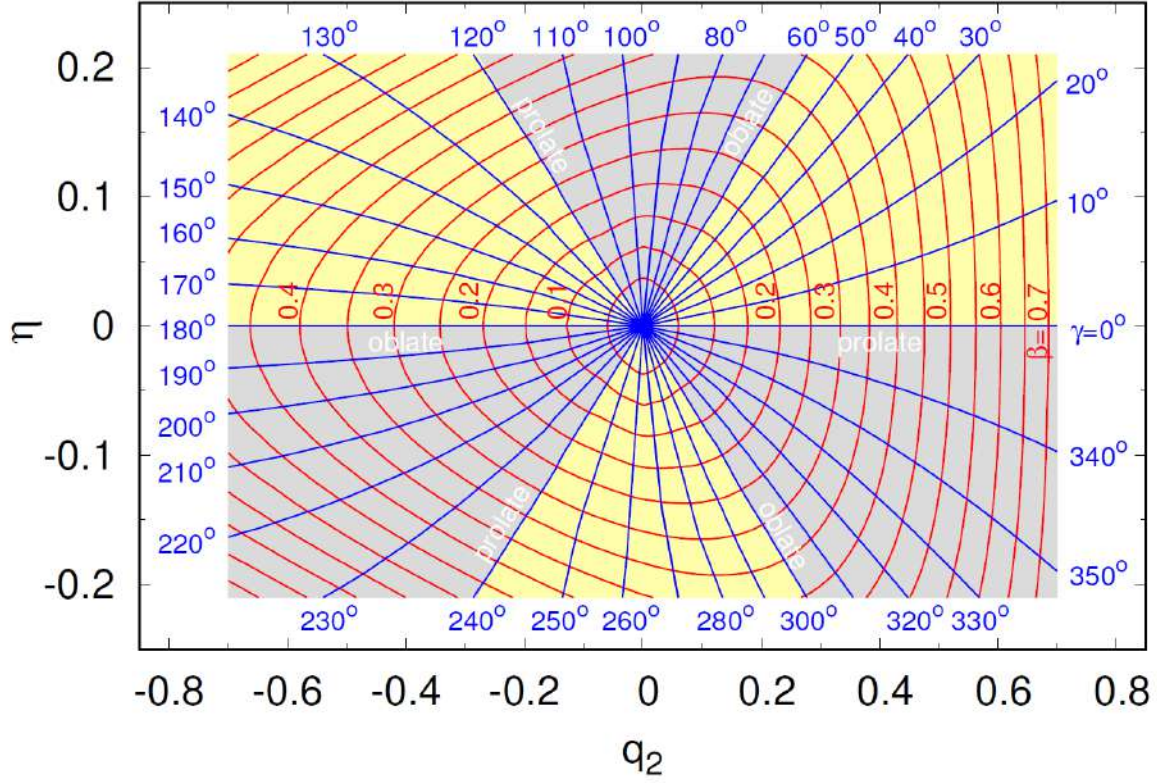
Figure 3.2: relation between β, γ and the (q_2, η) collective coordinates.

In order to work with the collective coordinates (q_2, η) we must indicate the relationship with the commonly used deformation parameters (β, γ) of Bohr:

$$\beta = \frac{1}{X}\sqrt{Q_{20}^2 + Q_{22}^2} \qquad \text{and} \qquad \gamma = \arctan\left(\frac{Q_{22}}{Q_{20}}\right) \qquad (3.30)$$

The parameters Q_{20}^2 and Q_{22}^2 are the components of the mass quadrupole tensor, being defined as:

$$Q_{20} = \langle 2z^2 - r^2 \rangle, \qquad Q_{22} = \langle y^2 - x^2 \rangle \qquad (3.31)$$

The parameter $X = 3r_0^2 A^{5/3}/\sqrt{5\pi}$, where r_0 is the radius constant.

The relation between (q_2, η) and (β, γ) can be seen in the graph 3.2, where the $\Delta\gamma = 60^{\circ}$

symmetry can be seen. Because of this symmetry, it is necessary to be careful in the study of the deformation-energy landscapes in our (η, q_2, q_3, q_4) space, so that we do not make the mistake of "double counting" of shapes.

4 Liquid drop fission barriers

Enrico Fermi won the Nobel Prize in 1938 for the synthesis of new elements by bombarding uranium nuclei with neutrons. Paradoxically, with that experiment, Fermi not only synthesized an element with an atomic number greater than 92 but also broke the nucleus. One year later Hahn and F. Strassmann concluded that after bombarding uranium nuclei with neutrons, lighter isotopes of barium originated.

L. Meitner and her collaborator O. Frisch have shown that the experiment of Hahn and Strassman led to the fission of the nucleus bombarded by neutrons (Nature, vol. 143, p. 239). In their explanation of this new process, they have used the deformed liquid drop model, where fission occurs in a process of competition between the long-range Coulomb repulsive forces between the protons that tend to break up the nucleus and the surface tension of the nucleus that tends to keep all the nucleons together in the nucleus, just as the surface of a liquid drop does. This idea of the liquid drop was further developed by N. Bohr and J. A. Wheeler in their paper "The mechanism of nuclear fission" in the Physical Review (vol. 56, p. 426). This liquid drop model has been the basis of later nuclear models, even today, for fission processes.

So far, it has been accepted that this explanation based on the liquid drop model determines the fact of large attractive forces between nearby nucleons and repulsive forces due to the repulsion between protons in the atomic nucleus. Furthermore, with this model, it is also possible to explain the fact that the volume of the nucleus remains constant despite possible deformations on the way to fission. This volume term directly related to the number A determines the major part of the energy of the nucleus which becomes constant independently of the deformation of the nucleus. In addition, the energy of the nucleus is related to its surface area, which is a function of the shape of the nucleus. This competition between the surface energy of the repulsive Coulomb forces between the protons leads to the appearance of an energy barrier, which has to be tunneled in the

fission process.

It should be noted that if the surface energy in the liquid drop model increases faster than the Coulomb energy decreases and in the case when

$$2E_{surf} \geq E_{Coul}, \tag{4.1}$$

we can say that there is a barrier. Using the expressions for E_{surf} and E_{Coul} of the standard liquid drop model described in the previous section, as well as the approximations of the deformation functions B_{surf} and B_{Coul}, it is possible to reformulate the above equation in the form:

$$a_{surf}A^{2/3}\frac{2}{5}\alpha^2 \geq a_{Coul}\frac{Z^2}{A^{1/3}}\frac{\alpha^2}{5} \ , \tag{4.2}$$

The parameter α describes the global deformation of nucleus defined by Swiatecki as:

$$\alpha^2 = 2\pi \int_0^\pi \left[\frac{R(\Theta) - R_{00}}{R_{00}}\right]^2 d\Theta \ , \tag{4.3}$$

The equation 4.2 can be expressed in the form:

$$\frac{2A}{Z^2} \geq 1 \ . \tag{4.4}$$
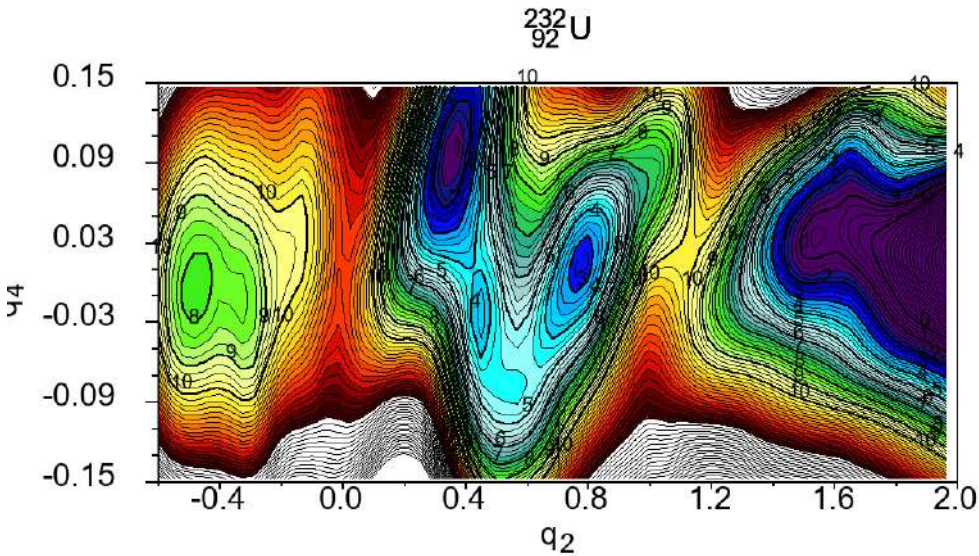
Figure 4.1: Potential energy surface ^{232}U as a function of the elongation and the neck parameter.
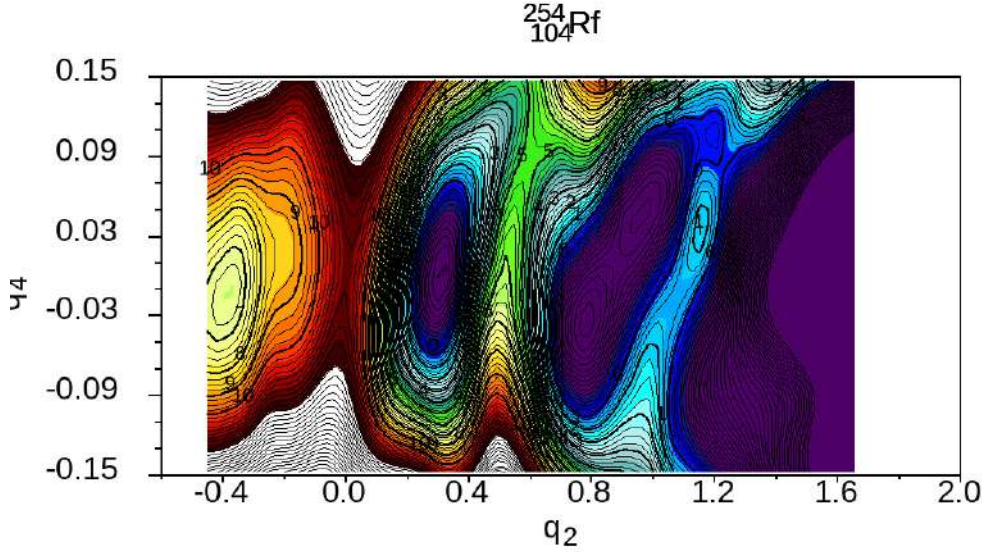
Figure 4.2: Potential energy surface in ^{254}Rf as a function of the elongation and the neck parameter.

One can introduce a so called fissility parameter x:indicating the capacity of the nucleus for spontaneous fission:

$$x \equiv \frac{b_{Coul}Z^2}{2b_{sur}A} \approx \frac{Z^2}{49A}. \tag{4.5}$$

When $x \ll 1$ the probability of fission is extremely small. Conversely, a value of $x > 1$ indicates the disappearance of the LD barrier. It is only a general trend, in reality, the microscopic (read quantum origin) energy corrections described in the next chapters, modify the LD fission barrier that can be seen in Figs. 4.1 and 4.2.

In Fig. 4.1 the difference between the energy of deformed and the spherical LSD energy of ^{232}U is shown as a function of the Fourier deformation parameters q_2 and q_4. In this landscape of the potential energy surface (PES) we can observe in this case that the ground state is approximately at $q_2 \approx 0.35$ and that there are two saddle points located at $q_2 \approx 0.6$ and $q_2 \approx 1.1$, which gives rise to two energy barriers in this case. The exit from the barrier, turning-point, would be approximately at $q_2 \approx 1.5$. Similar but shorter fission barrier one can see in Fig. 4.2 where the PES of ^{254}Rf is presented.

In the case of super-heavy elements, the barrier of the liquid drop is significantly reduced, in some cases, the barrier even disappears. This is due to the high Coulomb repulsion compared to the attractive nuclear forces between the nucleons. Despite this non-existent barrier, experimental results have shown that heavy and super-heavy elements (SHE)

can be stable and do not undergo spontaneous fission. If, in addition to the liquid drop, where no energy barrier is predicted for SHE, we also take into account that the nuclear energy also includes the quantal corrections, we see that the shell correction and the pairing effects are responsible for the existence of an energy barrier that provides sufficient stability for heavy and super-heavy elements not to undergo spontaneous fission.

5 Yukawa-folding description of the structure of the nucleus

In this chapter, we would like to show the main steps that led to the one of the most effective single-particle mean-field potential called the Yukawa-folded potential, which will be used in this thesis to evaluate the microscopic energy corrections as described in the next chapters.

The effective nucleon-nucleon interaction was proposed by Hideki Yukawa in 1935. It describes the strong attractive interaction between two nucleons by the exchange of a meson, just as the photon is a "particle" responsible for the transmission of the electromagnetic force. Considering the short distances of the strong Yukawa interaction, it was possible to estimate the mass of the meson particle at about $140 MeV/c^2$. This particle was discovered two years later and was given the name $\pi - meson$. Therefore, the potential proposed by Yukawa is of the form:

$$V_{Yuk}(r) = G \frac{1}{r} e^{-\frac{m_\pi c}{\hbar} r} \ ,$$

(5.1)

where the characteristic length of this interaction is the Compton wavelength defined as:

$$\left(\frac{\lambda}{2\pi} \right)_\pi = \frac{\hbar}{m_\pi c} \ .$$

(5.2)

This length is approximately $\lambda = 1.4$ fm, with a pion mass of $\approx$ 139 MeV, it is therefore of very short range. The parameter G in the equation 5.1 is the coupling constant of the Yukawa interaction.

5.1 Folded nucleon densities

One of the easiest ways to express nuclear density is with the help of a folding procedure (37):

$$\rho(\overrightarrow{r_1}) = \rho_0 \int_V g(|\overrightarrow{r_1} - \overrightarrow{r_2}|) \, d^3 r_2 \ .$$

(5.3)

Above, the parameter ρ_0 is the uniform density distribution of the charge or the nuclear

matter:

$$\rho_0(C) = \begin{cases} \rho_0 = 3A/4\pi R_0^3 & \text{for} \quad r \leq R_0 \ , \\ \\ 0 & \text{for} \quad r \geq R_0 \ . \end{cases} \tag{5.4}$$

Such a density distribution must satisfy the condition of conservation of the number of nucleons:

$$\int_V \rho_0(\overrightarrow{r_1}) \, d^3r = N(Z) \ . \tag{5.5}$$

The folding function in Eq. 5.3 must also be normalized to unity:

$$\int_V g(|\overrightarrow{r_1} - \overrightarrow{r_2}|) \, d^3r_2 = 1 \ . \tag{5.6}$$

We choose the folding function $g(|\overrightarrow{r_1} - \overrightarrow{r_2}|)$ to be of the form of the Yukawa function 5.1 with the width parameter a approximated to the pion Compton wavelength

$$g(|\overrightarrow{r_1} - \overrightarrow{r_2}|) = \frac{1}{4\pi a^3} \frac{e^{|\overrightarrow{r_1} - \overrightarrow{r_2}|/a}}{|\overrightarrow{r_1} - \overrightarrow{r_2}|/a}. \tag{5.7}$$

We must be careful not to confuse the function $g(|\overrightarrow{r_1} - \overrightarrow{r_2}|)$ which represents the two-nucleon interaction with a short-range interaction between the N-particles creating a density distribution with a diffuse surface with diffuseness approximating 1 fm, as described in the equation 5.3.

5.2   Coulomb interaction potential

As already seen, the charge distribution in the nucleus is described by Eq. 5.3. It is now possible to give an expression to calculate the Coulomb potential:

$$V_c = e \int_V \frac{\rho(\overrightarrow{r_2})}{|\overrightarrow{r_1} - \overrightarrow{r_2}|} \, d^3r_2 \ . \tag{5.8}$$

Let us introduce a function f which satisfies the following equation:

$$\int_V f(\overrightarrow{r_1} - \overrightarrow{r_2}) g(\overrightarrow{r_1} - \overrightarrow{r_2}) \, d^3r_2 = \int_{-\infty}^{\infty} f(\overrightarrow{k}) g(\overrightarrow{k}) e^{i\overrightarrow{k}(\overrightarrow{r_1} - \overrightarrow{r_3})} \, d^3k \ , \tag{5.9}$$

where g is given by Eq. 5.7.

If we replace $g(\vec{r_1} - \vec{r_3})\frac{1}{|\vec{r_1} - \vec{r_2}|}$ by its Fourier transform, then:

$$V_c(\vec{r_1}) = \frac{4\pi e \rho_0}{(2\pi)^{3/2}} \int_V d^3r_3 \int_{-\infty}^{\infty} \frac{1}{K^2} g(k) e^{i\vec{k}(\vec{r_1}-\vec{r_3})} d^3k \; , \tag{5.10}$$

in this case, the Fourier transform of the Yukawa function of the equation 5.7 will have the form:

$$g(k) = \frac{1}{2\pi} \frac{1}{(1 + a^2 k^2)} \; . \tag{5.11}$$

Since the function g has dependence only on $\vec{k}$, it is possible to develop a new integration and rewrite the above equation:

$$V_c(\vec{r_1}) = 4(2\pi)^{1/2} e \rho_0 \int_V \frac{1}{|\vec{r_1} - \vec{r_3}|} d^3r_3 \int_{-\infty}^{\infty} \frac{g(k)}{k} \sin(k|\vec{r_1} - \vec{r_3}|) \, dk \; . \tag{5.12}$$

Now, we can insert in the Fourier transform of the Yukawa function, the equation. 5.11, the above expression is:

$$V_c(\vec{r_1}) = \frac{4(2\pi)^{1/2} e \rho_0}{(2\pi)^{3/2}} \int_V \frac{1}{|\vec{r_1} - \vec{r_3}|} d^3r_3 \times \int_0^{\infty} \frac{1}{(1 + a^2 k^2)} \frac{1}{k} \sin(k|\vec{r_1} - \vec{r_3}|) \, dk \; . \tag{5.13}$$

Using the relationship:

$$\sin(x) = \frac{e^{ix} - e^{-ix}}{2i} \; , \tag{5.14}$$

one can rewrite the previous equation:

$$\begin{aligned} V_c(\vec{r_1}) &= \frac{2}{\pi} e \rho_0 \int_V \frac{1}{|\vec{r_1} - \vec{r_3}|} d^3r_3 \times \int_0^{\infty} \frac{e^{i\vec{k}(\vec{r_1}-\vec{r_3})}}{2ik(k^2 + \frac{1}{a^2})} = \\ &= \frac{e \rho_0}{\pi i} \int_V \frac{1}{|\vec{r_1} - \vec{r_3}|} d^3r_3 \times \int_{-\infty}^{\infty} \frac{e^{i\vec{k}(\vec{r_1}-\vec{r_3})}}{a^2 k(k^2 + \frac{1}{a^2})} \end{aligned} \tag{5.15}$$

The residue method allows to develop of this integral, which will obtain the following more simplified form:

$$V_c(\vec{r_1}) = V_c(\vec{r_1}; sharp) + \Delta V_c(\vec{r_1}) \; , \tag{5.16}$$

where $V_c(\vec{r_1}; sharp)$ is the dominant term in the Coulomb potential originated from a uniform density distribution, and $V_c(\vec{r_1})$ is the correction created by the diffuseness of the charge in the atomic nucleus.

The dominant term of the Coulomb potential is expressed as:

$$V_c(\overrightarrow{r_1}; sharp) = \rho_0 e \int_V \frac{1}{|\overrightarrow{r_1} - \overrightarrow{r_2}|} d^3r_2 \ . \tag{5.17}$$

while the contribution from the surface "diffuseness" reads:

$$\Delta V_c(\overrightarrow{r_1}) = -\rho_0 e \int_V \frac{1}{|\overrightarrow{r_1} - \overrightarrow{r_2}|} e^{-\frac{|\overrightarrow{r_1} - \overrightarrow{r_2}|}{a}} d^3r_2 \ . \tag{5.18}$$

In order to convert the volume of a function such as $f(|\overrightarrow{r_1} - \overrightarrow{r_2}|)$ into a surface with the function $F(|\overrightarrow{r_1} - \overrightarrow{r_2}|)$ applied to the nucleus, we can make use of Gauss's theorem:

$$\int_V r^2 f(|\overrightarrow{r_1} - \overrightarrow{r_2}|) \, d^3r_2 = \oint_S (d\overrightarrow{S_2} \cdot \overrightarrow{r_{12}}) F(|\overrightarrow{r_1} - \overrightarrow{r_2}|) \ . \tag{5.19}$$

Now, for convenience, we can transform these two integrals for numerical integration using the Gauss-Legendre method:

$$V_c(\overrightarrow{r_1}; sharp) = -\frac{\rho_0 e}{2} \oint_S [d\overrightarrow{S_2} \cdot (\overrightarrow{r_1} - \overrightarrow{r_2})] \frac{1}{|\overrightarrow{r_1} - \overrightarrow{r_2}|} \tag{5.20}$$

and

$$\Delta V_c(\overrightarrow{r_1}) = \frac{\rho_0 e}{a} \oint_S [d\overrightarrow{S_2} \cdot (\overrightarrow{r_1} - \overrightarrow{r_2})] \left(\frac{|\overrightarrow{r_1} - \overrightarrow{r_2}|}{a} \right)^{-3} \times$$
$$\times \left[1 - \left(1 + \frac{|\overrightarrow{r_1} - \overrightarrow{r_2}|}{a} \right) e^{-\frac{|\overrightarrow{r_1} - \overrightarrow{r_2}|}{a}} \right] \ . \tag{5.21}$$

For spherical-shaped nuclei of radius R_0, the integrals 5.20 and 5.21 can be solved analytically.

5.3   Coulomb energy

Following the methods of folding the density distributions of nucleons in the atomic nucleus described in the previous section, we will calculate the Coulomb energy for non-spherical nuclei. The energy in this case is written in the standard way:

$$E_c = \frac{1}{2} \int_V \int_V \frac{1}{|\overrightarrow{r_1} - \overrightarrow{r_2}|} \rho(\overrightarrow{r_1}) \rho(\overrightarrow{r_2}) \, d^3r_1 d^3r_2 \ . \tag{5.22}$$

Now, having introduced the folded density 5.3, the above equation remains:

$$E_c = \frac{\rho_0^2}{2} \int_V \int_V \frac{1}{|\vec{r_1} - \vec{r_2}|} d^3r_1 d^3r_2 \times \int_V \int_V g(|\vec{r_1} - \vec{r_3}|)g(|\vec{r_2} - \vec{r_4}|)\, d^3r_3\, d^3r_4 \ . \qquad (5.23)$$

Moving on with the calculations made in the case of the Coulomb potential, we can express the equation 5.9 for the three functions f, g and h:

$$\int_V \int_V f(|\vec{r_1} - \vec{r_2}|)g(|\vec{r_1} - \vec{r_3}|)g(|\vec{r_2} - \vec{r_4}|)d^3r_1 d^3r_2 =$$
$$= (2\pi)^{3/2} \int_\infty f(\vec{k})g(-\vec{k})h(\vec{k})e^{i\vec{k}(\vec{r_3} - \vec{r_4})}\, d^3\vec{k}. \qquad (5.24)$$

If we introduce the above equation into Eq. 5.23, it remains like (37):

$$E_c = 4\pi \frac{\rho_0^2}{2} \int_V \int_V d^3r_1 d^3r_2 \int_\infty \frac{1}{k^2}g^2(k)e^{i\vec{k}(\vec{r_1} - \vec{r_2})}\, d^3k \ . \qquad (5.25)$$

Calculating the integral over the variable k, we can write:

$$E_c = \frac{(4\pi\rho_0)^2}{2} \int_V \int_V \frac{d^3r_1 d^3r_2}{|\vec{r_1} - \vec{r_2}|} \int_\infty \frac{g^2(k)}{k} \sin(k|\vec{r_1} - \vec{r_2}|)\, dk \ . \qquad (5.26)$$

On the function g of Eq. 5.11 we apply the Fourier transform:

$$E_c = \frac{\rho_0^2}{2\pi} \frac{1}{i} \int_V \int_V \frac{d^3r_1 d^3r_2}{|\vec{r_1} - \vec{r_2}|} \int_{-\infty}^{\infty} \frac{e^{i\vec{k}|\vec{r_1} - \vec{r_2}|}}{k(1 + a^2k^2)^2}\, dk. \qquad (5.27)$$

Using the residue theorem of integrating in the complex plane, we arrive at the result:

$$E_c = E_c(sharp) + \Delta E_c \ , \qquad (5.28)$$

where $E_c(sharp)$ represents the part of the Coulomb energy produced by the uniform nucleonic density distribution, whereas ΔE_c corresponds to the correction due to a diffused surface charge. Finally, both these terms write

$$E_c(sharp) = \frac{\rho_0^2}{12} \int_V \int_V \frac{d^3r_1 d^3r_2}{|\vec{r_1} - \vec{r_2}|} \ , \qquad (5.29)$$

and

$$\Delta E_c = \frac{-\rho_0^2}{2} \int_V \int_V \frac{d^3 r_1 d^3 r_2}{|\vec{r_1} - \vec{r_2}|} e^{-|\vec{r_1} - \vec{r_2}|/a} \left(1 + \frac{1}{2} \frac{|\vec{r_1} - \vec{r_2}|}{a} \right) . \qquad (5.30)$$

Using the Gauss-Ostrogradsky theorem we can convert the double volume integrals into the corresponding surface integrals, so the equations are written respectively:

$$E_c(sharp) = -\frac{\rho_0^2}{12} \oint_S \oint_S \frac{[d\vec{S_1} \cdot (\vec{r_1} - \vec{r_2})][d\vec{S_2} \cdot (\vec{r_1} - \vec{r_2})]}{|\vec{r_1} - \vec{r_2}|} , \qquad (5.31)$$

and

$$\Delta E_c = \frac{\rho_0^2}{2a} \oint_S \oint_S \frac{[d\vec{S_1} \cdot (\vec{r_1} - \vec{r_2})][d\vec{S_2} \cdot (\vec{r_1} - \vec{r_2})]}{|\vec{r_1} - \vec{r_2}|/a^4} \times$$
$$\times \left[2\frac{|\vec{r_1} - \vec{r_2}|}{a} - 5 + \left(5 + 3\frac{|\vec{r_1} - \vec{r_2}|}{a} + \frac{1}{2} \frac{|\vec{r_1} - \vec{r_2}|}{a^2} \right) e^{-\frac{|\vec{r_1} - \vec{r_2}|}{a}} \right] . \qquad (5.32)$$

5.4   Yukawa-folded effective potentials

The macroscopic-microscopic model is widely known and used to calculate the potential energy functions of the atomic nucleus. This model was greatly improved with the introduction of the shell effect by Myers and Swiatecki (38) [Nucl. Phys. 81, 1 (1966)], but it continued to make further improvements in order to give a closer description of the total nuclear energy as a function of deformation.

In 1966, Strutinsky published a new way of calculating the shell effects (39) [Sov. J. Nucl. Phys. 3, 449 (1966)] which was another important improvement of the macroscopic-microscopic model. The new correction proposed by Strutinsky consists in the idea that one evaluates the shell energy as a difference between the sum of occupied single-particle levels and the energy of a nucleus in which the shell structure is washed out.

On the other hand, another important improvement to the macroscopic-microscopic model was introduced in the development of a theory of short-range pairing corrections. The Bardeen-Cooper-Schrieffer (BCS) theory developed previously to explain the superconductivity observed in solid states [Phys. Rev. 108, 1175 (1957)], was successfully applied by A. Bohr, B. Mottelson and Pines to atomic nuclei [Phys. rev. 110, 936

(1958)]. Applying both shell and pairing corrections to the main liquid-drop smooth energy contribution, which are based on the idea of single-particle levels, varying widely depending on the shape of the nucleus, one theoretically reproduces the potential energy of a nucleus. It hence becomes clear that knowledge of the nuclear mean-field potential to generate the individual nucleonic levels is necessary to successfully address the nuclear processes such as fission, fusion, vibrations, rotations, etc. As widely known, in these processes, the deformation dependent potential energy surface is a crucial quantity determining their essential properties, as half-lives, fragmentation modes, multiplicities of emitted light particles and others.

The first realistic single-particle nuclear potential was proposed by Nilsson in 1955 [Mat. Fys. Medd. Dan. Vid. Selsk. **29** (16) (1955)]. He has approximated the nuclear mean-field potential by the harmonic oscillator potential corrected by a term proportional to l^2 which deepens the potential for the peripheral nucleons. In addition, he also took into account the spin-orbit coupling $\sim \vec{l} \cdot \vec{s}$ to reproduce the splitting of the single-particle energy levels. Apart of the Nillson potential, another more realistic potential was proposed by Woods and Saxon [Phys. Rev. **95**, 577 (1954)], which incorporated several improvements that have successfully predicted the energy potentials to this day.

Taking into account that the mean-field single-particle potential must describe the density distribution of nucleons, it is possible to create its form using the convolution of the density of the nucleus with the Yukawa-like function, as proposed by Krappe, Nix and Sierk [Phys. Rev. C **20**, 992 (1979)]. Taking a spin independent two-body Yukawa interaction, i.e. as the interaction of two infinitesimal volume elements of the nuclear drop:

$$V(r_{12}) = -\frac{V_0}{4\pi\lambda^3} \frac{-e^{|\vec{r_1}-\vec{r_2}|/\lambda}}{|\vec{r_1}-\vec{r_2}|/\lambda} \ , \tag{5.33}$$

where $r_{12} = |\vec{r_1} - \vec{r_2}|$ and folding with it the density distribution 5.3, they have obtained the central part of the single-particle potential of the form:

$$V_{sp}(\vec{r_1}) = \int_V r_2 V(r_{12}) \frac{\rho(\vec{r_2})}{\rho_0} \, d^3r_2 \ . \tag{5.34}$$

Just as we use the Fourier transform in the equation 5.11, we can apply it in the above

equation as well:

$$V_{sp}(\overrightarrow{r_1}) = -\frac{V_0}{(2\pi)^{3/2}} \int_V d^3r_3 \int_{-\infty}^{\infty} \frac{g(k)}{1+\lambda^2 k^2} e^{i\overrightarrow{k}(\overrightarrow{r_1}-\overrightarrow{r_3})} d^3k \ . \tag{5.35}$$

We can develop the second integral of the equation over the angles θ and ϕ in the momentum-space so that the equation follows:

$$V_{sp}(\overrightarrow{r_1}) = -\left(\frac{2}{\pi}\right)^{1/2} V_0 \int_V \frac{d^3r_3}{|\overrightarrow{r_1}-\overrightarrow{r_3}|} \int_0^{\infty} k\frac{g(k)}{1+\lambda^2 k^2} \sin(k|\overrightarrow{r_1}-\overrightarrow{r_3}|) \, dk \tag{5.36}$$

Replacing the function $g(k)$ by its Fourier transform 5.11 we get an expression that is possible to develop with the method of residues:

$$V_{sp}(\overrightarrow{r_1}) = -\frac{V_0}{4\pi^2 i} \int_V \frac{d^3r_3}{|\overrightarrow{r_1}-\overrightarrow{r_3}|} \int_{-\infty}^{\infty} \frac{e^{ik|\overrightarrow{r_1}-\overrightarrow{r_3}|}}{(1+\lambda^2 k^2)(1+a2k^2)} \, dk \ . \tag{5.37}$$

The range of λ in the Yukawa interaction is considered to be somewhat different compared to the range of a of the folding function used to create the density distribution of equation 5.11.

Having integrated the above expression in the complex plane, the equation is simplified to give the mean-field potential as the sum of two contributions:

$$V_{sp}(\overrightarrow{r_1}) = V(\overrightarrow{r_1}; sharp) + \Delta V(\overrightarrow{r_1}) \ . \tag{5.38}$$

The uniform-density potential is independent of the density of diffuseness a:

$$V(\overrightarrow{r_1}; sharp) = -\frac{V_0}{4\lambda^3} \int_V \frac{e^{-|\overrightarrow{r_1}-\overrightarrow{r_2}|/\lambda}}{|\overrightarrow{r_1}-\overrightarrow{r_2}|/\lambda} \, d^3r_2 \ . \tag{5.39}$$

The correction will be a function depending on the diffuseness parameters λ and a:

$$\Delta V(\overrightarrow{r_1}) = -\frac{a^2}{a^2-\lambda^2} V(\overrightarrow{r_1}; sharp) - \frac{V_0}{4\pi(a^2-\lambda^2)} \int_V \frac{e^{-|\overrightarrow{r_1}-\overrightarrow{r_2}|/a}}{|\overrightarrow{r_1}-\overrightarrow{r_2}|} \, d^3r_2. \tag{5.40}$$

Applying Gauss-Ostrogradsky theorem and transforming the spatial integrals into the

equivalent surface integrals, we get:

$$V(\vec{r_1}; sharp) = \frac{V_0}{4\pi\lambda^3} \oint_S \left(d\vec{S_2} \cdot \vec{r_{12}}\right) \left(\frac{|\vec{r_1} - \vec{r_2}|}{\lambda}\right)^{-3} \left[1 - \left(1 + \frac{|\vec{r_1} - \vec{r_2}|}{\lambda}\right) e^{\frac{|\vec{r_1} - \vec{r_2}|}{\lambda}}\right]$$

$$(5.41)$$

and

$$\Delta V(\vec{r_1}) = -\frac{a^2}{a^2 - \lambda^2} V(\vec{r_1}; sharp) + \frac{V_0}{4\pi(a^2 - \lambda^2)} \oint_S \left(d\vec{S_2} \cdot \vec{r_{12}}\right) \left(\frac{|\vec{r_1} - \vec{r_2}|}{a}\right)^{-3} \times$$
$$\times \left[1 - \left(1 + \frac{|\vec{r_1} - \vec{r_2}|}{a}\right) e^{\frac{|\vec{r_1} - \vec{r_2}|}{a}}\right] .$$

$$(5.42)$$

In the case of a spherical-shaped nucleus of radius R_0, the equation 5.41 may be written in the analytical form as:

$$V_{sph}(r_1; sharp) = \begin{cases} -V_0 \left[1 - \left(1 + \frac{R_0}{\lambda}\right) e^{-R_0/\lambda} \frac{\sinh(r_1/\lambda)}{(r_1/\lambda)}\right] & \text{for} \quad r_1 \leq R_0 , \\ -V_0 \left[\frac{R_0}{\lambda}\cosh\left(\frac{R_o}{\lambda}\right) - \sinh\left(\frac{R_o}{\lambda}\right)\right] \frac{e^{-r_1/\lambda}}{r_1\lambda} & \text{for} \quad r_1 \geq R_0 , \end{cases}$$

$$(5.43)$$

and

$$\Delta V_{sph}(r_1) = -\frac{a^2}{(a^2 - \lambda^2)} V_{sph}(r_1; sharp) +$$
$$+ \begin{cases} \frac{a^2 V_0}{(\lambda^2 - a^2)} \left[1 - \left(1 + \frac{R_0}{a}\right) e^{-R_0/a} \frac{\sinh(r_1/a)}{(r_1/a)}\right] & \text{for} \quad r_1 \leq R_0 , \\ \frac{a^2 V_0}{(\lambda^2 - a^2)} \left[\frac{R_0}{a}\cosh\left(\frac{R_o}{a}\right) - \sinh\left(\frac{R_o}{a}\right)\right] \frac{e^{-r_1/a}}{r_1/a} & \text{for} \quad r_1 \geq R_0 . \end{cases}$$

$$(5.44)$$

In this way, we get the splitting of the folded Coulomb and the nuclear potentials together with the corresponding energies in the form of *sharp* and *diffused* components.

It was shown e.g. in Ref. [Phys. Rev. C **75**, 024613 (2007)] that the effect of the *density diffuseness* can be simulated by a *renormalization* of the diffuseness parameter λ used in the *sharp-density* contribution. Moreover, it was found that the correction of the *sharp-density* diffuseness changes very slowly with the nuclear deformation. Because of these considerations, these corrections were not used in the forms given in the equations

We move on to consider the spin-orbit component of the total single-particle potential, which can be generated by making use of the central part of the potential V_{sp} as:

$$V_{S.O.} = i\lambda^q \left(\frac{\hbar}{2Mc}\right)^2 \vec{\nabla} V_{sp} \cdot \left[\vec{\sigma} \times \vec{\nabla}\right], \qquad q = n, p. \tag{5.45}$$

The parameter $\vec{\sigma}$ represents the vector of 2×2 Pauli matrices $(\sigma_x, \sigma_y, \sigma_z)$.

For the central parts of the single-particle potentials for protons and neutrons we have taken into account the following parametrization of Ref. (41):

$$V_0^p = V_s + V_a \bar{\delta}$$
$$V_0^n = V_s - V_a \bar{\delta} \tag{5.46}$$

The parameters are defined by the following formulas:

$$\bar{\delta} = \left(I + \frac{3c_1}{8Q} \frac{Z^2}{A^{5/3}}\right) / \left(1 + \frac{9}{4} \frac{J}{Q} \frac{1}{A^{1/3}}\right) \qquad I = (N - Z)/A, \tag{5.47}$$

$$\lambda^p = 6.0 \left(\frac{A}{240}\right) + 28.0 \tag{5.48}$$

and

$$\lambda^n = 4.5 \left(\frac{A}{240}\right) + 31.5. \tag{5.49}$$

A comparison between the shape of the Yukawa folded potential and the Woods-Saxon potential for the spherical ^{240}Pu is presented in Fig. 5.1.

Parameters List		
Constant	value	unit
λ	0.8	$[fm]$
a	0.7	$[fm]$
V_s	52.5	$[MeV]$
V_a	48.7	$[MeV]$
J	35.0	$[MeV]$
Q	25.0	$[MeV]$
c_1	$\frac{3}{5}\frac{e^2}{r_0}$	[MeV]
M	938.9	$[MeV/c^2]$
r_0	1.16	$[fm]$

Table 5.1: Yukawa-folding constants
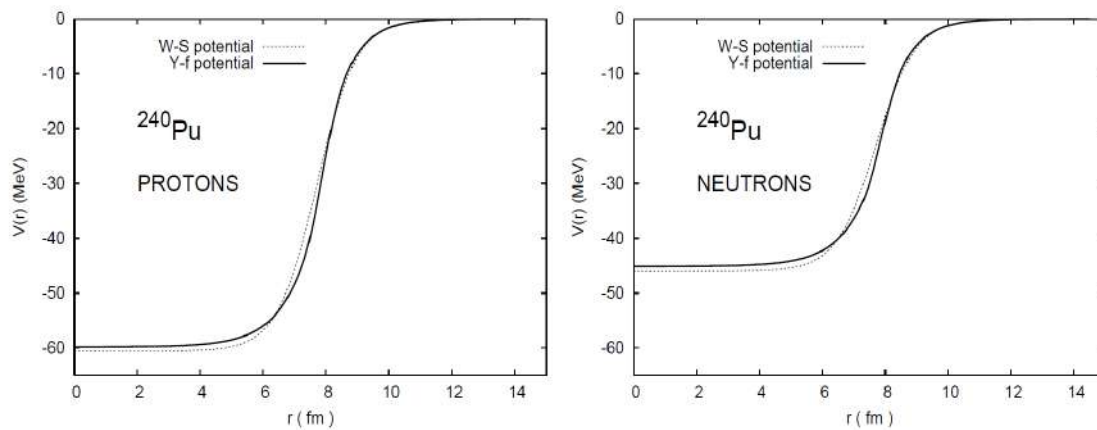
Figure 5.1: Comparison of the spherical Yukawa-folded (solid line) and Woods-Saxon (dashed line) central potentials for protons and neutrons in ^{240}Pu nucleus. The Woods-Saxon potential parameters are taken form (42).

6   Pairing correction

The pairing interaction proves to be a good approximation of the short-range forces between nucleons of equal, but opposite directed total angular momenta. We have evidence for these forces from numerous experimental results which we list here:

1. The total angular momentum (spin) of all even-even nuclei is equal to 0. In the case of an odd nucleus, the spin comes from the angular momentum of the last valence particle,

2. The moments of inertia of the nuclei evaluated without the pairing correlation is much too large in comparison with the data,

3. Near-magic nuclei stay spherical due to the competition of the short-range pairing correlations with the long-range interaction which prefers deformed shapes of nuclei,

4. Existence of energetic gap between the ground state and the first excited level in even-even nuclei.

Superconductivity is the physical phenomenon produced in the nucleus from a pair of nucleons that move in opposite directions. The name superconductivity is used, as it is similar to what happens to electrons in metals when at low temperatures, a pair of electrons combine to produce what is known as Cooper pairs.

Bohr, Mottelson and Pines gave a description of the pairing interactions in nuclei, making use of the BCS theory given by Bardeen, Cooper and Schrieffer in the study of the solid state to explain the phenomenon of superconductivity.

To find the solutions of the eigenproblem of a system of nucleons interacting with the pairing forces, we will use the BCS theory, whose Hamiltonian can be written as:

$$\hat{H} = \sum_{\nu} e_{\nu} a_{\nu}^{+} a_{\nu} - G \sum_{\nu>0,\nu'>0} a_{\nu}^{+} a_{-\nu}^{+} a_{-\nu'} a_{\nu'} \ . \tag{6.1}$$

The single-particle states are represented by the eigenfunctions, $|\nu\rangle$ and the corresponding eigen-energies, e_{ν} of the mean-field Hamiltonian. $|\nu\rangle$ is a state with a positive third component of angular momentum, while $|-\nu\rangle$ is its counterpart with negative third

component of angular momentum.

Applying Kramer's theorem for the time reversal invariant Hamiltonian we get that the nucleon states are doubly degenerate. For example, looking at the states $|\nu\rangle$ and $|-\nu\rangle$, they have exactly the same single-particle energy.

If we review the equation 6.1, its first term describes the energy of non-interacting particles, the second term of the equation describes the contribution of the pairing interaction. The quantity G is the parameter describing the average, monopole pairing strength between the two nucleons of opposite spins.

Recall that for fermions, the creation a_ν^+ and annihilation a_ν operators fulfill the commutation conditions, in order to take into account the Pauli principle.

We therefore define the total vacuum of fermions $|0\rangle$ as a state in which it is no longer possible to annihilate any particle:

$$a_\nu|0\rangle = 0, \qquad \text{or} \qquad \langle 0|a_\nu^+ = 0 \;, \tag{6.2}$$

since the creation operator $a_\nu^+ = [(a_\nu)]^\dagger$, is the Hermitian conjugation of the particle annihilation operator.

6.1   Even-even nuclei

In the BCS wave function it is assumed that the ground-state of the system of even number n of fermions of the same type is described by the following function:

$$|\Phi_0\rangle = \prod_{\nu>0}(U_\nu + V_\nu a_\nu^+ a_{-\nu}^+)|0\rangle \;, \tag{6.3}$$

with V_ν^2 being the occupation probability of the energy level e_ν by a pair of particles. If its value is equal to 1, it means that the state is occupied. The amplitude U_ν^2 is hence the probability of not being occupied. The normalization of $\Phi_0\rangle$ function implies that:

$$U_\nu^2 + V_\nu^2 = 1 \;. \tag{6.4}$$

This condition has to be satisfied for every state ν. The values V_ν^2 and U_ν^2 range from 0 to 1 and form a set of parameters determined for the BCS ground state making the total energy of the system minimum. These are identical real numbers for $|\nu\rangle$ and $|-\nu\rangle$:

$$U_\nu = U_{-\nu}, \qquad V_\nu = V_{-\nu}. \tag{6.5}$$

Despite the great importance of the BCS description in nuclear physics, it has a major disadvantage. The product 6.3 does not correspond to a given number of particles residing in the system. In order to conserve the number of particles n, we have to evaluate the expectation value of the particle number operator $\hat{N}$:

$$\hat{N} = \sum_\nu a_\nu^+ a_\nu \tag{6.6}$$

in the ground-state $|\Phi_0\rangle$ and to solve the following variational problem:

$$\langle\Phi_0|\hat{H}|\Phi_0\rangle - \lambda\langle\Phi_0|\hat{N}|\Phi_0\rangle = minimum \ , \tag{6.7}$$

with the condition for the conservation of particle number, introduced by the method of Lagrange multipliers, λ. It corresponds to the minimization of the average value of the following modified Hamiltonian:

$$\hat{H}' = \hat{H} - \lambda\hat{N} = \sum_{\nu>0}(e_\nu - \lambda)(a_\nu^+ a_\nu + a_{-\nu}^+ a_{-\nu}) - G\sum_{\nu'>0,\nu\neq\nu',\nu>0} a_\nu^+ a_{-\nu}^+ a_{\nu'}^- a_\nu' \ , \tag{6.8}$$

where the single-particle energies are shifted by the multiplier λ, which has the meaning of the Fermi level.

In order to calculate the above average value, it is useful to introduce the concept of quasi-particles, for which the ground-state of the system $|\Phi_0\rangle$ is the vacuum. Therefore,

$$\alpha_k|\Phi_0\rangle = 0, \qquad and \qquad \langle\Phi_0|\alpha_k^+ = 0 \ . \tag{6.9}$$

The operators of the creation α_k^+ and annihilation α_k^+ of a bosonic quasi-particle have to

satisfy the anti-commutation conditions:

$$\{\alpha_\nu, \alpha_{\nu'}\} = \delta_{\nu\nu'} , \qquad \{\alpha_\nu, \alpha_{\nu'}\} = \{\alpha_\nu^+, \alpha_{\nu'}^+\} = 0 . \tag{6.10}$$

The annihilation and quasi-particle creation operators that satisfy the above conditions are given by the Bogolubov-Valatin transformation:

$$
\begin{aligned}
\alpha_\nu &= U_\nu a_\nu - V_\nu a_{-\nu}^+ , \\
\alpha_{-\nu} &= U_\nu a_{-\nu} + V_\nu a_\nu^+ .
\end{aligned}
\tag{6.11}
$$

The creation operator of quasi-particles can be obtained by the Hermitian coupling of the above equations:

$$
\begin{aligned}
\alpha_\nu^+ &= U_\nu a_\nu^+ - V_\nu a_{-\nu}^+ , \\
\alpha_{-\nu}^+ &= U_\nu a_{-\nu}^+ + V_\nu a_\nu^+ .
\end{aligned}
\tag{6.12}
$$

Using these transformations, as well as the anti-commutation rules 6.10 one can evaluate the mean value of the BCS Hamiltonian 6.8 in the BCS ground state $|\Phi_0\rangle$:

$$\langle\Phi_0|\hat{H}'|\Phi_0\rangle = 2\sum_{\nu>0}(e_\nu - \lambda)V_\nu^2 - G\sum_{\nu>0}V_\nu^4 - G\left(\sum_{\nu>0}U_\nu V_\nu\right)^2 . \tag{6.13}$$

This expectation value has a minimum when its full variation over V_ν or U_ν disappears:

$$\sum_\nu \frac{\delta}{\delta V_\nu}\langle\Phi_0|\hat{H}'|\Phi_0\rangle\delta V_\nu = 0 . \tag{6.14}$$

It means that for every ν the variation must vanish:

$$\frac{\delta}{\delta V_\nu}\langle\Phi_0|\hat{H}'|\Phi_0\rangle\delta V_\nu = 0 . \tag{6.15}$$

The derivative on V_ν of the equation 6.13 reads:

$$4(e_\nu - \lambda)V_\nu - 4GV_\nu^3 - 2G\left(\sum_{\mu>0}U_\mu V_\nu\right)\left(U_\nu + V_\nu\frac{\delta U_\nu^2}{\delta V_\nu}\right) = 0 . \tag{6.16}$$

The derivative of the normalization condition 6.4 gives the following relation:

$$\frac{\delta U_\nu}{\delta V_\nu} = -\frac{V_\nu}{U_\nu} \ . \tag{6.17}$$

Inserting the equation 6.17 to Eq.6.16 we obtain:

$$2(e_\nu - \lambda)V_\nu - 2GV_\nu^3 - G\left(\sum_{\mu>0} U_\mu V_\nu\right)\left(U_\nu - \frac{V_\nu^2}{U_\nu}\right) = 0. \tag{6.18}$$

Let us also define a parameter Δ called the pairing energy gap:

$$\Delta \equiv G\sum_{\mu>0} U_\mu V_\mu \tag{6.19}$$

and introduce the notation:

$$\tilde{e}_\nu \equiv e_\nu - \lambda - GV_\nu^2 \ . \tag{6.20}$$

If we now multiply the equation 6.18 by U_μ:

$$2\tilde{e}_\nu V_\nu U_\nu - \Delta(U_\nu^2 - V_\nu^2) = 0 \tag{6.21}$$

and use the equations 6.21 and 6.4 we obtain:

$$U_\nu^2 = \frac{1}{2}\left(1 + \frac{\tilde{e}_\nu}{\sqrt{\tilde{e}_\nu^2 + \Delta^2}}\right), \qquad V_\nu^2 = \frac{1}{2}\left(1 - \frac{\tilde{e}_\nu}{\sqrt{\tilde{e}_\nu^2 + \Delta^2}}\right) \ . \tag{6.22}$$

The function V_ν^2 expresses the occupation probabilities of the single-particle states and depends on the parameters λ and Δ.

To evaluate the average number of particles in the BCS state, it is useful to write the particle number operator $\hat{N}$ 6.6 in terms of the quasi-particles:

$$
\begin{aligned}
n = \langle\phi_0|\hat{N}|\phi_0\rangle = \langle\phi_0|\sum_{\nu>0}&\{\left(U_\nu\alpha_\nu^+ + V_\nu\alpha_{-\nu}\right)\left(U_\nu\alpha_\nu + V_\nu\alpha_{-\nu}^+\right) \\
&+ \left(U_\nu\alpha_{-\nu}^+ - V_\nu\alpha_\nu\right)\left(U_\nu\alpha_{-\nu} - V_\nu\alpha_\nu^+\right)\}|\phi_0\rangle = 2\sum_{\nu>0} V_\nu^2 \ .
\end{aligned}
\tag{6.23}
$$

If we insert the equation 6.22 into 6.23 we get:

$$\sum_{\nu>0} \left(1 - \frac{\tilde{e}_\nu}{\sqrt{\tilde{e}_\nu^2 + \Delta^2}} \right) = n \ . \tag{6.24}$$

We will be able to use this equation to calculate the parameter λ. Then we can calculate the energy gap Δ using the equations 6.19 and 6.22:

$$\Delta = \frac{G}{2} \sum_{\nu>0} \frac{\Delta}{\sqrt{\tilde{e}_\nu^2 + \Delta^2}} \ . \tag{6.25}$$

If we now divide by $\Delta G/2$:

$$\frac{2}{G} = \sum_{\nu>0} \frac{1}{\sqrt{\tilde{e}_\nu^2 + \Delta^2}} \ . \tag{6.26}$$

The above equation gives also the lower limit for the strength of interaction G at which the the pairing correlation vanishes in the BCS approximation: $G \gg 2/\sum_\nu 1/|\tilde{e}|$.

The complete set of the BCS equations is:

$$\begin{cases} U_\nu^2 = \frac{1}{2} \left(1 + \frac{\tilde{e}_\nu - \lambda}{\sqrt{(\tilde{e}_\nu - \lambda)^2 + \Delta^2}} \right) \\ U_\nu^2 + V_\nu^2 = 1, \\ \sum_{\nu>0} \left(1 - \frac{\tilde{e}_\nu - \lambda}{\sqrt{(\tilde{e}_\nu + \lambda)^2 + \Delta^2)^2}} \right) = n \\ \frac{2}{G} = \sum_{\nu>0} \frac{\tilde{e}_\nu - \lambda}{\sqrt{(\tilde{e}_\nu - \lambda)^2 + \Delta^2}} \end{cases} \tag{6.27}$$

These equations must be solved numerically.

Once Δ and λ are known, we can calculate the energy of the ground state with the following equation:

$$E_0 = 2 \sum_{\nu>0} e_\nu V_\nu^2 - G \sum_{\nu>0} V_\nu^4 - \frac{\Delta^2}{G} \ . \tag{6.28}$$

And then, with the equation 6.3 we can obtain the ground-state function $|\phi_0\rangle$.

6.2   Discussion of the BCS equations

We will now look at physical meaning of the parameters Δ, λ, U_ν and V_ν by reviewing the set of equations 6.27.

The parameter Δ is related to the pairing interaction. If $\Delta = 0$, then the BCS equations are describing a system of free fermions. The parameters U_ν and V_ν are then equal to 0 or 1 depending on the position of the level:

$$
\begin{aligned}
U_\nu^2 &= \frac{1}{2}\left(1 + \frac{(e_\nu - \lambda)}{\sqrt{(e_\nu - \lambda)^2}}\right) = \frac{1}{2}(1 \pm 1) =
\begin{cases}
1 & \text{for } e_\nu > \lambda \, , \\
0 & \text{for } e_\nu < \lambda \, ,
\end{cases} \\
V_\nu^2 &= \frac{1}{2}\left(1 - \frac{(e_\nu - \lambda)}{\sqrt{(e_\nu - \lambda)^2}}\right) = \frac{1}{2}(1 \mp 1) =
\begin{cases}
0 & \text{for } e_\nu > \lambda \, , \\
1 & \text{for } e_\nu < \lambda \, .
\end{cases}
\end{aligned}
\tag{6.29}
$$

It means that the probability that the states below λ are occupied by a pair of particles is 1 and above λ is 0. The Lagrange multiplier λ is not only a mathematical artifice but it represents the Fermi level of the system.

The Bogolubov-Valatin transformation in the case of $\Delta = 0$ is:

$$
\begin{aligned}
\alpha_\nu &=
\begin{cases}
a_\nu & \text{for } e_\nu > \lambda \, , \\
-a_{-\nu}^+ & \text{for } e_\nu < \lambda \, ,
\end{cases} \\
\alpha_\nu^+ &=
\begin{cases}
a_\nu^+ & \text{for } e_\nu > \lambda \, , \\
-a_{-\nu} & \text{for } e_\nu < \lambda \, .
\end{cases}
\end{aligned}
\tag{6.30}
$$

We can say that the quasi-particle annihilation operators act as the annihilation operators of particles above Fermi level and as the creation operator below. The quasi-particle creation operators create particles in empty states and annihilate particles in occupied states.

Considering the case when $\Delta = 0$, the equation for the number of particles is:

$$n = \sum_{\nu > 0} \left(1 - \frac{e_\nu - \lambda}{\sqrt{(e_\nu - \lambda)^2}} \right) = \sum_{\nu > 0}^{\Omega} (1 + 1) = 2\Omega \ . \tag{6.31}$$

The number of particles is twice the number of Ω states below the Fermi level. Therefore, the ground state energy is:

$$E_0 = 2 \sum_{\nu > 0}^{\Omega} e_\nu V_\nu^2 = 2 \sum_{\nu > 0}^{\Omega} e_\nu \ . \tag{6.32}$$

In the particular case of $\Delta = 0$ superconductivity is not observed, since the pairs of nucleons are not created, so the nucleus continues to behave as a system of independent fermions in the average potential. In this case when $\Delta = 0$, the solution of the superconductivity equations is called "normal".

Let us now look at the case when the solution of nuclear superconductivity equations gives $\Delta \neq 0$, then, inequality is satisfied:

$$\sqrt{(e_\nu - \lambda)^2 + \Delta^2} > |e_\nu - \lambda| \ . \tag{6.33}$$

Now we put this inequality into the energy gap equation 6.26:

$$\frac{2}{G} = \sum_{\nu > 0} \frac{1}{\sqrt{(e_\nu - \lambda)^2 + \Delta^2}} < \sum_{\nu > 0} \frac{1}{|e_\nu - \lambda|} \ . \tag{6.34}$$

According to BCS theory, when the pairing strength is less than the critical value G_{cr}, the superconducting solution does not exist.

Fig. 6.1 shows the occupation probability V_ν^2 of the single-particle states as a function of their energies. In the case where the single-particle energy is much smaller than the Fermi level, $e_\nu \ll \lambda$, the occupied and empty probabilities are:

$$V_\nu^2 \simeq 1, \qquad U_\nu^2 \simeq 0.$$

If the state with $e_\nu = \lambda$, then $V_\nu^2 = U_\nu^2 = \frac{1}{2}$.
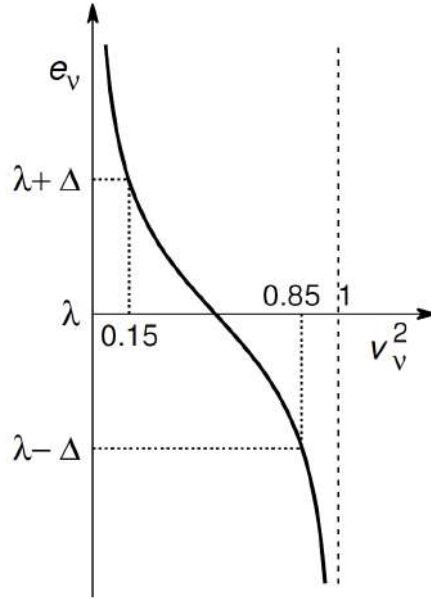
Figure 6.1: Occupation probability of single-particle states above and below the Fermi level in the BCS model.

In the case of $e_\nu \gg \lambda$:

$$V_\nu^2 \simeq 0 \ , \qquad U_\nu^2 \simeq 1 \ .$$

As can be seen, in the case of being far from the Fermi level, the coefficients U_ν^2 and v_ν^2 have the same values as for a free fermionic system. In a range close to the Fermi level with a window $(\lambda - \Delta, \lambda + \Delta)$ the pairing correlation are strongest. The occupation probability of the single-particle at the borders of such window is:

$$V_\nu^2 = \frac{1}{2}\left(1 - \frac{\Delta}{\Delta\sqrt{2}}\right) \approx 0.15 \quad \text{for} \quad e_\nu = \lambda + \Delta, \tag{6.35}$$

$$V_\nu^2 = \frac{1}{2}\left(1 + \frac{\Delta}{\Delta\sqrt{2}}\right) \approx 0.85 \quad \text{for} \quad e_\nu = \lambda - \Delta. \tag{6.36}$$

So, one can say that the superconductivity occurs mostly within this range 2Δ around the Fermi level.

6.3   Excited states of even nuclei

The break-up of a pair of particles and promotion them above the Fermi surface produces excitation in even nuclei. The wave function describing such an excited state contains

only components of an even number of particles. Therefore the lowest excitation must correspond to a two quasi-particle excitation of the form:

$$|\Phi_{12}\rangle = \alpha_{\nu_1}^+ \alpha_{\nu_2}^+ |\Phi_0\rangle \ . \tag{6.37}$$

The energy of this system is therefore equal to:

$$E_{12} = \langle\Phi_{12}|\hat{H}|\Phi_{12}\rangle = \langle\Phi_0|\alpha_{\nu_2}\alpha_{\nu_1}\left(E_0 + \sum_\nu \alpha_\nu \alpha_\nu^+\right)\alpha_{\nu_1}^+ \alpha_{\nu_2}^+ |\Phi_0\rangle = E_0 + E_{\nu_1} + E_{\nu_2} \ . \tag{6.38}$$

The excitation energy W of the state $|\Phi_{12}\rangle$ is given as:

$$W = E_{\nu_1} + E_{\nu_2} = \sqrt{\tilde{e}_{\nu_1}^2 + \Delta^2} + \sqrt{\tilde{e}_{\nu_2}^2 + \Delta^2} \ . \tag{6.39}$$

Observe that this energy is always larger than 2Δ and describes the energy *gap* between the ground state and the first excited state of the core pair. The lowest excited state we obtain by creating a pair of quasi-particles close to the Fermi level, when $e_{\nu_1} \approx e_{\nu_2} \approx \lambda$, so, then, $E_{\nu_1} \approx E_{\nu_2} \approx \Delta$, so, the first excited state is around 2Δ above the ground state.

6.4   Blocking effect

Through the variational method it will be possible to obtain the equations of superconductivity for the two-particle state:

$$\langle\Phi_{12}|\hat{H} - \lambda\hat{N}|\Phi_{12}\rangle = \langle\Phi_0|\alpha_{\nu_2}\alpha_{\nu_1}\left(\hat{H} - \lambda\hat{N}\right)\alpha_{\nu_1}^+ \alpha_{\nu_2}^+ |\Phi_0\rangle =$$

$$= \sum_{\nu>0} 2V_\nu^2 \tilde{e}_\nu - G\left(\sum_{\nu'>0} U_{\nu'} V_{\nu'}\right)^2 + G\sum_{\nu>0} V_\nu^4 +$$

$$+ \left(U_{\nu_1}^2 - V_{\nu_1}^2\right)\tilde{e}_{\nu_1} + 2G\left(\sum_{\nu'>0} U_{\nu'} V_{\nu'}\right)U_{\nu_1} V_{\nu_1} + \tag{6.40}$$

$$+ \left(U_{\nu_2}^2 - V_{\nu_2}^2\right)\tilde{e}_{\nu_2} + 2G\left(\sum_{\nu'>0} U_{\nu'} V_{\nu'}\right)U_{\nu_2} V_{\nu_2} \ ,$$

relative to V_ν, where $\nu \neq \nu_1$ and $\nu \neq \nu_2$. Therefore:

$$\frac{\delta \langle \Phi_{12} | \hat{H} - \lambda \hat{N} | \Phi_{12} \rangle}{\delta V_\nu} = 0 \ . \tag{6.41}$$

We define the energy gap $\Delta_{\nu_1 \nu_2}$ in a system with "blocked" states ν_1 and ν_2:

$$\Delta_{\nu 1 \nu_2} \equiv \sum_{\nu > 0, \nu \neq \nu_1, \nu \neq \nu_2} U_\nu V_\nu \ . \tag{6.42}$$

The occupancy probabilities are:

$$U_\nu^2 = \frac{1}{2} \left(1 + \frac{\tilde{e}_\nu}{\sqrt{\tilde{e}_\nu^2 + \Delta_{\nu_1 \nu_2}^2}} \right), \qquad V_\nu^2 = \frac{1}{2} \left(1 - \frac{\tilde{e}_\nu}{\sqrt{\tilde{e}_\nu^2 + \Delta_{\nu_1 \nu_2}^2}} \right) \ . \tag{6.43}$$

The particle number equation

$$\langle \Phi_{12} | \hat{N} | \Phi_{12} \rangle = n \ , \tag{6.44}$$

we can write as:

$$2 + \sum_{\nu = 0, \nu \neq \nu_1, \nu \neq \nu_2} \left(1 + \frac{\tilde{e}_\nu}{\sqrt{\tilde{e}_\nu^2 + \Delta_{\nu_1 \nu_2}^2}} \right) = n \ . \tag{6.45}$$

Then, the energy gap equation:

$$\frac{2}{G} = \sum_{\nu > 0, \nu \neq \nu_1, \nu \neq \nu_2} \left(\frac{1}{\sqrt{\tilde{e}_\nu^2 + \Delta_{\nu_1 \nu_2}^2}} \right) \ . \tag{6.46}$$

Therefore, the equation of the two-particle $|\Phi_{12}\rangle$ takes the form:

$$E_{12} = \langle \Phi_{12} | \hat{H} | \Phi_{12} \rangle = e_{\nu_1} + e_{\nu_2} + 2 \sum_{\nu > 0, \nu \neq \nu_1, \nu \neq \nu_2} e_\nu V_\nu^2 - \frac{\Delta_{\nu_1 \nu_2}^2}{G} -$$
$$- G \sum_{\nu > 0, \nu \neq \nu_1, \nu \neq \nu_2} V_\nu^4 \ . \tag{6.47}$$

It is found that the states occupied by quasi-particles $|\nu_1\rangle$ and $|\nu_2\rangle$ are removed from the sums in the superconductivity equations. Since these states are "blocked" for the pairing interaction.
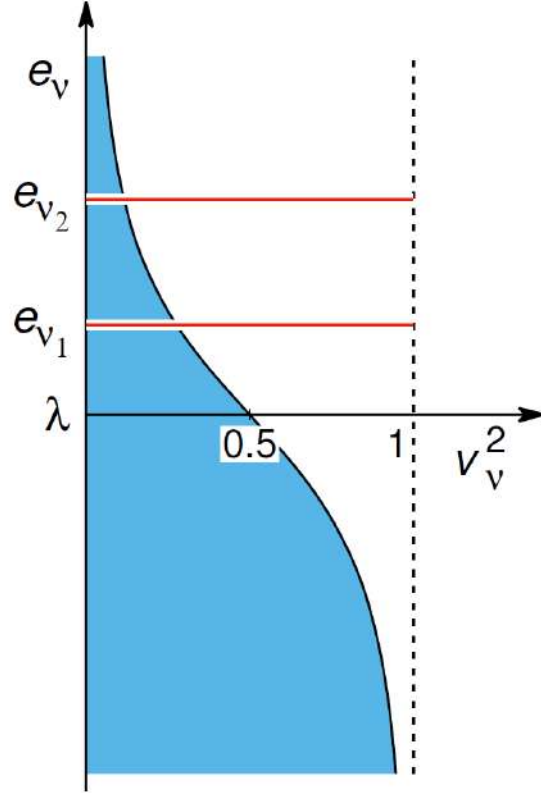
Figure 6.2: Excited states of the even nuclei in BCS model.

The corresponding wave function is:

$$
\begin{aligned}
|\Phi_{12}\rangle = \alpha_{\nu_1}^+ \alpha_{\nu_2}^+ |\Phi_0\rangle &= \left(U_{\nu_1}\alpha_{\nu_1}^+ + V_{\nu_1}\alpha_{-\nu_1}\right)\left(U_{\nu_2}\alpha_{\nu_2}^+ + V_{\nu_2}\alpha_{-\nu_2}\right)|\Phi_0\rangle = \\
&= \alpha_{\nu_1}^+ \alpha_{\nu_2}^+ \prod_{\nu>0,\nu\neq\nu_1,\nu\neq\nu_2} \left(U_\nu + V_\nu \alpha_\nu^+ \alpha_{-\nu}^+\right)|0\rangle \, ,
\end{aligned}
\tag{6.48}
$$

The probability of occupation by single particles of the states ν_1 and ν_2 is equal to 1, while the other states by pairs of particles with probability V_ν^2.

In the figure 6.2 we can see the blocking effect in the two-particle state. The ν_1 and ν_2 states are totally filled by single particles.

The blocking effect loses relevance for a larger number of particles and in such cases is usually not taken into account.

6.5   Odd nuclei

To describe the ground and excited states of systems with an odd number of nucleons we consider single quasi-particle functions, where single-particle states are filled by pairs of particles and also by a single nucleon or hole.

Therefore, the function of a system consisting of an odd number of nucleons can be represented as:

$$|\Phi_1^{odd}\rangle = \alpha_{\nu_1}^+|\Phi_0\rangle \ . \tag{6.49}$$

The creation of a quasi-particle in the ν_1 state has a contribution to the ground state energy of an even system and in an additional energy term E_{ν_1} has to be added. Thus, the energy of an odd system is:

$$E_1^{odd} = \langle\Phi_0|\alpha_{\nu_1}\hat{H}\alpha_{\nu_1}^+|\Phi_0\rangle = E_0 + E_{\nu_1} \ , \ . \tag{6.50}$$

When we create a quasi-particle in the state closest to the Fermi level $e_{\nu_0} \approx \lambda : \alpha_{\nu_0}^+|\Phi_0\rangle$, then:

$$E_1^{odd} = \langle\Phi_0|\alpha_{\nu_1}\hat{H}\alpha_{\nu_1}^+|\Phi_0\rangle \approx E_0 + \Delta \ . \tag{6.51}$$

The excitation energy W of the odd nucleus that writes:

$$W = \sqrt{\tilde{e}_{\nu_1}^2 + \Delta^2} - \Delta < |\tilde{e}_{\nu_1}| \ . \tag{6.52}$$

As can be seen, the excitation energy corresponding to a free fermion is larger than the excitation energy of interacting particles. Pairing forces bring the single-particle energy levels closer together.

After the minimizing of the energy in the odd-system of $V_\nu(\nu \neq \nu_1)$, we can obtain a system of BCS equations where the state ν_1 has been blocked:

$$U_\nu^2 = \frac{1}{2}\left(1 + \frac{\tilde{e}_\nu}{\sqrt{\tilde{e}_\nu^2 + \Delta_{\nu_1}^2}}\right), \qquad V_\nu^2 = \frac{1}{2}\left(1 - \frac{\tilde{e}_\nu}{\sqrt{\tilde{e}_\nu^2 + \Delta_{\nu_1}^2}}\right) \ . \tag{6.53}$$

$$n = 1 + 2 \sum_{\nu>0,\nu\neq\nu_1} \left(1 - \frac{\tilde{e}_\nu}{\sqrt{\tilde{e}_\nu^2 + \Delta_{\nu_1}^2}} \right) . \tag{6.54}$$

$$\frac{2}{G} \sum_{\nu>0,\nu\neq\nu_1} \left(\frac{1}{\sqrt{\tilde{e}_\nu^2 + \Delta_{\nu_1}^2}} \right) , \qquad \text{where} \qquad \Delta_{\nu'} \equiv G \sum_{\nu>0,\nu\neq\nu_1} U_\nu V_\nu . \tag{6.55}$$

Figure 6.3 shows the smoothed occupation probability in all levels except the state ν_1 in which is located an odd particle.

Figure 6.3: Excited states of the odd nuclei in BCS model.
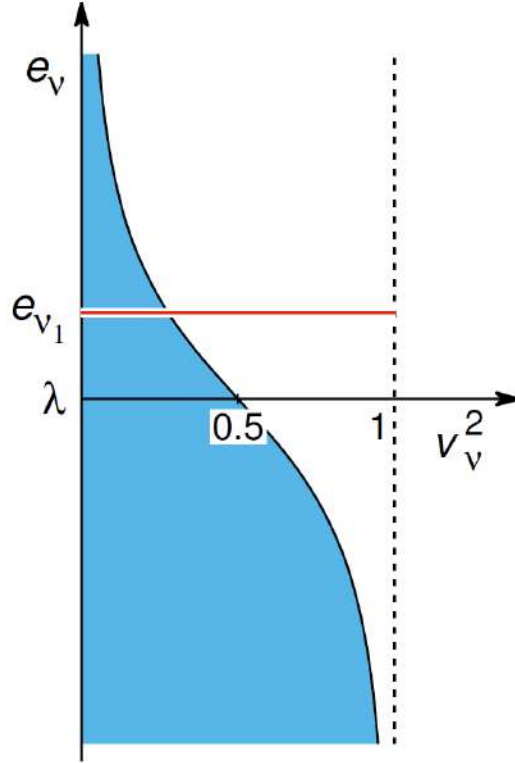
The energy of the odd number particle system is:

$$E_1^{odd} = e_{\nu_1} + 2 \sum_{\nu>0,\nu\neq\nu_1} V_\nu^2 e_\nu - \frac{\Delta_{\nu_1}^2}{G} - G \sum_{\nu>0,\nu\neq\nu_1} V_\nu^4 . \tag{6.56}$$

We check that this result is slightly different from the equation 6.50, because it takes into account the blocking of ν_1 level corresponding to the odd nucleon.

7 Deformed nuclei

We will now come to calculate the potential energy of deformed atomic nuclei in the macroscopic-microscopic method. Due to the spontaneous symmetry breaking effects known in the nature, the majority of atomic nuclei are deformed in their ground states. From a mathematical point of view in the macroscopic-microscopic model this effect is caused by the quantum shell and pairing interactions as they turn out to be strongly oscillating functions of nuclear deformation. Recall that previously discussed liquid drop energy alone has its minimum value for the spherical shape of nuclear drop.

We have already studied the macroscopic models with strong interactions between nucleons forming a drop of nuclear matter, such as e.g. the Lublin-Strasbourg Drop (LSD) model. We will also consider another approach of a microscopic nature, which treats only free particles moving within an average mean-field potential. Due to quantum interactions, the energy levels of those particles can be grouped in bundles forming a kind of energy shells between which gaps are observed. It is now important to describe how to separate shell and short-range pairing interactions from averaged nuclear properties. The effects of long-range forces will be treated by an additional collective coordinate, in this case, the nuclear deformation.

To find the equilibrium deformation of the nucleus, which corresponds to its minimum energy, one has to perform the total energy calculations on a discrete grid of one or more deformation parameters. For this purpose, we make use of a specific set of the Fourier deformation parameters described in Chapter 3, in which the energy is minimized.

To obtain a macroscopic description of the nucleus energy, one can use one of the liquid drop model described in Chapter 2. We are using in the following the Lublin-Strasbourg Drop formula given by Eq. 2.16. The macroscopic energy of non-rotating nuclei has a minimum at the spherical shape, as we can see in the Fig. 7.1, where the energy of the liquid drop is represented with a thin solid line as a function of the nucleus elongation (coordinate q_2). As already mentioned, the deformation of a nucleus in its equilibrium state can only be explained by the presence of microscopic effects, i.e. by the shell and pairing energy correction shown in Fig. 7.1.
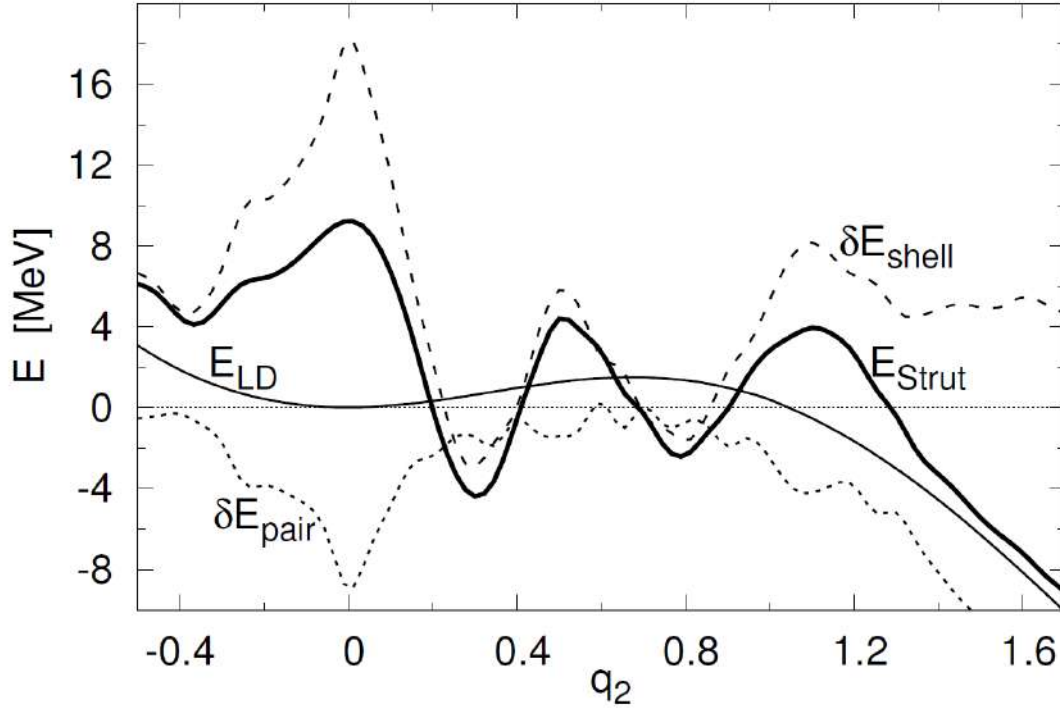
Figure 7.1: Schematic plot of the total potential energy as a function of the elongation parameter q_2. The macroscopic energy E_{LD} is represented by thin solid line, the shell energy δE_{shell} by dashed line, the pairing correction δE_{pair} by dotted line, and the total Strutinsky energy $E_{Strut} = E_{LD} + \delta E_{shell} + \delta_{pair}$ with thick solid line.

7.1   Summation of single-particle energies

Since atomic nuclei undergo deformations due to the presence of quantal effects, becoming non-spherical in their ground state, microscopic contributions to their potential energy are calculated from the single-particle energies in deformed mean-field potentials.

One of the first models that tried to describe the sum of the energies of individual particles was the Mottelson-Nilsson method [B. Mottelson, S. G. Nilsson, Phys. Rev. **99**, 1615 (1955)]:

$$E_{MN}(N, Z, def) = \sum_{\nu=1}^{\nu_F^n} e_\nu^n + \sum_{\nu=1}^{\nu_F^p} e_\nu^p + E_{Coul} , \tag{7.1}$$

where the single-particle energies e_ν of protons (p) and neutrons (n) are calculated by diagonalization of the single-particle Hamiltonian $\hat{h}$ with a deformed mean-field potential $V(\mathbf{r}; def)$:

$$\hat{h} = \hat{T} + V(\mathbf{r}; def) . \tag{7.2}$$

The Coulomb effect from protons may be calculated by the integral after all single-particle

coordinates of protons:

$$E_{Coul} = \sum_{i>j} \int \int ... \int \Psi^*(r_1, ..., r_z) \frac{e^2}{|r_i - r_j|} \Psi(r_1, ..., r_z)\, d\tau_1...d\tau_z \ , \qquad (7.3)$$

where Ψ is a Slater determinant of the single particle functions. If we replace the squares of the functions by the charge densities ρ_i, we get:

$$E_{Coul} = \sum_{i>j} \int \int \rho_i(r_i)\rho_j(r_j) \frac{e^2}{|r_i - r_j|}\, d\tau_i...d\tau_j \ . \qquad (7.4)$$

The last integral is usually evaluated assuming the uniform charge distribution like it is described in Chapter 2.

The sum of the single-particle energies and the Coulomb energy has a minimum for non-zero deformations, but does not describe the experimentally obtained masses nor the fission barrier heights of nuclei. This is because the interactions between nucleons were taken into account twice in the total energy. Therefore, the shell effects must be separated from the total energy.

An improvement of the Mottelson-Nilsson method by including short-range pairing correlations was proposed by Bés and Szymanski [D. R. Bés, Z. Szymanski, Nucl. Phys. **28**, 42 (1961)], who has added the Coulomb energy of the nucleus to the BCS energies of protons and neutrons:

$$\begin{aligned}
E_{BS} = &\left(\sum_{\nu=1}^{V_F} 2e_\nu V_\nu^2 - \frac{\Delta^2}{G} - G \sum_{\nu>0} V_\nu^4 \right)_p + \\
&+ \left(\sum_{\nu=1}^{V_F} 2e_\nu V_\nu^2 - \frac{\Delta^2}{G} - G \sum_{\nu>0} V_\nu^4 \right)_n + E_{Coul}.
\end{aligned} \qquad (7.5)$$

Helas, the Bés and Szymanski method was not free from the double counting of the inter-nucleon interaction energy. A proper treatment of this problem was proposed five years later by Strutinsky [V. M. Strutinsky, Nucl. Phys. A**95**, 420 (1967)].

7.2   Macroscopic-microscopic method

As seen in the previous section, there was a problem in calculating the potential energy values which was the double sum of the interactions between two nucleons, to avoid this, Strutinsky devised a method to normalize the energy in liquid drop or any other macroscopic energy, making use of a microscopic energy correction. This correction would take into account the energy due to the liquid drop, the shell effects and the pairing interactions.

$$E_{Strut} = E_{LD} + \delta E_{shell} + \delta E_{pair} \ . \tag{7.6}$$

The different contributions to the total energy considered by Strutinsky 7.2 are shown in Fig. 7.1.

The contribution of the pairing correction is described as the difference between the calculated microscopic energy with and without short-range interactions, from which the mean pairing energy term $\langle Epair \rangle \approx -2.3 \text{MeV}$ is subtracted, which has already been taken into account in the phenomenological parameters of the liquid drop model:

$$\delta E_{pair} = E_{BCS} - 2 \sum_{\nu>0}^{V_F} e_\nu - \langle E_{pair} \rangle \ . \tag{7.7}$$

While, the shell correction is calculated as the difference between the sum of the single-particle energies and an average energy ($\tilde{E}$) in the shell effects are smoothed:

$$\delta E_{shell} = 2 \sum_{\nu>0}^{V_F} e_\nu - \tilde{E}. \tag{7.8}$$

Inserting Eqs. 7.7 and 7.8 into the equation , we obtain the final equation for the potential energy:

$$E_{Strut} = E_{LD} + E_{BCS} - \delta E_{shell} - \langle E_{pair} \rangle - \tilde{E} \ . \tag{7.9}$$

It has been found that this correction proposed by Strutinsky describes well the shapes and energies of the atomic nuclei, both the ground states and the fission barrier widths and heights. We must take into account that in this Strutinsky method, two different ideas are associated, on the one hand, the strong nuclear macroscopic drop interactions and on the other hand independent particles moving in an average potential. In the next

section, we present the Strutinsky way of evaluating the energy of the nucleus in which the shell structure is washed out.

8   Strutinsky shell correction

To explain the Strutinsky shell correction method, we will consider a system of A nucleons with coordinates $x_i = r_i, s_i, t_i$, containing respectively their positions in the coordinate system, spin and isospin degrees of freedom, where $i = 1, ..., A$. The i-th nucleon density will also be involved, which will be defined as $\rho_i(x_i) = \varphi^*(x_i)\varphi(x_i)$, where $\varphi(x_i)$ is the single-particle wave function. To describe the energy of this system, we will consider two parts of the total energy: the single-particle kinetic energy $T_i(x_i)$ and the potential originating from the two particles' interaction $V(x_i, x_j)$:

$$E = \sum_{i=1}^{A} \int T_i(x_i)\rho_i(x_i)\, dx_i + \sum_{i>j}^{A} \int \int \rho_i(x_i)V(x_i, x_j)\rho_j(x_j)\, dx_i dx_j \ . \tag{8.1}$$

Let us also introduce the single-particle mean potential given by:

$$U(x_i) \equiv \sum_{i\neq j}^{A} \int V(x_i, x_j)\rho_j(x_j)\, dx_j \ . \tag{8.2}$$

Now, Eq. 8.1 for the total energy can be written as:

$$E = \sum_{i=1}^{A} \int [T_i(x_i) + \frac{1}{2}U_i(x_i)]\rho_i(x_i)\, dx_i \ . \tag{8.3}$$

Note the factor $1/2$ in front of the second term, which originates from the fact that the summation in the second term of Eq. 8.1 was performed for $i > j$. So, we avoid in this way the double counting of the nucleon-nucleon interaction.

The next important step proposed by Strutinsky was the separation of the density ρ into two parts, smooth part $\bar{\rho}$ and the fluctuating part $\delta\rho$, which origins the shell effects:

$$\rho_i(x_i) = \bar{\rho}_i(x_i) + \delta\rho_i(x_i) \ . \tag{8.4}$$

Applying the smoothed density $\bar{\rho}$ to Eq. 8.1 one can evaluate the non-fluctuating part of

energy:

$$\tilde{E} = \sum_{i=1}^{A} \int T_i(x_i)\bar{\rho}_i(x_i)\, dx_i + \sum_{i>j}^{A} \int \int \bar{\rho}_i(x_i)V(x_i,x_j)\bar{\rho}_j(x_j)\, dx_i dx_j \ . \tag{8.5}$$

Thus, we can now write the formula for the total energy:

$$E = \tilde{E} + \left\{ \sum_{i=1}^{A} \int T_i(x_i) + \sum_{i\neq j}^{A} \int V(x_i,x_j)\bar{\rho}_j(x_j)\, dx_j \right\} d\rho_i(x_i) dx_i +$$
$$+\text{terms of higher powers of } \delta\rho \ . \tag{8.6}$$

Let us define now the smoothed mean-field potential:

$$\tilde{U}(x_i) = \sum_{i\neq j}^{A} \int V(x_i,x_j)\bar{\rho}_j(x_j)\, dx_j \ . \tag{8.7}$$

We now write the formula for the total energy including the shell correction:

$$E = \tilde{E} + \sum_{i\neq j}^{A} \int \left[T(x_i) + \tilde{U}(x_i) \right] \left[\rho_i(x_i) - \bar{\rho}_j(x_i) \right] dx_i \equiv E_{LD} + \delta E_{shell} \ . \tag{8.8}$$
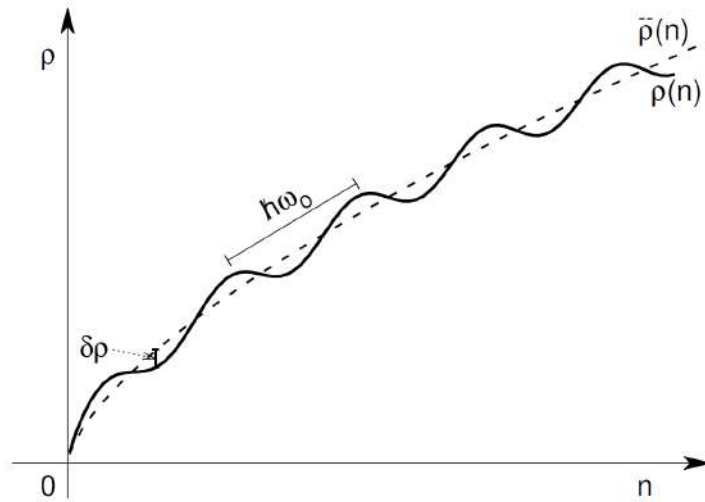

Figure 8.1: Density of single particle levels (ρ) and its smooth ($\tilde{\rho}$) and fluctuating ($\delta\rho$) parts as a function of number of particles n. Here $\hbar\omega_0$ is the energy distance between the major harmonic oscillator shells.

The smoothed energy is given in the Strutinsky method in the form of an integral over

the single-particle energies:

$$\tilde{E} = 2 \int_{-\infty}^{\tilde{\lambda}} \bar{\rho}(e)e \, de. \tag{8.9}$$

The upper limit of the integral corresponds to the Fermi level $\tilde{\lambda}$ in a nucleus with a smoothed shell structure and it is calculated from the conservation condition of the number of particles:

$$Z(N) = 2 \int_{-\infty}^{\tilde{\lambda}} \bar{\rho}(e) \, de \rightarrow \tilde{\lambda} \, . \tag{8.10}$$

To obtain the function $\bar{\rho}(e)$ we average the true density of single particle ρ using a weight function $j(e, e')$:

$$\bar{\rho}(e) = \int_{-\infty}^{-\infty} \rho(e')j(e, e') \, de' \, . \tag{8.11}$$

The weight function must be normalized:

$$\int_{-\infty}^{\infty} j(e, e') \, de' = 1. \tag{8.12}$$

In his original paper, Strutinsky has used for the weight function the Gauss function multiplied by a correction polynomial of the second order. Nowadays, one takes for this purpose a six or higher order polynomial:

$$j_6(u) = \frac{1}{\gamma_S \sqrt{\pi}} e^{-u^2} \left(\frac{35}{16} - \frac{35}{8}u^2 + \frac{7}{4}u^4 - \frac{1}{6}u^6 \right) , \tag{8.13}$$

where $u = (e - e')/\gamma$ and $\gamma \approx \hbar\omega_0$ is the smearing width.

Let us now summarize the steps taken to calculate the potential energy using the Strutinsky shell correction method for an even number of particles:

1. We solve the eigenproblem of the single-particle Hamiltonian $\hat{h}$ with a mean-field potential dependent on the deformation:

$$\hat{h}|\nu\rangle = e_\nu |\nu\rangle \, ,$$

   we uses for further calculations the single-particle energy e_ν as well as the corresponding eigenfunctions $|\nu\rangle$ of a nucleus.

2. We evaluate the integral for the smooth density of the single-particle levels:

$$\bar{\rho}(e) = \frac{1}{\gamma\sqrt{\pi}} \int_{-\infty}^{\infty} \rho(e') e^{-\left(\frac{e-e'}{\gamma}\right)^2} f\left(\frac{e-e'}{\gamma}\right) de' , \qquad (8.14)$$

taking the smoothing constant γ approximately equal to the average distances between major shells $(\hbar\mathring{w}_0)$ and the the corresponding correction polynomials f.

3. For nucleus with Z protons and N neutrons we define the Fermi level $\tilde{\lambda}$ from the condition:

$$\int_{-\infty}^{\tilde{\lambda}} \bar{\rho}(e) \, de = Z(N). \qquad (8.15)$$

4. Then we evaluate the energy of the spectrum of smoothed levels:

$$\tilde{E} = 2 \int_{-\infty}^{\tilde{\lambda}} \bar{\rho}(e) e \, de . \qquad (8.16)$$

5. Now it is the turn to calculate the energy due to the BCS system of equations.:

$$E_{BCS} = \sum_{\nu>0} 2e_\nu V_\nu^2 - \frac{\Delta^2}{G} - G \sum_{\nu>0} V_\nu^4. \qquad (8.17)$$

6. Then one has to evaluate the macroscopic energy of the nucleus in the given deformation, which in the LD model reads as:

$$E_{LD} = a_2(1-k^2)A^{2/3}[B_s(def)-1] + \frac{3}{5}\frac{Z^2 e^2}{r_0}A^{1/3}[B_c(def)-1] . \qquad (8.18)$$

7. The total energy nucleus in the Strutinsky model is given by the formula:

$$E_{Strut}(def) = E_{LD} + E_{BCS} - \langle E_{pair} \rangle - \tilde{E} . \qquad (8.19)$$

8. The local minima of the above energy one obtains by performing a minimization with respect the deformation parameters:

$$\text{minimum}\{E_{Strut}(def)\} \; ' \rightarrow \quad def_{min} . \qquad (8.20)$$

In this way, we can calculate all the local minima. The lowest of these local minima

corresponds to the ground state, which is the equilibrium point of the nucleus, def_{eq}.

9. The ground-state energy of the nucleus is given by the Strutinsky energy in the equilibrium point:

$$E_0 = E_{Strut}(def_{eq}) \ . \tag{8.21}$$

As we have seen, Strutinsky's method unifies the single-particle and pairing microscopic effects with the macroscopic ones.

9 Results of the calculation of GS, saddle points and barrier heights

In this section, we show the plots of the potential energy corresponding to a selected isotope of each nucleus for proton number Z between 90 and 110. In each figure, two kinds of two dimensional maps are shown (See Appendix C for more information on the method used for the calculation of energies, GS and saddle points). The one at the l.h.s. (a) corresponds to the (q_2, q_3) cross section of the full 4D potential energy function, while two other deformation parameters q_4 and η are taken as equal to zero. The maps at the r.h.s. (b) shows similar cross-sections but in the plane (q_2, q_4) assuming $q_3 = 0$ and $\eta = 0$.

The graphs shown in this section are only a sample, as for each element we have studied about 10 to 15, or even more, isotopes. We have chosen isotopes from the middle part of the isotopic chains because the resulting PES for these isotopes allow to reproduce the ground-state masses or the fission characteristics with a reasonable discrepancy compared to the experimental data. For the nuclei lying to the left and right from them this reproduction sometimes appears to be worse.

In light thorium nuclei, the left-right asymmetry (q_3) appears in the ground state while this effect disappears in the heavier isotopes. The second barrier heights of almost all considered isotopes are significantly reduced (even by a few MeV) when taking into account this asymmetry while the the first barrier is unchanged in the case of heavier than Th nuclei. The deformation parameter q_4 is chosen in such a way that the liquid drop (LD)
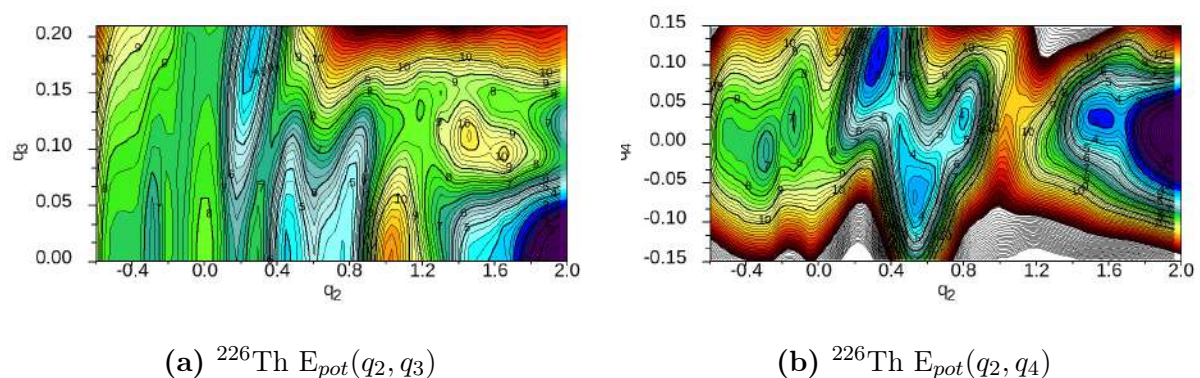

(a) ^{226}Th E$_{pot}(q_2, q_3)$ (b) ^{226}Th E$_{pot}(q_2, q_4)$

Figure 9.1: Potential energy surfaces for ^{226}Th.

(a) ^{234}U E$_{pot}(q_2, q_3)$
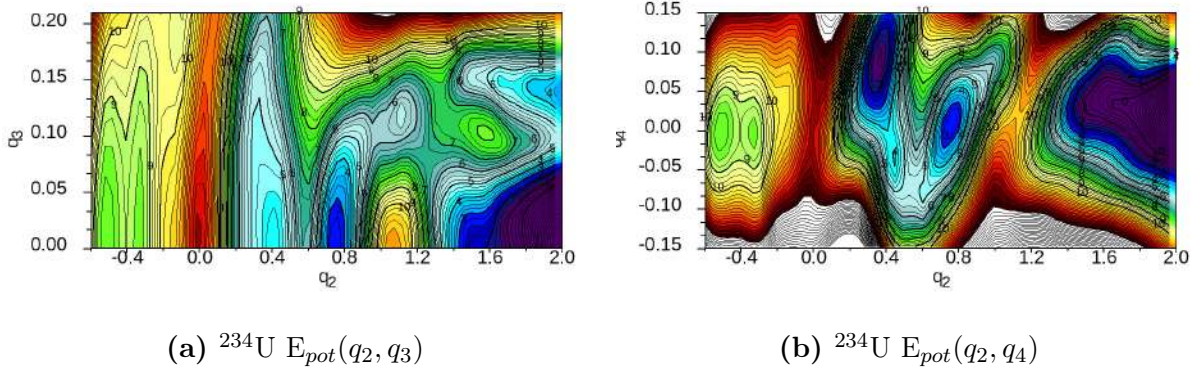
(b) ^{234}U E$_{pot}(q_2, q_4)$

Figure 9.2: Potential energy surfaces for ^{234}U.

(a) ^{236}Pu E$_{pot}(q_2, q_3)$
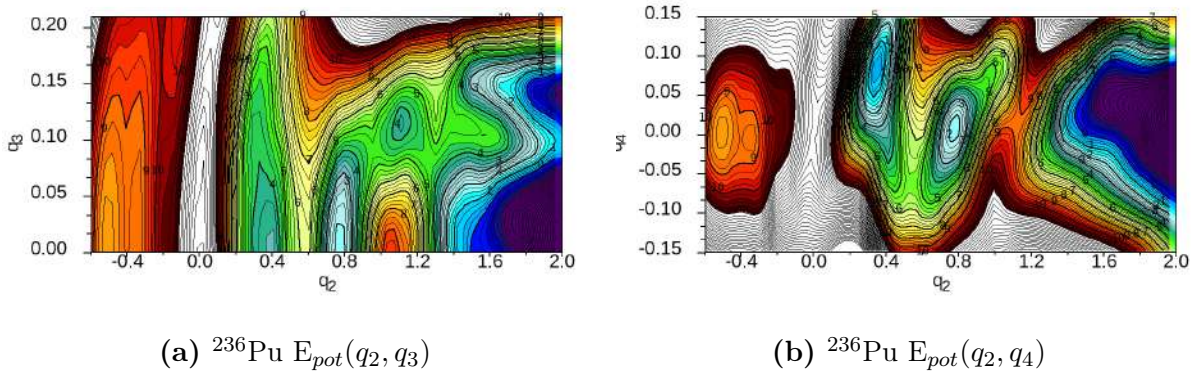
(b) ^{236}Pu E$_{pot}(q_2, q_4)$

Figure 9.3: Potential energy surfaces for ^{236}Pu.

path to fission corresponds roughly to $q_4 = 0$ line. Looking at energy maps $E_{pot}(q_2, q_4)$ one can see that the microscopic energy correction significantly modifies this LD picture: the ground state (GS), isomeric minima and the saddle points frequently correspond to non-zero values of q_4. Recall that this parameter, depending on whereas it is positive or negative, is responsible for creating the diamond-like or "necked" nuclear shape.

In the case of uranium isotopes, unlike in thorium, we can observe an important difference, since the GS is left-right symmetric, which is maintained throughout the whole fission path. The coordinate q_4 is then decreasing from $q_2 = 0.8$ to zero.

With plutonium, although both the GS and the scission point correspond to a mass-symmetrical shapes with $q_3 = 0$, we can observe that this symmetry is briefly broken in the vicinity of the second saddle point at approximately $q_2 = 1.1$. With respect to the q_4 coordinate, we observe that its behavior is very similar to that of uranium nuclei. In the next element, curium, the fission path shows a behaviour very similar to that of Pu, especially remarkable is that brief mass-symmetry breaking also in the vicinity of $q_2 \approx 1.1$.

(a) ^{240}Cm E$_{pot}(q_2, q_3)$ **(b)** ^{240}Cm E$_{pot}(q_2, q_4)$
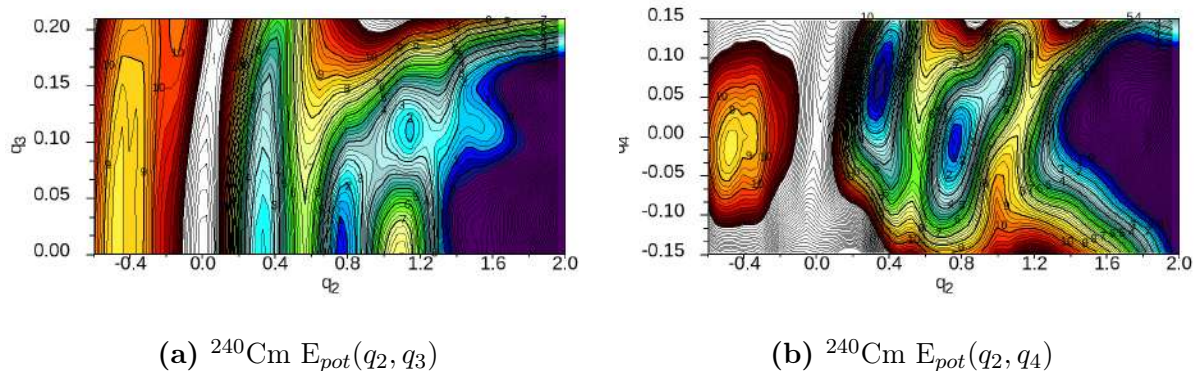
Figure 9.4: Potential energy surfaces for ^{240}Cm.

(a) ^{250}Cf E$_{pot}(q_2, q_3)$ **(b)** ^{250}Cf E$_{pot}(q_2, q_4)$
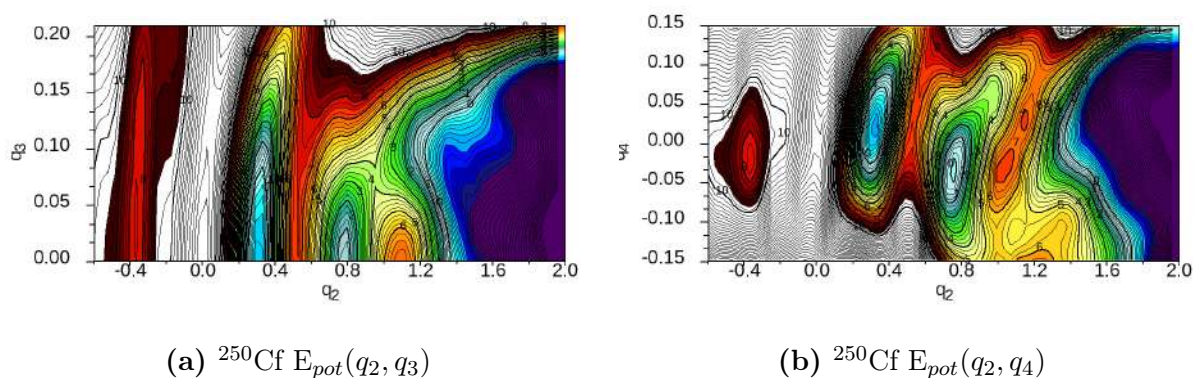
Figure 9.5: Potential energy surfaces for ^{250}Cf.

(a) ^{252}Fm E$_{pot}(q_2, q_3)$ **(b)** ^{252}Fm E$_{pot}(q_2, q_4)$
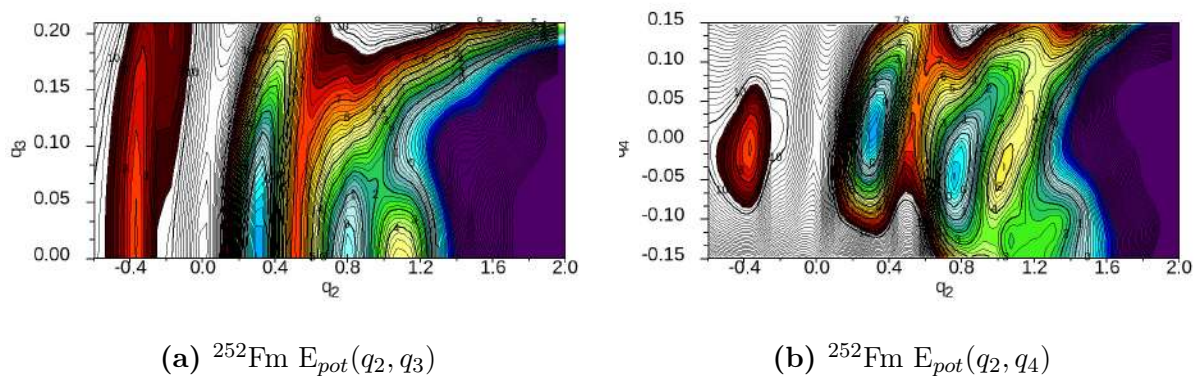
Figure 9.6: Potential energy surfaces for ^{252}Fm.

Starting from the californium, the following elements: Fm, No and Rf shown in this section have different behavior on the q_3 coordinate. Although all of them start from mass-symmetric GS, $q_3 = 0$, from the second saddle point, this symmetry is broken, just like in the 3 isotopic chains mentioned above, but this time there is an important difference, and that is that the symmetry is no longer recovered, reaching the fission configuration with one fragment larger than the other.

(a) ^{252}No $E_{pot}(q_2, q_3)$ **(b)** ^{252}No $E_{pot}(q_2, q_4)$
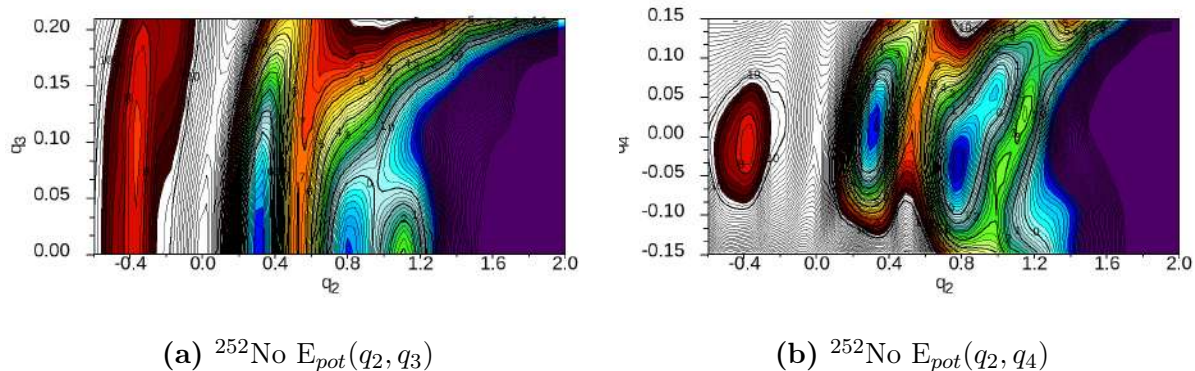
Figure 9.7: Potential energy surfaces for ^{252}No.

(a) ^{272}Rf $E_{pot}(q_2, q_3)$ **(b)** ^{272}Rf $E_{pot}(q_2, q_4)$
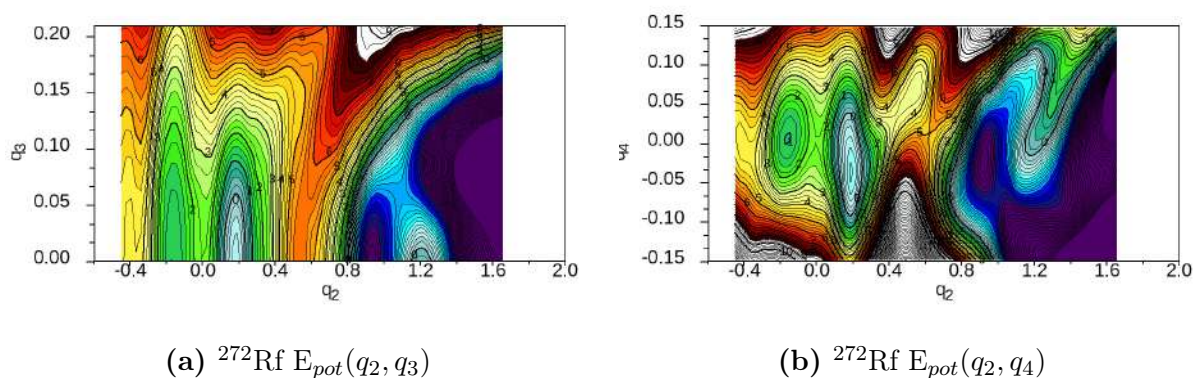
Figure 9.8: Potential energy surfaces for ^{272}Rf.

A remarkable peculiarity is the fact that all the isotopes seen in this section have the GS located at approximately $q_2 = 0.4$, but in the last isotopic chain shown, rutherfordium, the GS appears earlier, taking a value slightly lower than $q_2 = 0.2$.

Regarding the q_4 coordinate, we can observe that after the GS, it always remains very close to the value zero.

Due to the large number of maps on Potential Energy Surfaces (PES), we have decided to attach a link from which all these maps can be accessed on the internet: https://tpd.umcs.pl/index.php/s/RAEtp2zkZbXMEZa.

10 Fitting the average pairing strength G

Although we have so far used the BCS monopole pairing approach with great success, in this section we want to propose a slight modification of the pairing strength value, which would allow us to obtain the theoretical equilibrium masses of, in particular, actinide nuclei a little closer to the experimental data. For this purpose, it would be necessary to re-adjust the intensity of the pairing forces G in such a way that the pairing gaps $\Delta_q^{(exp)}$ for protons and neutrons estimated from the experimental equilibrium masses are reproduced through the above presented BCS-like approximation in these nuclei in the best possible way. This fit will be made from the measured mass excesses of neighboring heavy and superheavy nuclei, as tabulated, for example, in Ref.(43).

We can express the energy gap Δ_q, ($q = n$ or p) that occurs in the pairing interaction for neutrons and protons like $\Delta_q = E_{int}^{(q)}/2$, where $E_{int}^{(q)}$ is the interaction energy between two nucleons of type q.

For the case of a nucleus with a number of protons Z and neutrons N and with separation energies $S(N_q)$, the energy can be expressed as:

$$E_{int}^{(q)} = S(N_q) - \frac{1}{2}[S(N_q + 1) + S(N_q - 1)]. \tag{10.1}$$

The pairing gaps can be expressed as a combination of the experimental binding energies $B(N_q)$ using the following formula:

$$\Delta_q^{(exp)} = \frac{1}{4}\left[2B(N_q) - B(N_q + 1) - B(N_q - 1)\right]. \tag{10.2}$$

As mentioned above, the pairing strength G for nuclei with $Z = 90 - 100$ can be calculated so that the gaps for neutrons and protons $\Delta_q(G)$ calculated in the BCS approach presented in the previous sections are as close as possible to their experimental values given by the equation (10.2). To achieve it, one has to minimize with respect to the pairing strength G the sum of distances between the experimental (Δ_{exp}) and predicted energy gap ($\Delta(G)$) for all discussed nuclei:

$$\sum_{\text{set}} |\Delta_q^{(exp)} - \Delta_q(G)| , \tag{10.3}$$
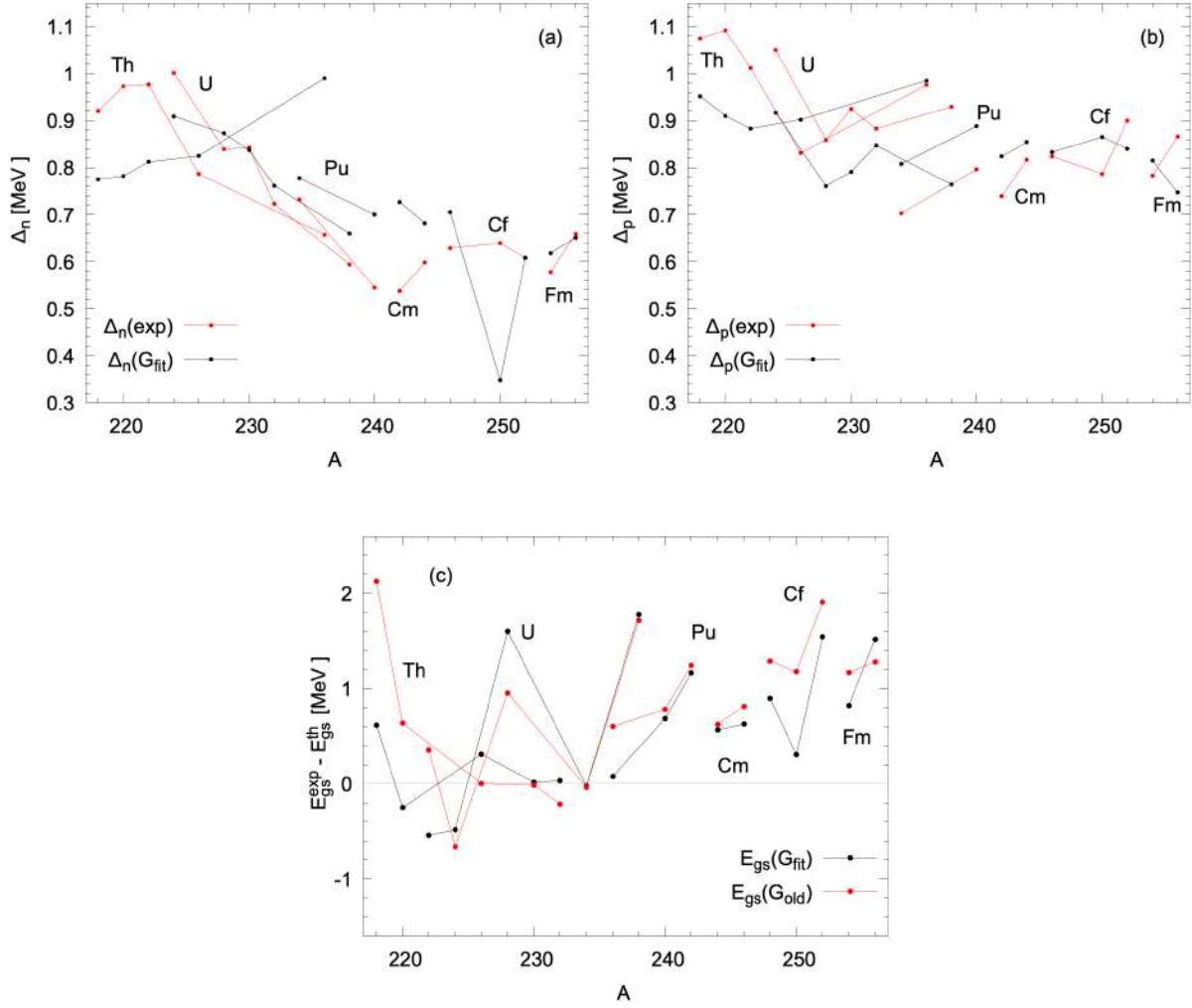
Figure 10.1: Comparison between calculated (in black) and empirical (in red) neutron (a) and proton (b) pairing gaps for the discussed isotopic chains from $Z = 90$ up to $Z = 100$. Panel (c) displays the largest differences between experimental and calculated ground-state masses, evaluated with the pairing strength of the Ref. (43) (red) and the one obtained from Eq.(10.4)(black).

where the sum goes over the whole set of the considered nuclei.

We used the following simple analytical expression for the pairing strength:

$$G\,A = g_0 + g_1\,(N - Z)\ . \tag{10.4}$$

This formula has two free parameters, g_0 and g_1 chosen to minimize the sum in Eq. (10.3). After performing numerous calculations with the masses of actinide isotopes, we have found that the values $g_0 = 18.35$ MeV and $g_1 = 0.103$ MeV for protons and $g_0 = 24.1$ MeV and $g_1 = -0.135$ MeV for neutrons.

In Fig. 10.1 (a) and (b) we can observe the quality of this adjustment, where the values of the pairing gaps calculated with this Eq. (10.4) are very close to the experimental values obtained with Eq. (10.2).

It can be seen that the largest difference for neutrons does not exceed 0.35 MeV in the cases ^{236}Th and ^{250}Cf, and for protons, this difference is always below 0.2 MeV. We can also note that the average of these differences between theoretical and experimental results for neutrons and protons is about 0.12 MeV.

In panel (c) of Fig. 10.1 made for the same set of nuclei as in panels (a) and (b), we show the macroscopic-microscopic ground-state energy, relative to the experimental data, with the pairing corrections obtained using the formula Eq. (10.4) (black dots) and a previous fit of the pairing strength (red dots) within the same projected BCS-like formalism as presented above (see (43) and references therein), where the dependence of the nucleons number of G is of the form:

$$G_q \cdot N_q^{2/3} = g_{(0)} \ , \quad q = \{n, p\} \ . \tag{10.5}$$

This formula contains a single parameter $g_{(0)}$ only the same for protons and neutrons and equal $g_q^{(0)} = 0.28\hbar\omega_0$, where the value of $\hbar\omega_0 = 41/A^{1/3}$ MeV. This value of g_0 fitted to nuclei from different mass regions is widely used in macroscopic-microscopic calculations. We have also used it when obtaining the results presented in Chapter 9.

It can be seen in Fig. 10.1 that this new pairing-strength fit, Eq. (10.4), achieves for most of the considered nuclei, a better approximation of the experimental ground-state masses as compared to the previous formula (10.5), only in the isotopes of uranium ^{222,226,228}U and of fermium ^{256}Fm the fit is worse. For example, in the case of ^{228}U, the difference between the results given by these two formulae is about half a MeV.

Considering this new fit which gives essentially a better approximation to the experimental masses, we can repeat the calculation of the total energy deformation function of the nuclear system in the macroscopic-microscopic approach as:

$$E(N, Z, def) = E_{LSD} + \sum_q \left[\delta E_{shell}^{(q)} + \delta E_{pair}^{(q)} \right] \ , \tag{10.6}$$

with the shell and pairing corrections $\delta E_{shell}^{(q)}$ and $\delta E_{pair}^{(q)}$ ($q = n, p$) being given by Eqs. (7.8) and (7.7), respectively.

With this above Eq. 10.4, we can calculate the nuclear energy as a function of the deformation using the parameters introduced in chapter 3: η, q_2, q_3, q_4 which correspond to the non-axiality, elongation, left-right asymmetry and neck shape of the nuclear surface, respectively. It is possible to generate a potential energy surface of the nucleus, forming a 4D equidistant grid, with an appropriate number of points corresponding in each of the mentioned coordinates. We have used a step length of $\Delta q_2 = 0.05$ for the elongation parameter q_2 and for the other three parameters of deformation a step length of $\Delta q_j = 0.03$, so, the total mesh size has $n_2 \times n_3 \times n_4 \times n_\eta = 60 \times 15 \times 15 \times 15 = 2.022.500$ nodes.

With this grid, it is possible to achieve a correct description with a good approximation of all physically important quantities, like the local minima, ground-state minimum, saddle points, and the formation of valleys and ridges leading to different modes of fission.

11 Recalculating potential energy surfaces to find the barrier heights

In this chapter, we compare the potential energy two-dimensional maps obtained with the new pairing-strength fit with those presented in section 9. In section 9, we displayed the PES for the heavy elements up to Rf while in the present study, we have extended the range of isotopes up to the Ubn nuclei. We have chosen here an isotope with A number approximately centered among all the isotopes of that chain.

Due to the large number of maps on potential energy surfaces, we have decided to attach a link from which all these maps can be accessed on the internet: https://tpd.umcs.pl/index.php/s/RAEtp2zkZbXMEZa.

Although in this recalculation of the energy values with newly fitted pairing strength G, more isotopes of the super heavy elements have been added to the study, we have chosen the same isotopes from among the actinides shown in chapter 9 to allow for easier comparison.

For various reasons, we have not used the same colour range in the maps of Chapter 9 and the current one. Instead, the values describing the energy isolines tell us the value of the energy in each region of the map, which can be used to compare the PESs with the old and new pairing force intensities.

In the first isotope shown, ^{226}Th, comparing both graphs of Chapter 9 and the current one, we can see that they have broadly the same pattern, with only minor differences. For example, in both cases, they show essentially 3 minima in approximately the same locations and with very similar energies.

We can highlight small differences in the maps but with very little impact on the fission process. For example, in the panel (q_2, q_4), we can notice that the fission valley with the old pairing is formed a little earlier, even a small minimum appears before this valley at about $q_2 = 1.5$, while in the equivalent new pairing, the fission valley appears slightly later without seeing this advanced minimum. There are some other small differences, but they have practically no influence on the fission process.

In the next example, ^{234}U, similar regularities are seen. Broadly speaking, the configurations corresponding to the new and old pairing strengths appear similar. In both cases, two minima are visible at approximately $q_2 = 0.4$ and $q_2 = 0.8$. Slight energy differences do show up in the compared minima, but these differences do not exceed 1MeV.

Similarly, we can review the different actinide elements by comparing the graphs between the new and the old pairing corrections. We can see that in all these cases, the surface shapes and corresponding energies are, in general, very similar.

We can therefore affirm that this modification in the paring correction does not introduce a drastic change in the physics of the fission reaction, but when comparing the energy barriers from both models with the experimental data (54), an overall improvement can be seen in favour of new estimates of pairing intensities.

As we can see in the following figure 11.1 where the barrier heights in the actinide elements are represented, using both approaches, one with the old pairing correction and the new one that has been explained in this manuscript.

In the potential energy surfaces for super-heavy nuclei, we can already observe at first glance features that are different from those typical of actinides. For example, the energy values of important stationary points, as e.g. minima of the ground state and the isomeric ones, saddle points are more pronounced than in the case of actinides, with clearly lower minima values and higher saddle point values given in this work always in relation to the energy of the liquid drop (LSD) at a spherical point, which is set as a type of reference configuration. Also, it seems remarkable that the energies of the fission valley bottom along the fission trajectories are usually lower than in the actinides.

Such extremely varying energy values from one nucleus to another have made it difficult to choose a suitable range for the colour palette to represent the PES maps. This is the main reason that there can be an excess of purple areas for very low energy values or an excess of white ones for very high energies.

Only in the element flerovium, with Z=114, does the stable shape of the nucleus begin to have a near spherical form with the elongation coordinate taking a value close to $q_2 = 0$, maintaining this sphericity in the other elements with higher atomic numbers. This undoubtedly means that the shell and pairing corrections in these nuclei changes weakly
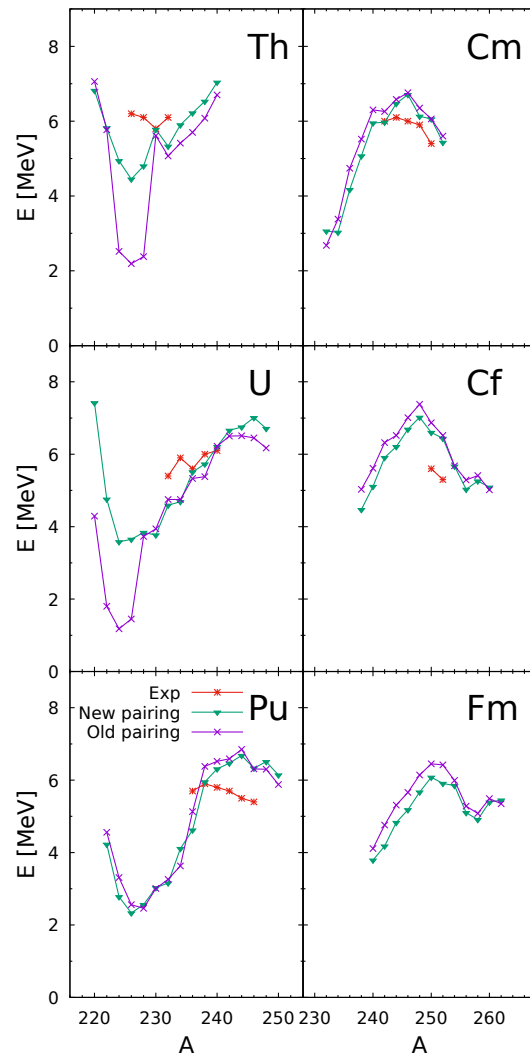
Figure 11.1: Barrier heights calculated with the new (green colour)and old pairing (purple colour). Experimental data (red colour) (55).

Figure 11.2: Potential energy surfaces for ^{226}Th.
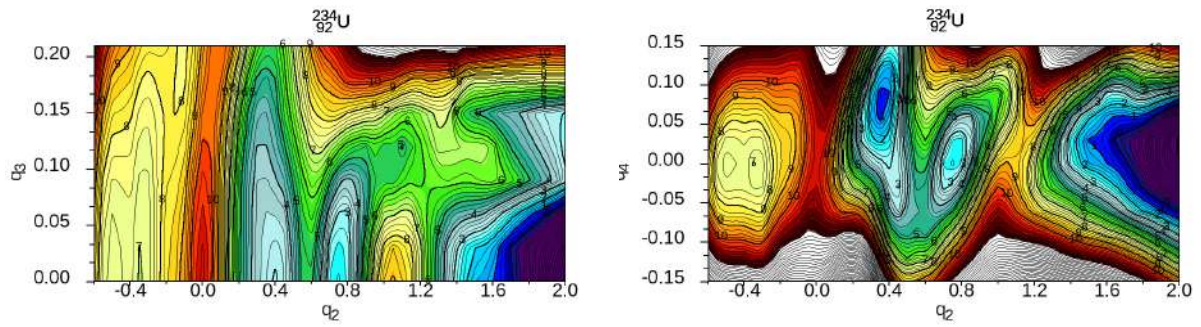
Figure 11.3: Potential energy surfaces for ^{234}U.
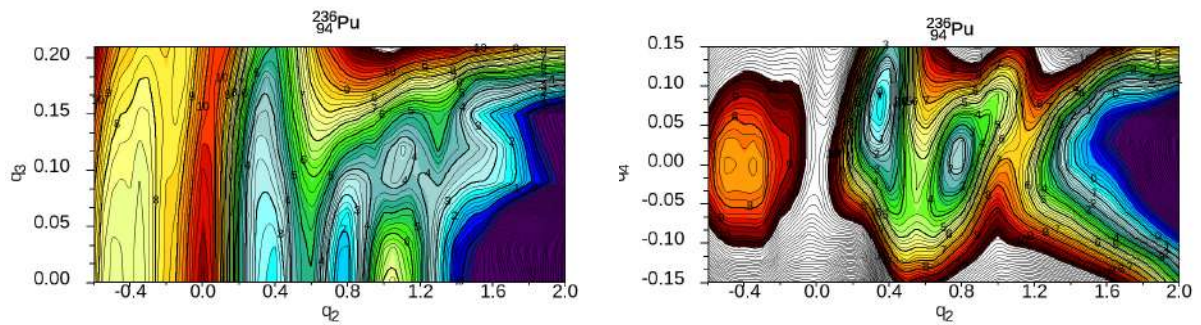
Figure 11.4: Potential energy surfaces for ^{236}Pu.
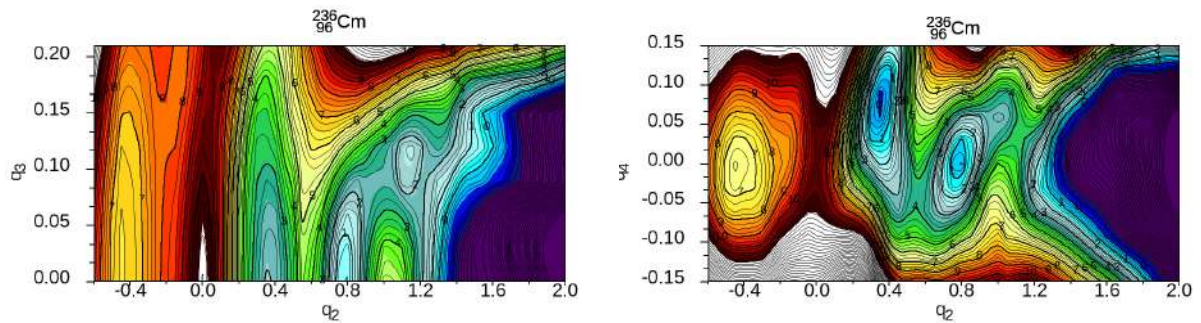
Figure 11.5: Potential energy surfaces for ^{236}Cm.
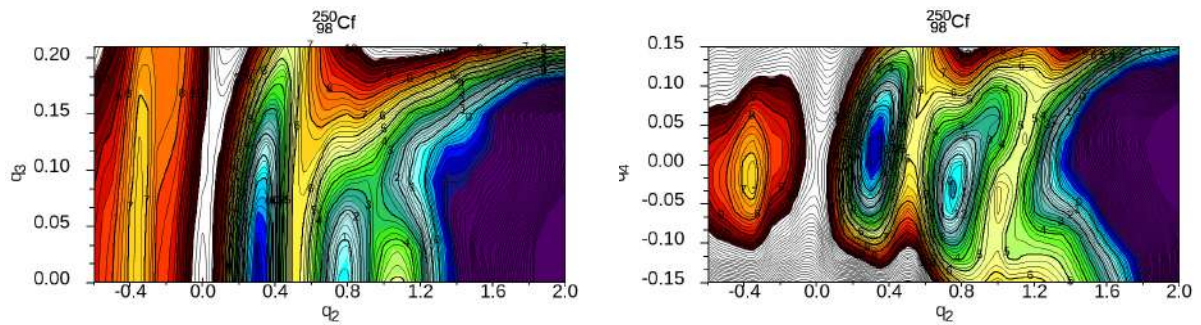
Figure 11.6: Potential energy surfaces for ^{250}Cf.
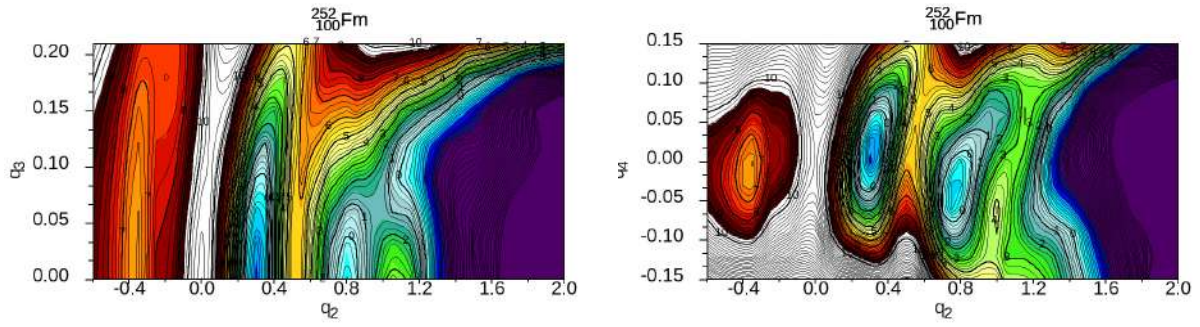
Figure 11.7: Potential energy surfaces for ^{252}Fm.
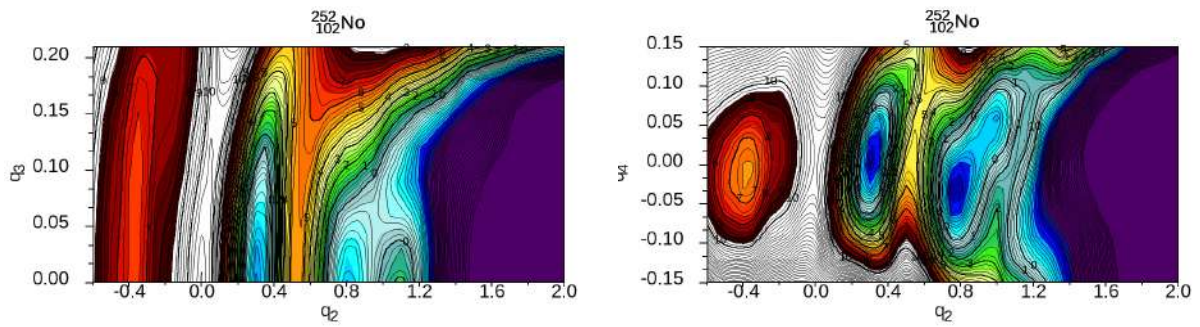
Figure 11.8: Potential energy surfaces for ^{252}No.
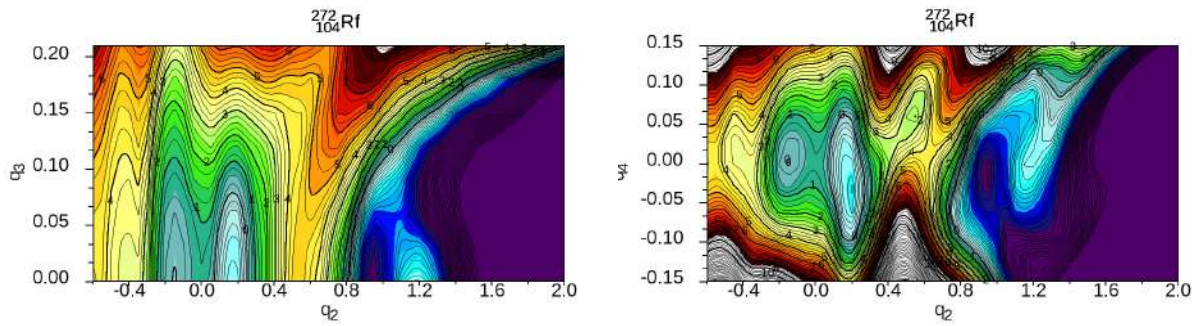
Figure 11.9: Potential energy surfaces for ^{272}Rf.
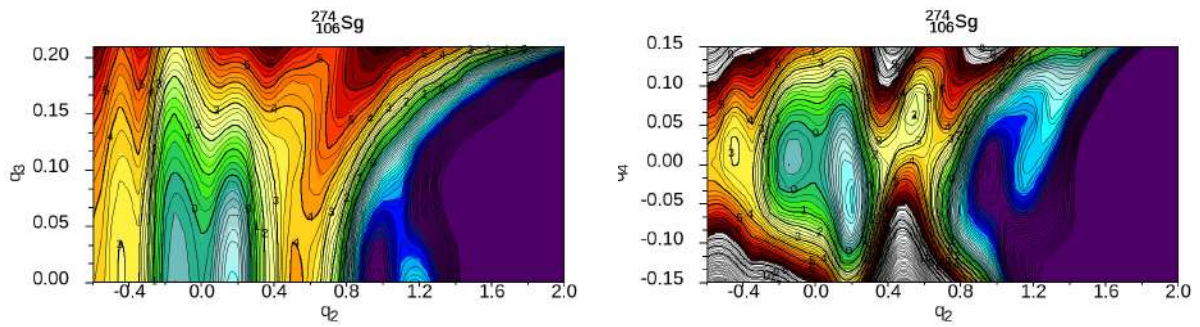
Figure 11.10: Potential energy surfaces for ^{274}Sg.
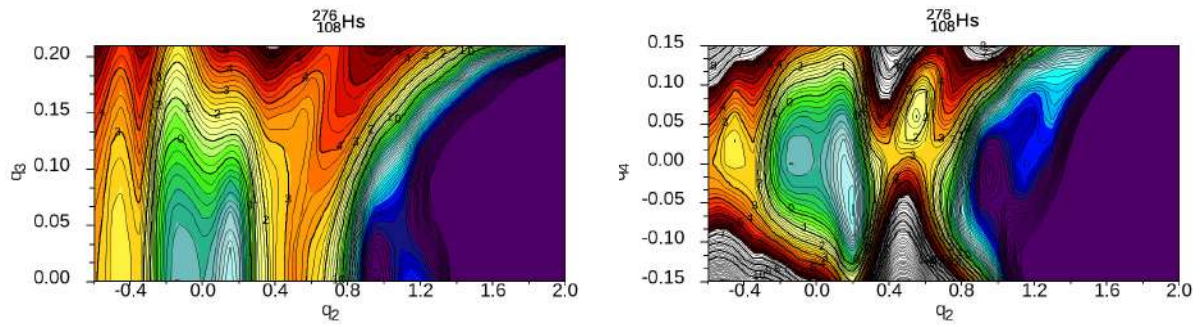
Figure 11.11: Potential energy surfaces for ^{276}Hs.
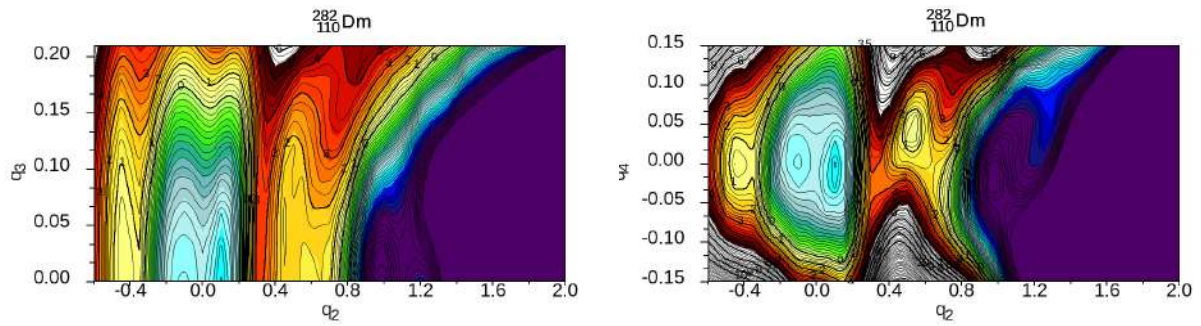
Figure 11.12: Potential energy surfaces for ^{282}Dm.
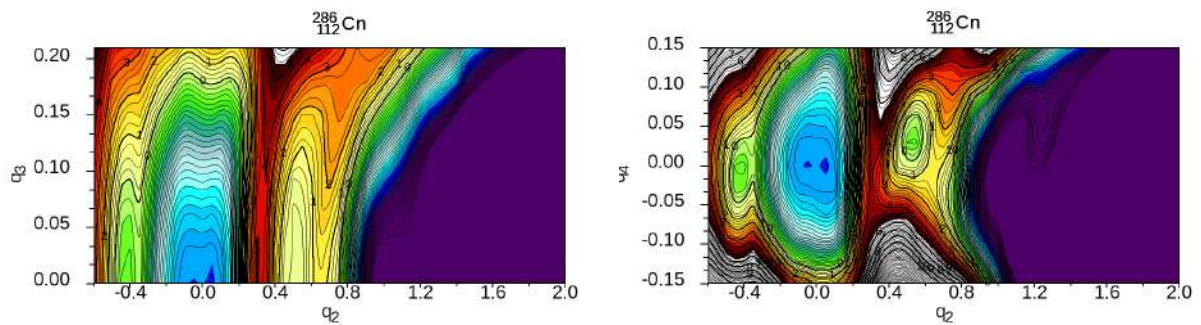
Figure 11.13: Potential energy surfaces for ^{286}Cn.
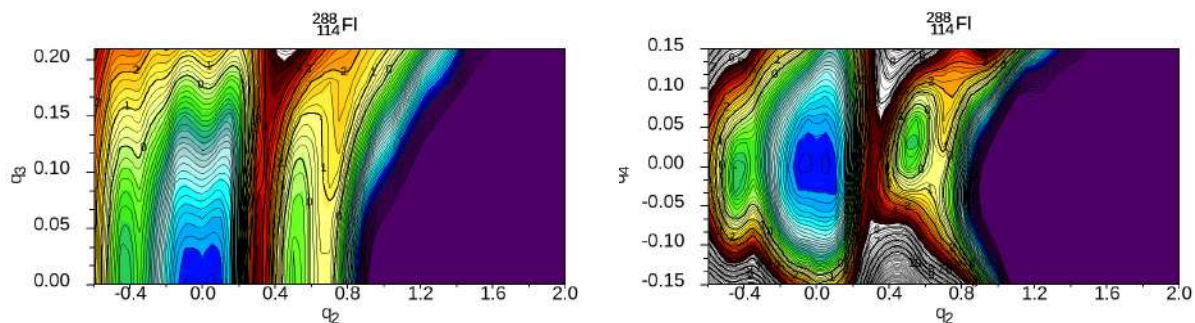
Figure 11.14: Potential energy surfaces for ^{288}Fl.
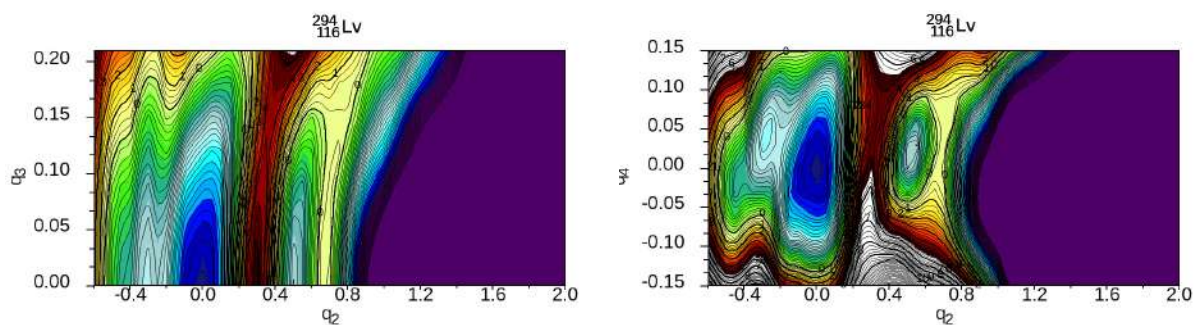
Figure 11.15: Potential energy surfaces for ^{294}Lv.
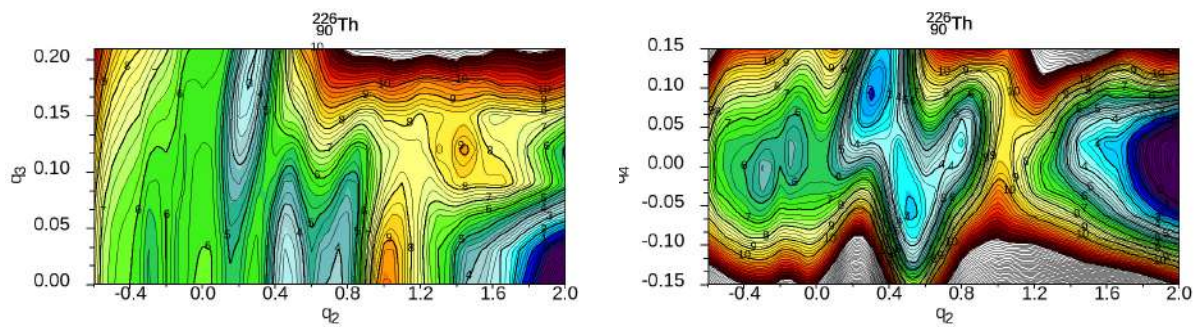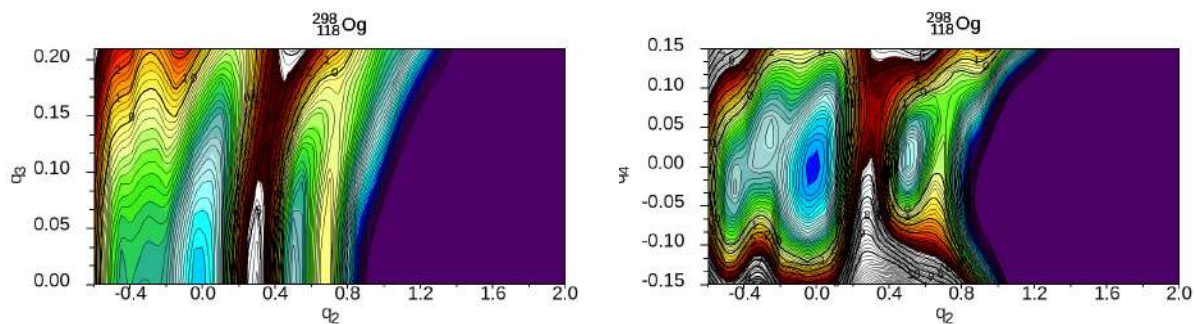

Figure 11.16: Potential energy surfaces for ^{298}Og.

with deformation, being unable to modify significantly the deformation dependence of the total energy imposed by the liquid drop term alone.

Taking into account that the energy reference is in the spherical configuration, in the nuclei of superheavy elements, the energies of GS are on average lower than those of actinide nuclei. This leads to higher barrier heights on average in the superheavy elements.
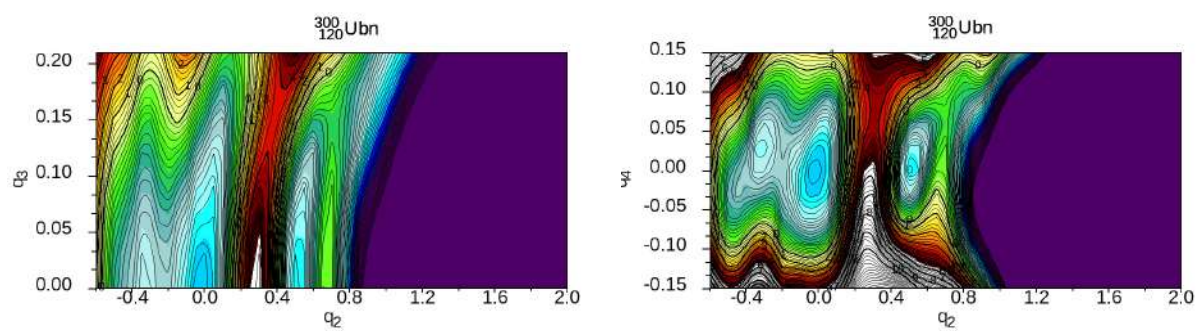
Figure 11.17: Potential energy surfaces for ^{300}Ubn.

12 Study of the GS, saddle points and barriers in odd nuclei

So far all our work has been confined to the study of nuclei with an even number of particles, both in protons and neutrons. As we have seen in Chapter 8 for actinides, only an in-depth study of even-even actinides is performed. Now we shall extend our study to all actinide nuclei, including those with odd numbers of protons and/or neutrons. In addition, these calculations already implement the improved pairing strength G derived in Chapter 6. The element that distinguishes systems with an even number of protons and neutrons from systems where one of these numbers is odd is the treatment of the unpaired particle in the super-fluid BCS model producing the pairing correction. Within the framework of this work, we use the seemingly simplest solution so that the odd particle has the lowest quasi-particle energy of all those residing in the pairing window around Fermi surface. An extra term corresponding to the average energy required to destroy a nucleon pair in a nucleus with an odd particle is also taken into account in the LSD leading energy term.

We will now put some selected cases of the PES maps that we will be commenting on. We will also expose the energy fission barriers. On this occasion, where it has been extended to odd nuclei. We have chosen cases where the most common configurations can be seen, but also some configurations with more peculiar characteristics.

As before, due to the large number of maps on Potential Energy Surfaces (PES), we have decided to attach a link from which all these maps can be accessed on the internet: https://tpd.umcs.pl/index.php/s/RAEtp2zkZbXMEZa.

With the first odd element in our work, actinium, we can observe from the lightest isotope in the study, ^{220}Ac to ^{232}Ac an important characteristic, which is that the GS has an asymmetric configuration. As examples of isotopes with this asymmetric GS configuration, we present ^{223}Ac and ^{232}Ac, the latter being the heaviest isotope in the study that shows this characteristic. In this chain with an asymmetric GS, its $_q3$ coordinate remains in the region $q_3 = 0.15$ and $q_3 = 0.2$. This asymmetric GS is located in the region around $q_2 \approx 0.2$. From the ^{233}Ac isotope onwards, the symmetry changes drastically and the GS

always presents a symmetric configuration in all Ac isotopes.

With the protactinium element, we observe a very similar behaviour, since from the lightest isotope included in this work, ^{220}Pa to ^{235}Pa, the GS is symmetric, and from ^{236}Pa onwards the GS changes to a symmetric configuration. As an example of Pa with asymmetric GS we show ^{221}Pa and ^{230}Pa, and as an example of symmetric GS we show ^{239}Pa. The ^{230}Pa is also an interesting example as it has 3 minima, a feature that is present in the isotopes from ^{227}Pa to ^{234}Pa.

In the case of neptunium isotopes, we can also observe a drastic change between the lighter and heavier isotopes. In the ^{224}Np one, we can see that the GS is asymmetric while the second symmetric minimum is washed out. Since the equilibrium state is q_3 deformed the first saddle configuration has the same property. On the contrary, in ^{237}Np isotope, the GS and well pronounced second minimum are mass-symmetric. Studying only the PES in the vicinity of the scission configurations, i.e. for $q_2 > 1.4$ of both neptunium isotopes one can deduce that the most like fission channels are asymmetric.

(a) ^{223}Ac $\mathrm{E}_{pot}(q_2, q_3)$ **(b)** ^{223}Ac $\mathrm{E}_{pot}(q_2, q_4)$
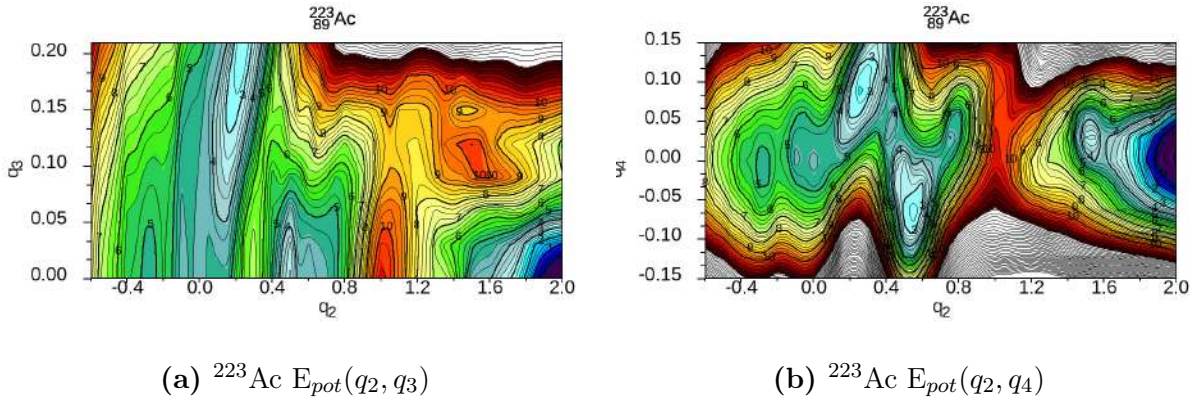
Figure 12.1: Potential energy surfaces for ^{223}Ac.

(a) ^{232}Ac $\mathrm{E}_{pot}(q_2, q_3)$ **(b)** ^{232}Ac $\mathrm{E}_{pot}(q_2, q_4)$
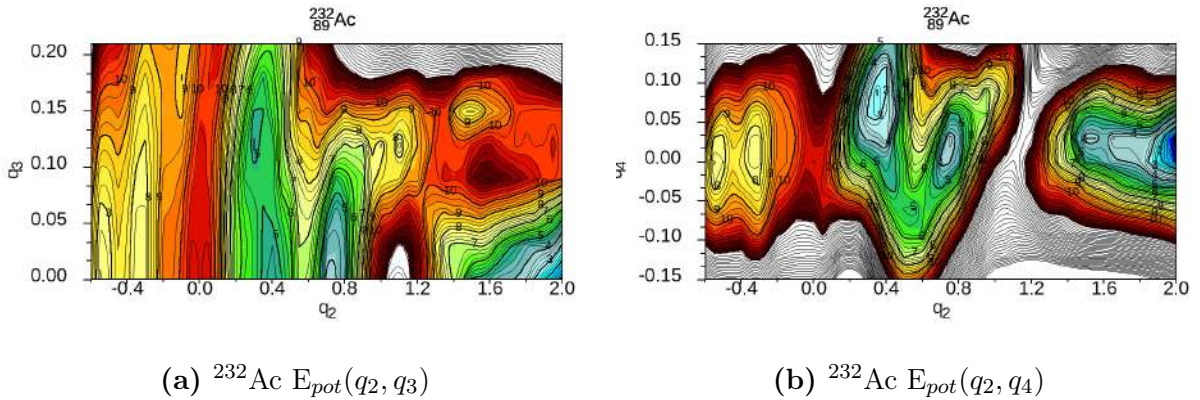
Figure 12.2: Potential energy surfaces for ^{232}Ac.
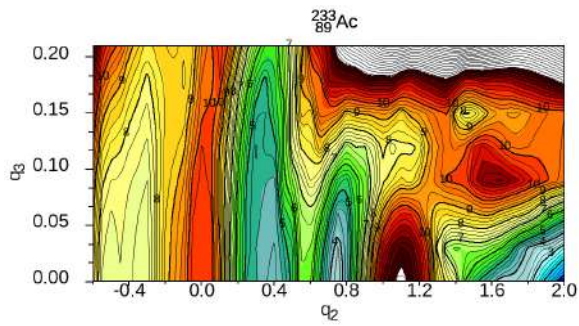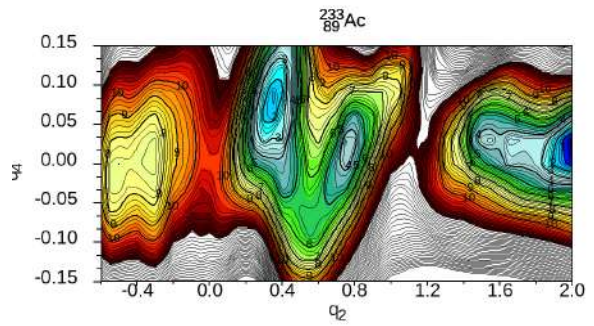
(a) ^{233}Ac E$_{pot}(q_2, q_3)$ **(b)** ^{233}Ac E$_{pot}(q_2, q_4)$

Figure 12.3: Potential energy surfaces for ^{233}Ac.
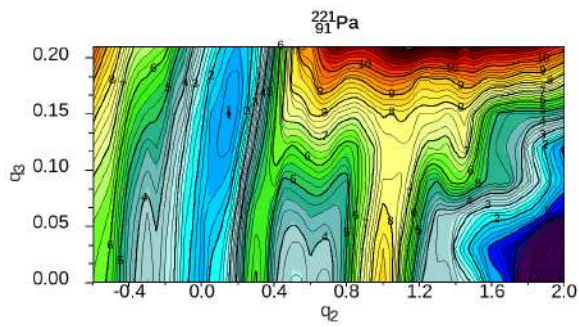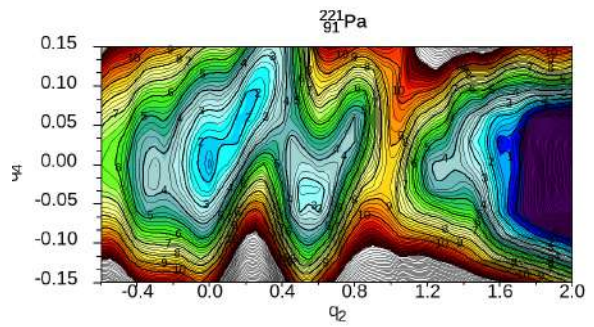
(a) ^{221}Pa E$_{pot}(q_2, q_3)$ **(b)** ^{221}Pa E$_{pot}(q_2, q_4)$

Figure 12.4: Potential energy surfaces for ^{252}Pa.
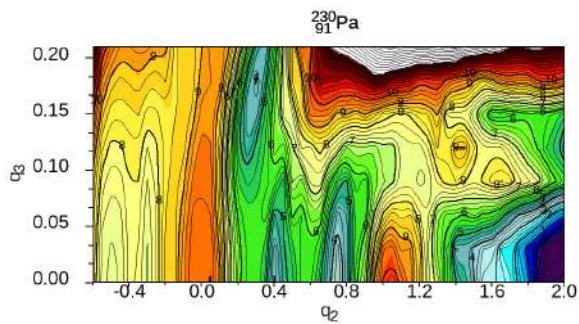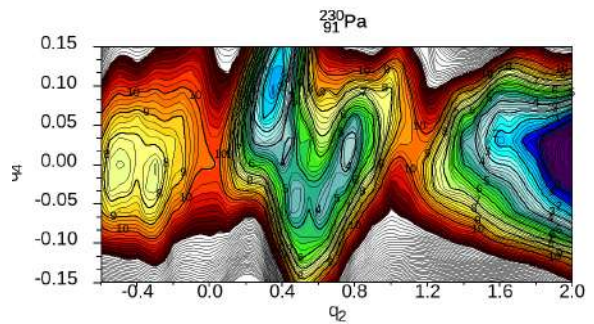
(a) ^{230}Pa E$_{pot}(q_2, q_3)$ **(b)** ^{230}Pa E$_{pot}(q_2, q_4)$

Figure 12.5: Potential energy surfaces for ^{230}Pa.
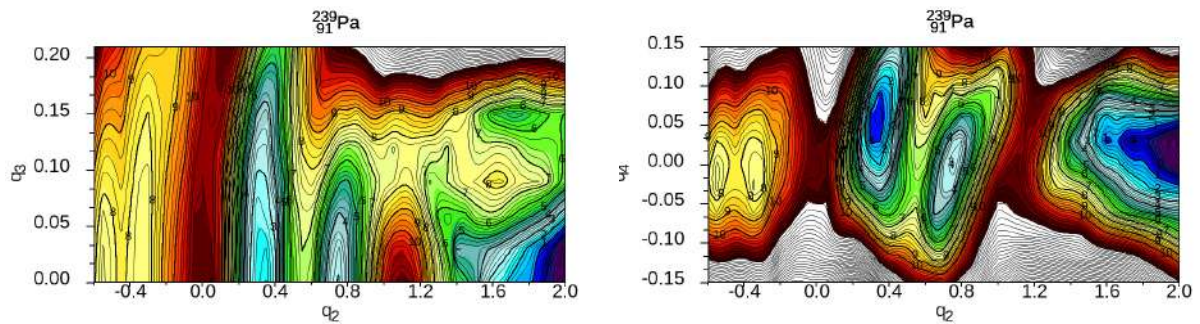
(a) ^{239}Pa E$_{pot}(q_2, q_3)$ **(b)** ^{239}Pa E$_{pot}(q_2, q_4)$

Figure 12.6: Potential energy surfaces for ^{252}Pa.
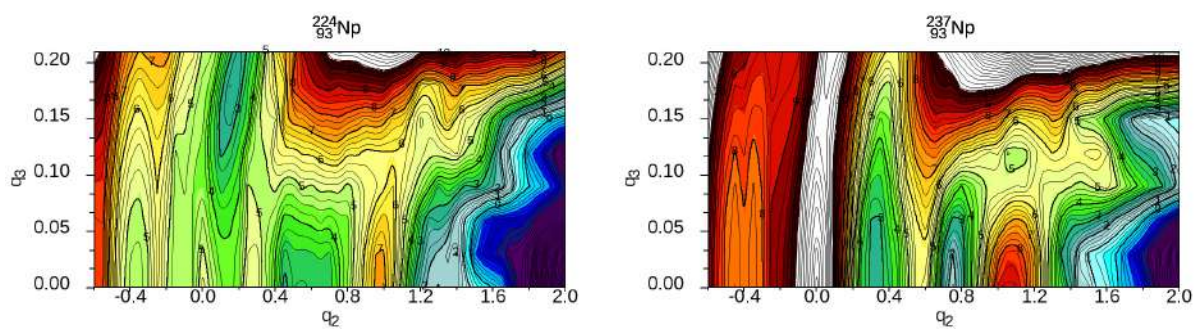
(a) ^{224}Np E$_{pot}(q_2, q_3)$ **(b)** ^{237}Np E$_{pot}(q_2, q_3)$

Figure 12.7: Potential energy surfaces for ^{224}Np and ^{237}Np.

(a) ^{227}Pu E$_{pot}(q_2, q_3)$ **(b)** ^{227}Pu E$_{pot}(q_2, q_4)$
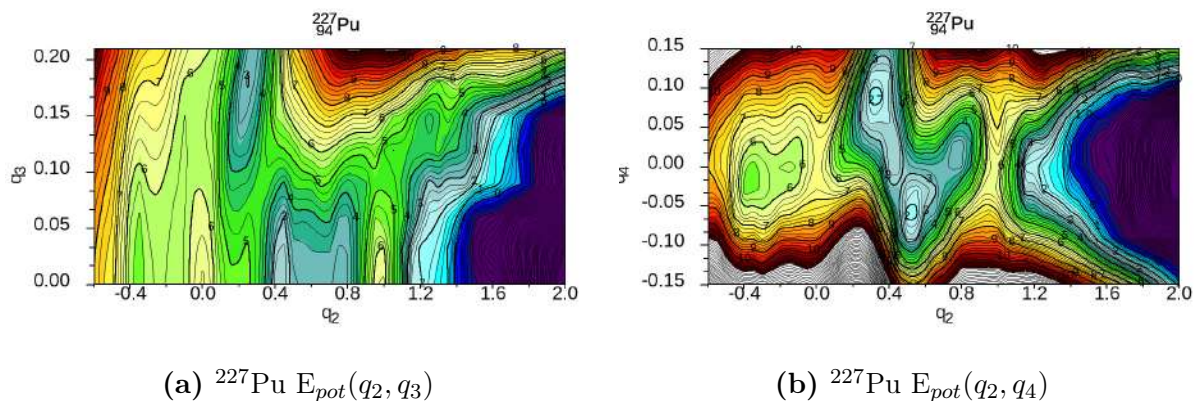
Figure 12.8: Potential energy surfaces for ^{227}Pu.

(a) ^{233}Pu E$_{pot}(q_2, q_3)$ **(b)** ^{233}Pu E$_{pot}(q_2, q_4)$
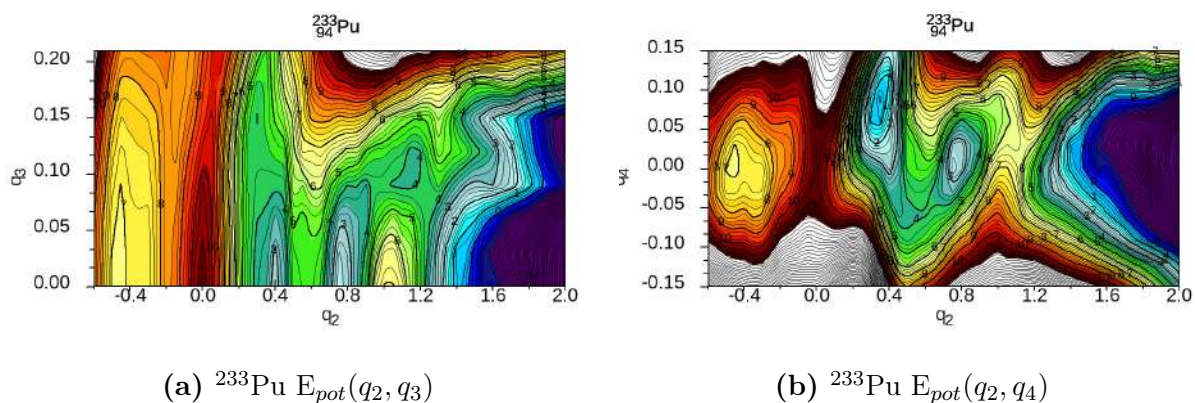
Figure 12.9: Potential energy surfaces for ^{233}Pu.

Similar properties to the above seen in Np nuclei can be given for the two odd plutonium isotopes, ^{227}Pu and ^{233}Pu. but with the exception that in addition, symmetric fission modes are also expected. This is facilitated by the fact that the symmetric energy maxima in Pu at $q_2 \approx 1$ which may efficiently block the symmetric fission path, are significantly lower and less extensive than in neptunium.

Different behaviour of the GS minima is observed in Americium as the isotope mass increases. In the lighter isotope ^{225}Am, we observe the substantially mass-asymmetric GS at $q_2 = 0.1$ and quite extensive energy well with two degenerated minima corresponding to the isomeric configuration. When we move to ^{231}Am, we see that its GS minimum is now symmetric and shifted towards larger elongations being around $q_2 \approx 0.4$. If we keep increasing the A number, in ^{235}Am, we can see that a relatively shallow third asymmetric minimum is formed at about $q_2 = 1.1$. At the same time, the symmetric maximum forming at $q_2 \approx 1$ and jamming the symmetric fission channel is getting higher and higher with increasing mass number.

84

(a) ^{225}Am E$_{pot}(q_2, q_3)$

(b) ^{225}Am E$_{pot}(q_2, q_4)$
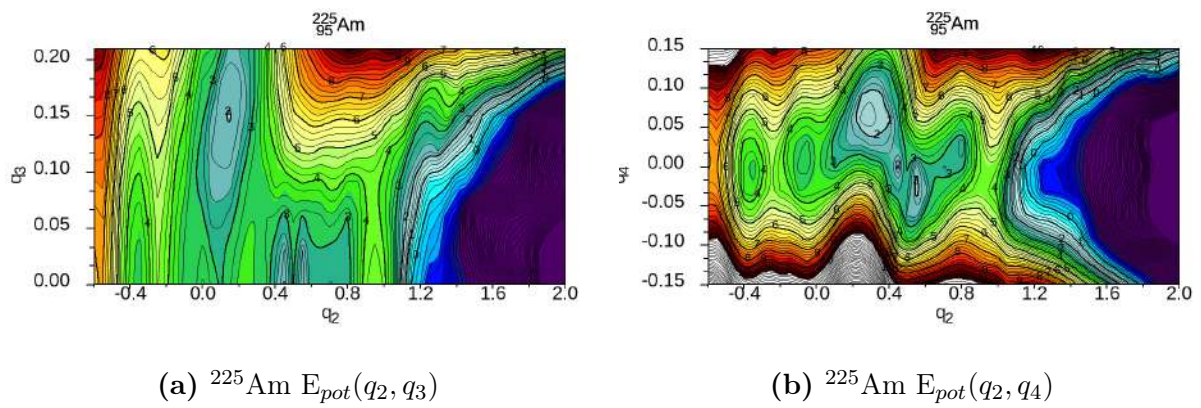
Figure 12.10: Potential energy surfaces for ^{252}Pa.

(a) ^{231}Am E$_{pot}(q_2, q_3)$

(b) ^{231}Am E$_{pot}(q_2, q_4)$
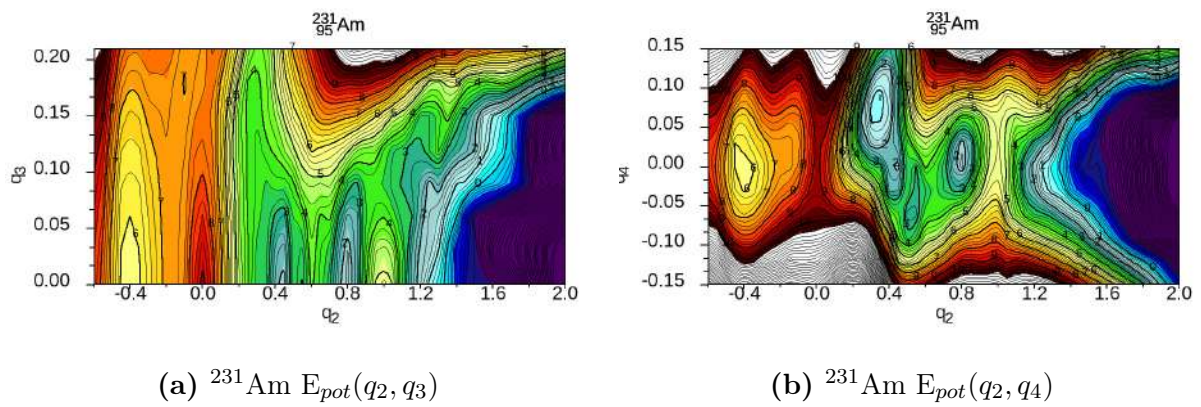
Figure 12.11: Potential energy surfaces for ^{231}Am.

(a) ^{235}Am E$_{pot}(q_2, q_3)$

(b) ^{235}Am E$_{pot}(q_2, q_4)$
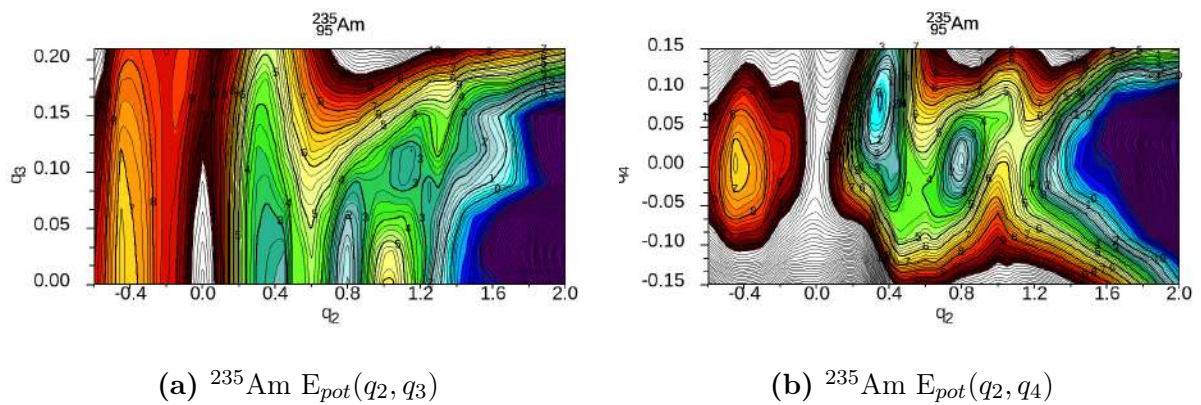
Figure 12.12: Potential energy surfaces for ^{252}Am.

(a) ^{225}Cm $E_{pot}(q_2, q_3)$ **(b)** ^{225}Cm $E_{pot}(q_2, q_4)$
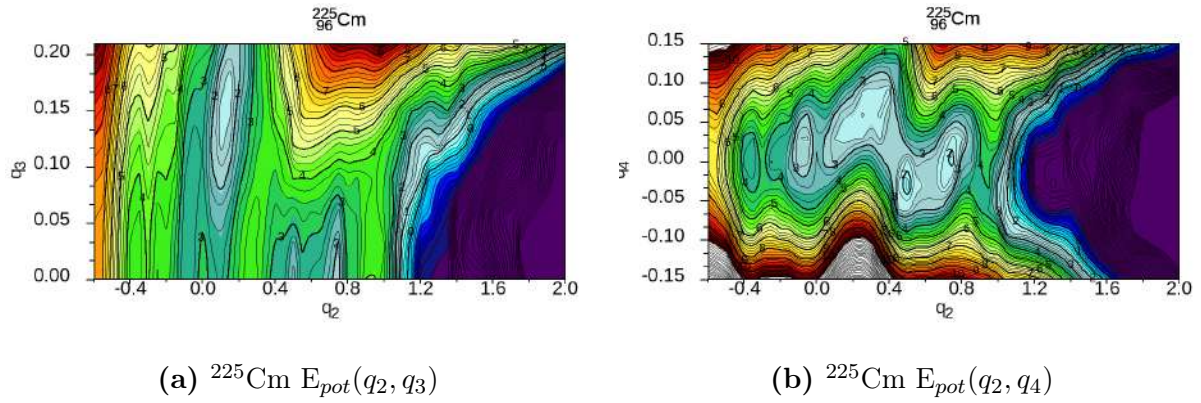
Figure 12.13: Potential energy surfaces for ^{225}Cm.

(a) ^{240}Cm $E_{pot}(q_2, q_3)$ **(b)** ^{240}Cm $E_{pot}(q_2, q_4)$
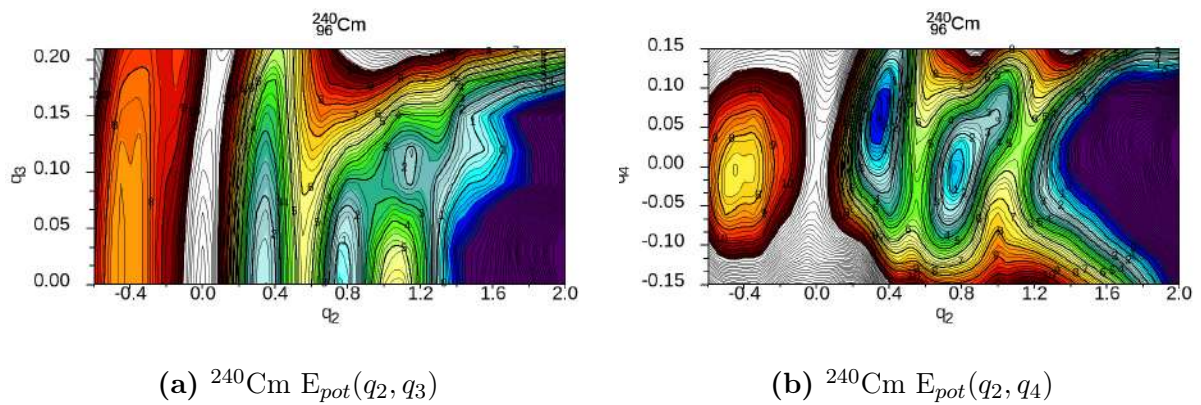
Figure 12.14: Potential energy surfaces for ^{240}Cm.

**(a)** ^{246}Cm $E_{pot}(q_2, q_3)$ **(b)** ^{246}Cm $E_{pot}(q_2, q_4)$
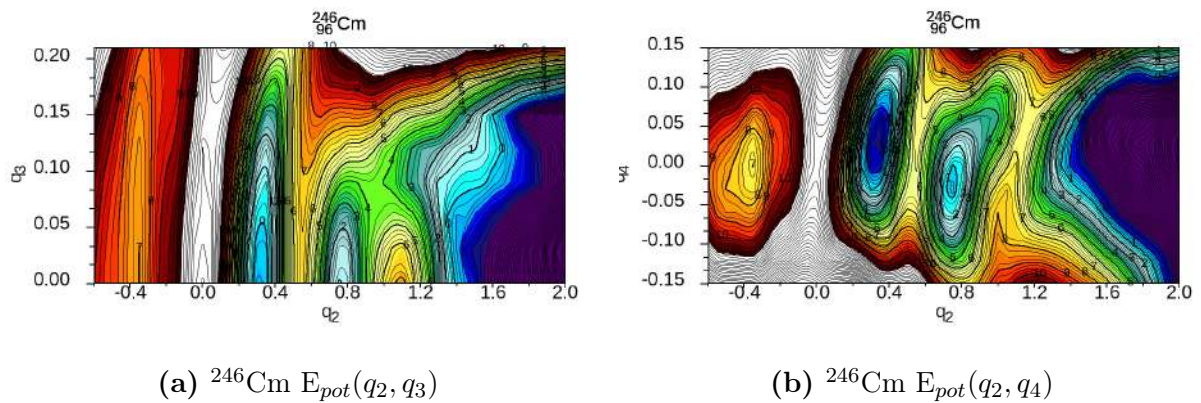
Figure 12.15: Potential energy surfaces for ^{246}Cm.

Also, in the case of curium, in the light region, we observe at ^{225}Cm an asymmetric GS and three minima, from the second minimum onwards, the whole path towards fission is symmetric. At ^{240}Cm and in heavier isotopes, two minima are observed, where the GS is mass-symmetric, in the region of the second saddle the configuration changes to asymmetric to return again into a symmetric state at the end of the fission path.

(a) ^{238}Bk E$_{pot}(q_2, q_3)$ **(b)** ^{238}Bk E$_{pot}(q_2, q_4)$
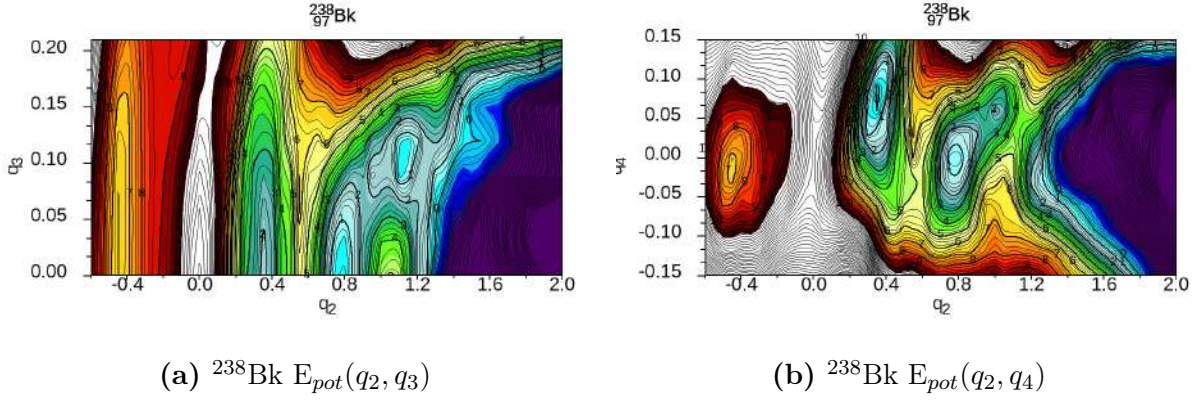
Figure 12.16: Potential energy surfaces for ^{238}Bk.

(a) ^{249}Bk E$_{pot}(q_2, q_3)$ **(b)** ^{249}Bk E$_{pot}(q_2, q_4)$
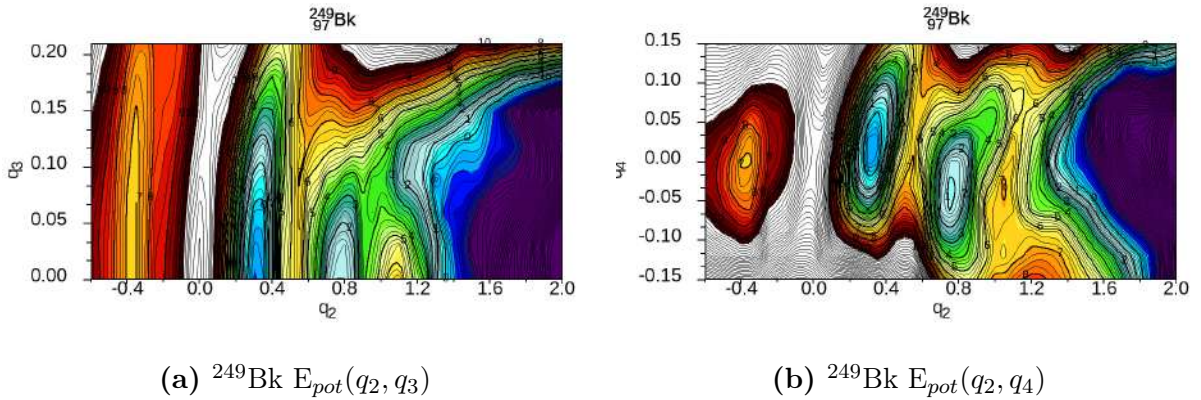
Figure 12.17: Potential energy surfaces for ^{249}Bk.

With the element berkelium, the GS always maintains a symmetric configuration, although in the light isotope ^{238}Bk it shows a configuration with main 3 minima when the third asymmetric one occurs at $q_2 = 1.15$. In ^{249}Bk the third minimum disappears. The scission area covers a very wide range of symmetric and asymmetric fragmentation modes while in heavier isotopes the energy maximum on the way along the symmetric path is higher than this in the ^{238}Bk isotope.

In californium, we observe a general behavior very similar to that of berkelium. In the light isotope, ^{239}Cf, three minima are observed while in the heavy even-even ^{252}Cf one - only two minima are observed. In both cases, the fission path is firstly symmetric until reaching the second saddle point, where it changes to an asymmetric one till the end of the fission.

In the last figure of this chapter, we show the fission barrier heights of the studied isotopes, where the solid red dots represent the experimental values taken from (54) while the blue dots represent the theoretical estimates. Analyzing the PESs shown in the above maps
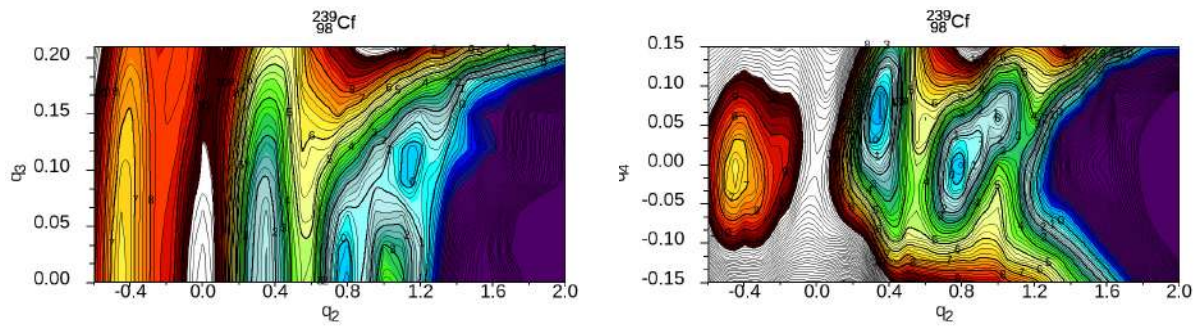
(a) ^{239}Cf E$_{pot}(q_2, q_3)$ **(b)** ^{239}Cf E$_{pot}(q_2, q_4)$

Figure 12.18: Potential energy surfaces for ^{239}Cf.
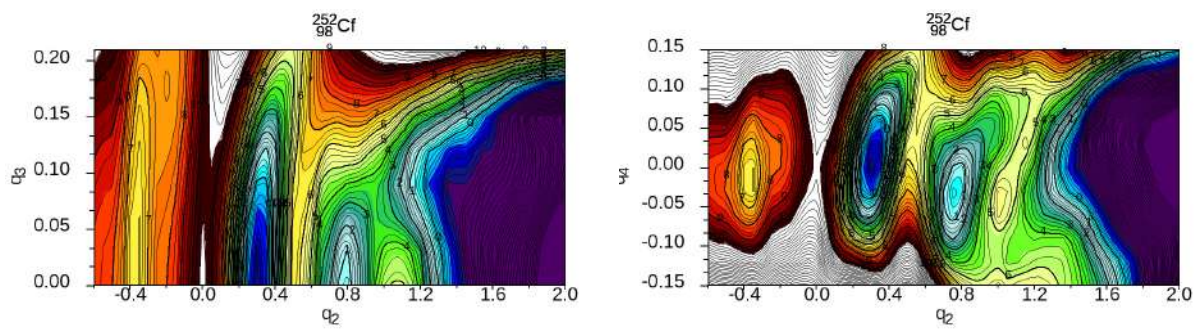
(a) ^{252}Cf E$_{pot}(q_2, q_3)$ **(b)** ^{252}Cf E$_{pot}(q_2, q_4)$

Figure 12.19: Potential energy surfaces for ^{252}Cf.

we have evaluated the fission barrier heights for all considered nuclei. The numerical data with the results are listed in the tables presented in Appendix A and B. The theoretical fission barrier heights (open points) are compared with the available experimental data (full points) in Fig. 12.20 for all even and odd isotopes from Ac to Cf. The values shown correspond to the highest of the inner or outer barrier, calculated as the difference between the energy of the saddle point with the highest energy and the ground state.

The characteristics of the fission barrier heights shown in Fig. 12.20 for actinide and super-heavy nuclei clearly indicate that the macroscopic-microscopic model used in all presented here studies is able to replicate the experimental barrier heights and fission half-lives of even-even nuclei with good accordance. The method of calculating the spontaneous fission
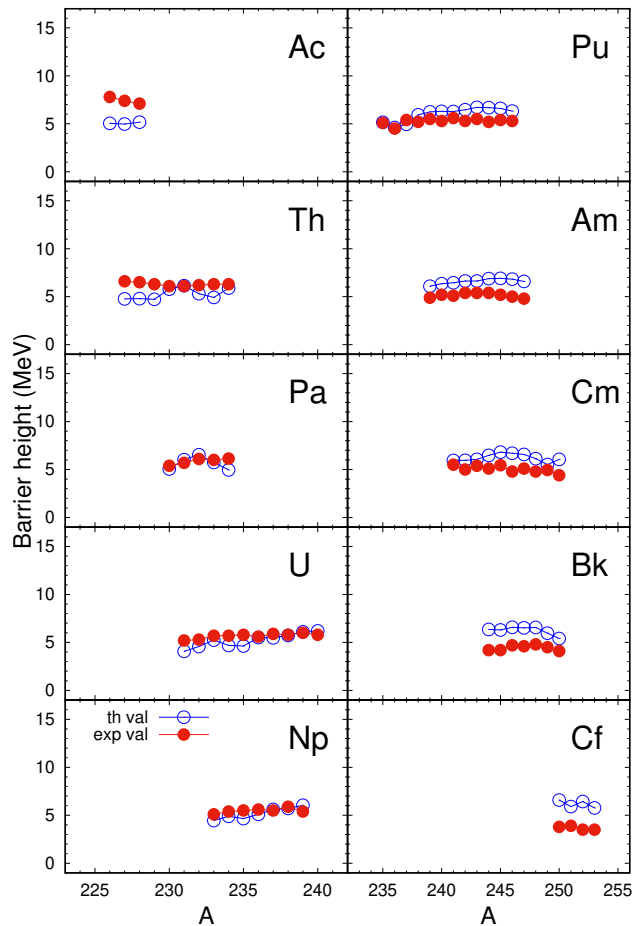
Figure 12.20: Barrier heights of even-odd and odd-odd actinide nuclei.

half lives and the appropriate results will be addressed in great detail in the forthcoming section. Although the fission lifetimes for even-odd and odd-odd nuclei are not discussed in this work but a high quality of reproducing the empirical barrier heights in these 10 isotopic chains from Ac to Bk, seen in this figure, may lead to the belief that they will also be estimated with a reasonable accuracy.

Let us remind that, in odd-even and odd-odd nuclei the unpaired particle is represented in the BCS approach by the lowest in energy quasi-particle from the "pairing window" located around the Fermi level. At the same time, it seems doubtful that during the whole path to fission described in multidimensional deformation space containing a non-axiality, it is possible to assume the constancy of any quantum number of the state corresponding to an odd particle.

13 Calculations of spontaneous fission half-lives of actinide and super-heavy nuclei

With the data obtained in the previous sections, it is possible to calculate the spontaneous fission half-lives of actinide and super-heavy nuclei, but first, let us introduce the theoretical framework used for this calculation.

13.1 Multidimensional WKB method

One of the most successful semi-classical approximations to obtain an approximate solution of the Schrödinder equation is the WKB method, which takes into account the potential energy barrier that the particle under study has to penetrate. In this method, we presume that the wave function of the particle moving in this potential can be represented as a plane wave with momentum $k(x)$ which is a function of the position x and varies slowly with this coordinate.

In our method, we use a multidimensional form of the above mentioned WKB approximation to evaluate the half life of a nucleus undergoing spontaneous fission. This method has been extensively implemented in nuclear physics to obtain the penetrability of a potential-energy barrier established in a multidimensional deformation space, for fission or cluster emission processes. In the following, we outline the generalization of the standard one-dimensional WKB method to a four-dimensional deformation space. The Fourier parameters q_i introduced in Eq. (3.28) serve here as the deformation variables.

The initial step in obtaining a reliable estimate for the half lives of a system undergoing spontaneous fission is to find the *least-action path* (LAP) that leads to fission within the 4-dimensional PES which a nucleus needs to follow to split into fission fragments. Such an approach considers a fission event as a dynamic process, characterized by the collective motion of numerous nucleons that tend to elongate the nuclear shape from an initial state, such as the nuclear ground state towards the scission configuration. It is important to mention that the collective space in which the fission process is simulated can often be multidimensional, curvilinear, and non-Euclidean.

In our current approach, the path to fission occurs within a four-dimensional space,

specifically defined by the Fourier deformation parameters $(q_1 \equiv \eta, q_2, q_3, q_4)$ as outlined in Eqs. (3.26)-(3.29). Our investigation has shown that considering tri-axiality q_1 leads to a slight decrease (within 1 MeV) in the heights of the inner fission barrier along the least-energy path.

One should note that the energy $E(q_1, q_2, q_3, q_4)$ is calculated in the macroscopic-microscopic model, presented in the previous sections in a very detailed way. In this model, the shell corrections in (10.6) are determined using the Strutinsky method. The correction for the residual pairing interaction is obtained in the BCS approximation with projection onto good particle number, as outlined in the GCM approach (see, Ref. (45)). In both of these approaches, single-particle states of the mean-field folded-Yukawa potential (46) are utilized.

13.2 Least-action fission path

The action in the 4-dimensional deformation space $\{q_1, q_2, q_3, q_4\}$ introduced above can be represented by the following integral:

$$
S = \int_{q_2^{(g.s.)}}^{q_2^{(exit)}} dq_2 \sqrt{\frac{2}{\hbar^2} \sum_{ij=2}^{4} \beta B_{ij}(q_k)\left[\mathcal{E} - E(g.s.)\right]\frac{\partial q_i}{\partial q_2}\frac{\partial q_j}{\partial q_2}}, \tag{13.1}
$$

where $\mathcal{E} = E(\{q_k\})$ and $E(g.s.)$ refer to the potential energy of a given configuration along the fission path and the ground state, respectively. The along the least-action path integration should begin in the nuclear ground-state deformation and extend up to an "exit point" of the same energy as the ground state ($E_{exit} = E_{g.s.}$).

In the 4-dimensional deformation space, there are usually numerous turning (exit) points that satisfy this condition. A real challenge is to identify the specific exit point corresponding to the minimum of the action integral. At first glance, it seems that the action integral provided by equation (13.1) is only calculated along a one-dimensional path L(q_2), parameterized by q_2 only rather than being defined in a multi-dimensional deformation space. However, this is not the case, as under the square root in Eq. 13.1 the explicit expression for the infinitesimal arc length of the least-action curve in a given

curve-linear Fourier collective space is written. A comparable approach has also been utilized in other literature, such as in Refs. (47; 48), to determine the LA integral in a multi-dimensional deformation space.

The deformation-dependent quantity $B_{ij}(\{q_k\})$, whose indices are $i, j = \{1, 2, 3, 4\}$, refers to the pair of the shape parameters (q_i, q_j), is the irrotational flow inertia tensor in the Werner-Wheeler approximation (49). This tensor is represented in the Fig. 13.1 for the diagonal components B_{11}, B_{22} and B_{33} as well as for the off-diagonal component B_{23} projected onto the (q_2, q_1) and (q_2, q_3) planes, respectively. The values of the remaining two deformation parameters q_3, q_4, respectively q_1, q_4 are adjusted in such a way that they minimize the action integral (13.1) along the least-action trajectory.

It should be noted that the deformation-dependent parts of this macroscopic hydrodynamic mass tensor are virtually identical for all nuclei and only need to be multiplied by a scaling factor proportional to $A^{5/3}$, (see, e.g. Ref. (19)) to obtain the right value for each nucleus.
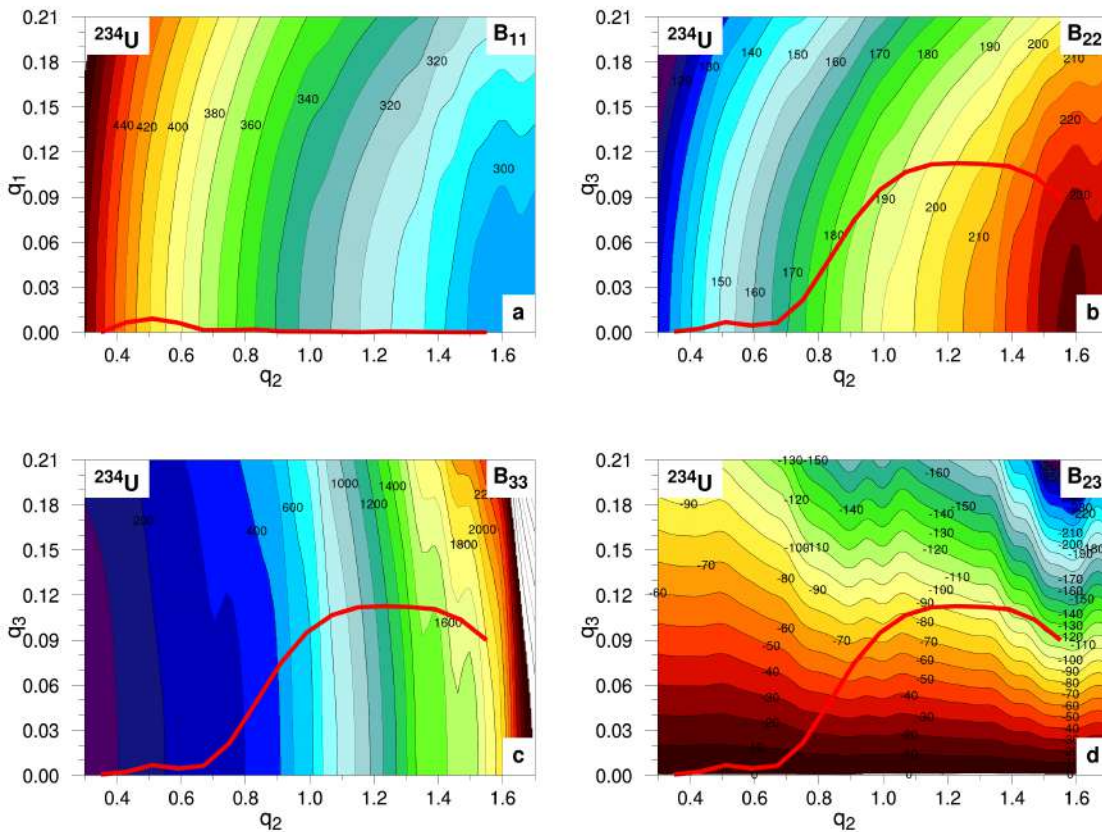
Figure 13.1: Hydrodynamical mass tensor components in the (q_2, q_1) (a) and (q_2, q_3) (b-d) deformation planes. The LAP is indicated by the solid red line.

In Fig. 13.1 we observe that the component B_{22} progressively increases with the elongation q_2, but is only weakly dependent on the mass-asymmetry parameter q_3 in the region where it would have the largest influence on the action integral (13.1), i.e. in the barrier region around $q_2 \approx 1$. Another important component of the inertia tensor, B_{33}, varies slowly with q_2 in this region (below $q_2 \lesssim 1$) but instead, it increases rapidly near the scission line ($q_2 \approx 1.5$). In addition, the component B_{11} decreases with elongation q_2, but remains practically constant when q_1 grows. Since the WKB action integral is affected by an interplay between potential energy and inertia tensor, it can be deduced that it is the potential energy gradient towards q_1 that mostly contributes to the final value of the action and the impact of B_{11} is small in the present case.

Note also that the absolute values of B_{33} are much larger than the ones of B_{22}, thus may contribute significantly to the total action (13.1) when a derivative $\frac{dq_3}{dq_2} \neq 0$, comes into play. This mostly happens if the fission path leads to a mass-asymmetric splitting, even if q_3 stays almost constant in its final part. If, in turn, the turning point is mass symmetric ($q_3 = 0$), the local changes of q_3 variable along the LAP are too weak to substantially contribute to the action integral. Please note also that for the here studied nuclei the fission path usually starts heading towards mass-asymmetric deformations around the second minimum ($q_2 \approx 0.7 - 0.8$) as this is shown for the cases of ^{234}U or ^{252}No in Fig. 13.2. It is interesting to note that changes of the off-diagonal mass component B_{23} shown in Fig. 13.1(d) prefer asymmetric fragmentation.

We use, however, the multiplicative parameter β in front of the B_{ij} mass tensor in (13.1) to re-scale its ten independent components to be able to reproduce within a couple of orders of magnitude the measured actinide half-lives. Clearly, such an operation does not change the relative values between all the tensor components which, in addition to the reliability of the PES, is crucial for a reasonable determination of the LAP course, and consequently, the resulting value of the action. It should be noted that the differences in the inertia values evaluated within available macroscopic or microscopic models can show deviations of up to an order of magnitude. (13).

One of the most important features of the macroscopic hydrodynamical mass tensor used in this work compared to its microscopic (e.g. cranking) counterparts is that the latter is often a rapidly fluctuating function of deformation, mainly due to the microscopic

quantum effects. Such local variations are, to some extent, omitted by the least-action trajectory method itself, where the corresponding LAP tends to bypass states associated with abrupt changes in the potential energy or inertia. This obviously influences the stability of the numerical minimization of the action integral (13.1).

For comparisons, another efficient prescription of the collective inertia effects simulated by the so-called phenomenological mass parameter $B(R_{12})$ is used, which is expressed in units of the reduced mass $\mu = M_{A_L} \cdot M_{A_R}/(M_{A_L} + M_{A_R})$, with M_{A_L} and M_{A_R} being the mass numbers of the left and right fission fragments, respectively (see, e.g. Ref. (49)).

$$B(R_{12}) = 1 + k\frac{17}{15} \exp\left[\lambda\left(R_{12}^{(\text{sph})} - R_{12}\right)\right]. \tag{13.2}$$

The above phenomenological mass parameter is dependent on a single parameter $R_{12} = R_{12}(q_2, q_3, q_4)$ (in units of the radius R_0 of the corresponding spherical nucleus) which describes the evolution of a nucleus towards fission and which describes the centers-of-mass distance. For a spherical shape one has $R_{12}^{(\text{sph})} = 0.75\, R_0$. The parameter $\lambda = 0.408/R_0$ describes the *descent rate* of the exponential function in (13.2).

In this way, unlike the calculations with full hydrodynamical mass tensor, the corresponding 3D total potential energy function $E(q_2, q_3, q_4) = E(q_1^0, q_2, q_3, q_4)$, Eq. (10.6) is used, where q_1^0 is the non-axiality deformation parameter which minimizes the full 4D potential energy $E(q_1, q_2, q_3, q_4)$ at at given point in the 3D (q_2, q_3, q_4) space.

We must keep in mind that the magnitude of the center-of-mass distance R_{12} mainly depends on the elongation q_2 and, to a much lesser extent, on left-right asymmetry and the neck formation parameters, q_3 and q_4. This is why the least-action fission path obtained with the phenomenological mass function of Eq. (13.2) can not be called fully dynamical.

The parameter k in (13.2) is taken in order to ensure that the value of $B(R_{12})$ along the fission barrier (near to $q_2 \approx 1$) is close to the hydrodynamical mass tensor value in that region. Also, it should reproduce the asymptotic behavior, reproduced by the rigid-body inertia, when a nucleus splits into fragments. Then, the inertia of a strongly elongated nucleus, close to the scission configuration, has to smoothly merge into the reduced mass of the two fragments. It was found that the optimal value of this parameter is $k = 11.5$.
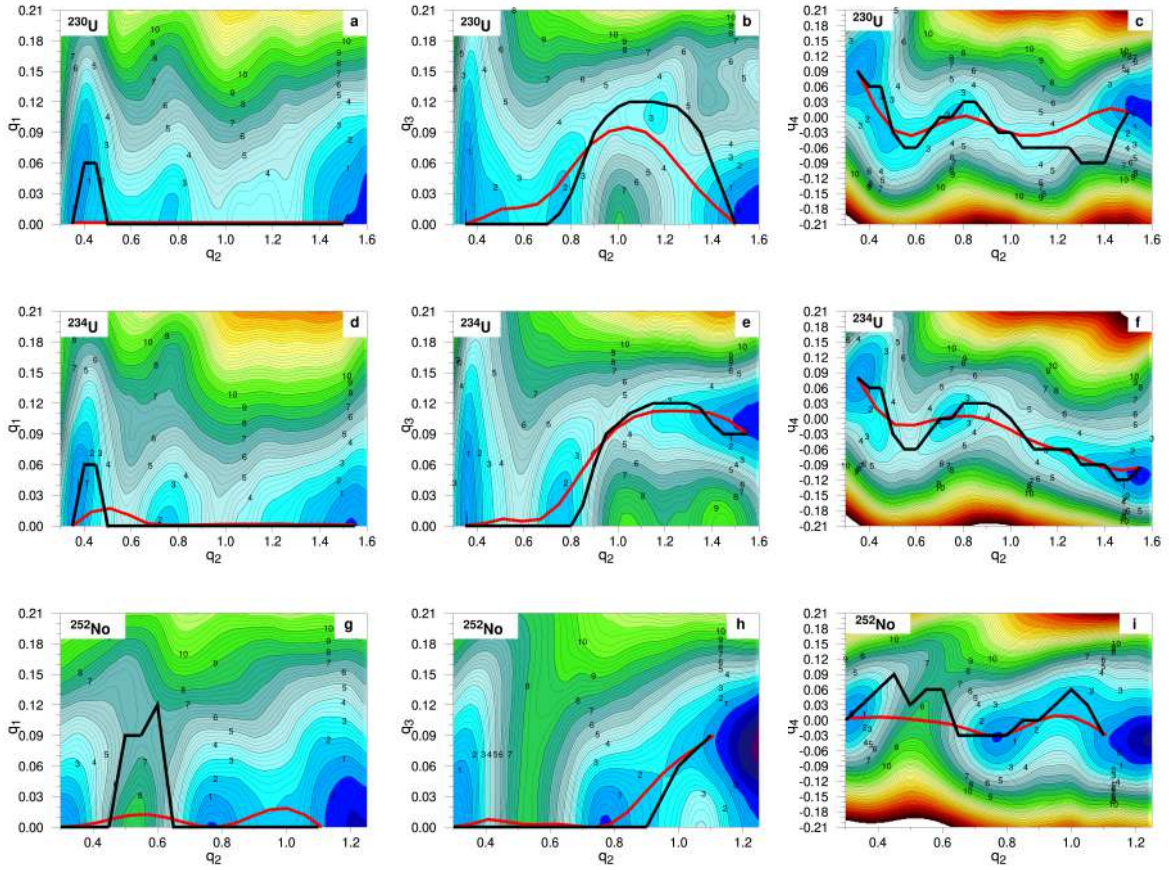
Figure 13.2: Potential energy surfaces for ^{230}U (a-c), ^{234}U (d-f) and ^{252}No (g-i) isotopes projected onto the (q_2, q_1), (q_2, q_3) and (q_2, q_4) deformation 2D subspaces. The projection is performed in such a way that the other two variables $q_k(q_2)$ and $q_{k'}(q_2)$ take values that minimize the action (13.1) between the ground-state and the exit points. The solid red and black lines correspond respectively to the LAP with the hydrodynamical mass tensor and the least-energy path (LEP).

We will now explain a method that has been shown to work well in determining the least-action path in a 4D deformation space with the full hydrodynamical mass tensor, which will then be used to calculate the penetration probability through the fission barrier to determine the spontaneous fission half-lives. This method is based on the idea firstly introduced by Ritz (50) and effectively utilized especially for investigating the phenomenon of spontaneous fission (see e.g. Refs. (51; 52; 47)).

We need to find a path within our 4D deformation space, that is why it is possible to approximate any continuous and bounded function over a finite interval of its arguments by a Fourier-type expansion. As long as the endpoints of the path are fixed, this expansion should only involve a series of *sin* functions, in addition to an average path, given by a straight line connecting the ground state and the exit points.

The end points of the average path are the ground state and the point, which is identified by the identical energy as the ground state. Treating the elongation parameter q_2 as the fundamental variable responsible for the evolution of a nucleus to fission, one can approximate the deformation parameters q_1, q_3, and q_4 along the least-action path as functions of q_2 in the following way:

$$q_\nu^{(\text{LAP})}(q_2) = \left[q_{\nu_{g.s.}} + \frac{(q_{\nu_{exit}} - q_{\nu_{g.s.}})(q_2 - q_{2_{g.s.}})}{q_{2_{exit}} - q_{2_{g.s.}}} \right.$$
$$\left. + \sum_{\ell=1}^{N_F} a_\ell \, sin \left(\ell\pi \frac{q_2 - q_{2_{g.s.}}}{q_{2_{exit}} - q_{2_{g.s.}}} \right) \right], \quad \nu = 1, 3, 4 \tag{13.3}$$

the amplitudes a_ℓ of the series expansion are treated as variational parameters in the search for the minimum of the action integral (13.1). The upper limit N_F for the Fourier series expansion in each direction of the least-action path (13.3) must be selected such that the final result for the tunneling probability becomes essentially independent of N_F.

We found that a value of $N_F = 8$ is sufficient to achieve good convergence of Fourier series (13.3) and therefore a well-converged tunneling probability.

By obtaining the least-action integral value with respect to the a_ℓ amplitudes, we obtain the path evolution for a specific nucleus in the 4D deformation space under consideration.

13.3   Results

In Figures 13.2, we present the projections of the complete 4D potential energy surface (PES) onto the 2D subspaces of (q_2, q_1), (q_2, q_3), and (q_2, q_4) for ^{230}U, ^{234}U, and ^{252}No. The other two deformation parameters are the functions of the elongation q_2, which minimize the action integral (13.1) between the ground state and the true exit point. The thick red line shows the evolution of the LAP using the aforementioned hydrodynamic mass tensor in these regions. The selected isotopes span from light to heavy actinides. It is clear to see that the PES and its linked LAP possess distinct characteristics in these extreme scenarios.

In the lighter actinides, the PES shows a stronger dependence on deformation due to the

significance of shell effects, which is not present in the heavy No isotope. As a result, the fission barriers in uranium isotopes are usually higher and longer before reaching the scission configuration, unlike in nobelium. On the basis of this preliminary qualitative analysis, one can predict a shorter half-life for nobelium relative to uranium, a conclusion that agrees with experimental data.

As can be inferred from Eq. (13.1), the final part of the LAP in the multi-dimensional deformation space is determined by the interplay between the PES dependent on deformation and the inertia tensor. This is why the LAP is typically shorter than the least energy path (LEP) and generally passes through higher energy configurations (sometimes by up to 2 MeV) than the LEP. The actions along both trajectories may vary significantly, resulting in considerable differences between the estimates of fission half-lives, sometimes reaching several orders of magnitude.

As demonstrated in part (e) of Figure 13.2, the LAP for ^{234}U originates from the mass-symmetric ground state and remains left-right symmetric ($q_3 = 0$) up to the second minimum. It then proceeds towards asymmetric shapes around $q_2 \approx 0.7$, finally leading to an asymmetric fission valley at a value of $q_3 \approx 0.08$. It is therefore important to consider the mass asymmetry degree of freedom after the second minimum. One observes that in ^{234}U, the LEP and LAP remain in close proximity in the (q_2, q_3) plane. Panel (f) of Fig. 13.2 indicates that LAP displays minor deviations from a linear trend in the (q_2, q_4) subspace, with a compact ground-state shape at $q_4 \approx 0.08$ transitioning to moderately elongated necked shapes at $q_4 \approx -0.12$.

Regarding the lack of axial symmetry in panel (d), the LAP between the ground state and the second minimum runs via moderately non-axial shapes before returning to the axial path at $q_2 = 0.65$. A similar pattern is observed in the super-heavy ^{252}No nucleus, as shown in panels (g)-(i). However, in this case, the LAP ends at $q_2 = 1.1$, making it much shorter than the one observed in ^{234}U. In contrast, for ^{230}U (as shown in panels (a)-(c)), the deformation q_3 is almost not present in the initial and final parts of the LAP, whereas at intermediate elongations, it surpasses values beyond $q_3 \approx 0.1$ to pass the energy maximum (barrier) peaked at $q_2 \approx 1$.

In both of the discussed uranium isotopes, their LAPs $q_4(q_2)$, as presented in panels (c) and (f), exhibit similar shapes.

It is remarkable that the LAP in this nucleus favours fully axial shapes throughout, despite the fact that the LEP goes through energetically lower, non-axial configurations at very small deformations just beyond the equilibrium point.

In order to maintain the precision of our calculations while keeping the computation time within reasonable limits, we can utilize up to a maximum of $N_F^{tot} = 3 \times N_F = 24$ harmonic components of the Fourier series in Eq. (13.3).

In a high number of dimensions, differentiating between a local and global minimum of the action integral can become more and more problematic. To prevent this issue, we initiate the calculations for every nucleus with a low value of N_F, such as $N_F = 3$, for the two functions $q_3(q_2)$ and $q_4(q_2)$, on top of the average path. We then gradually increase N_F, checking for convergence after each step.

We may prove that limiting ourselves to the initial few elements of these sequences, such as for example $N_F = 6 - 8$, brings about LAPs as depicted in Fig. 13.2 that are indiscernible visually from those obtained with greater values of N_F. After calculating the action value S, the spontaneous fission lifetime can be determined using the standard WKB relations (53).

$$T_{1/2}^{(\text{sf})} = \frac{2\pi \ln(2)}{\omega_0} \left(1 + e^{2S}\right), \tag{13.4}$$

with the term $E_{\text{ZPE}} \approx \frac{1}{2}\hbar\omega_0$ referring to the zero-point vibration energy, typically considered to be within the $0.5 - 1$ MeV. In the present study, we selected a particular value of $E_{\text{ZPE}} = 0.5\,\text{MeV}$.

Spontaneous fission half-lives were determined for several isotopes of actinide nuclei, including thorium (Th), uranium (U), plutonium (Pu), curium (Cm), californium (Cf), and fermium (Fm), and for superheavy isotopes of nobelium (Nb), rutherfordium (Rf), seaborgium (Sg), hassium (Hs), and darmstadtium (Ds), where experimental data were available (54).

The outcomes of the computations acquired by re-scaling (by using the value of scaling parameter β) the hydrodynamical mass tensor and using the original phenomenological mass formula (13.2) are demonstrated in Fig. 13.3, alongside the recorded values. The

information related to the diverse isotopes computed using the method detailed above
are displayed as open blue circles and black triangles, whereas the experimental data are
depicted as solid red circles.
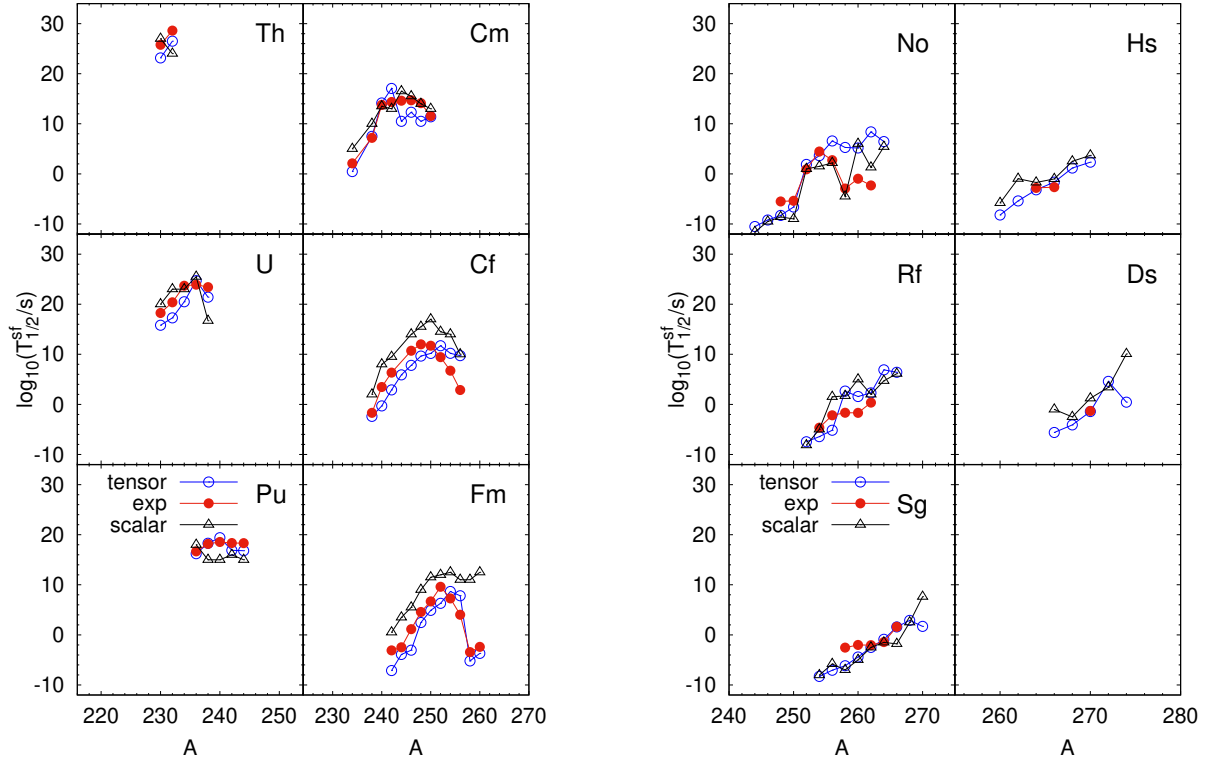
Figure 13.3: (Top panel) Comparison of spontaneous fission half-lives for actinide
nuclei obtained in full 4D WKB approach with the irrotational flow hydrodynamical mass
tensor (open circles) and the phenomenological inertia with 3D (with non-axiality treated
in a static way) PES, Eq. (13.2) (open triangles) with the experimental data (full red
circles). (Bottom panel) shows the same but for super-heavy elements from nobelium to
darmstadtium.

In order to establish a systematic approach for the half-lives of spontaneous fission as
shown in Fig. 13.3 of all actinide and super-heavy element isotopic chains up to $Z = 110$,
we have fine-tuned the parameter β in Eq. (13.1) through χ^2 minimization to all 39
measured half-lives of actinide nuclei from thorium to fermium. Our studies reveal that a
value of $\beta = 5$ effectively reproduces the half-lives of all reported actinides.

By selecting a smaller nucleus sample, we ensure that the value of $\beta = 5$ stays, in fact,
practically unaffected. This particular β value guarantees that the logarithm of the
calculated half-lives in super-heavy nuclei remains within reasonable limits of about $2 - 3$

(in units of $1/s$), which can be compared with other current assessments (56; 57). Let us note that, as shown in Ref. (58), the hydrodynamic inertia employed in our approach may significantly deviate from the microscopic mass tensors frequently obtained within the cranking or GCM+GOA model, sometimes by a factor of almost $3-5$ on average. This primarily holds true for compact shapes (with $q_2 \approx 1$), where the fission barrier is located. Once the β value is determined, calculations with this particular value are conducted to determine the fission half-lives for super-heavy elements and compare them to experimental data.

Let it be noted that the hydrodynamical inertia tensor has yielded fruitful results in the computation of fission features for shapes situated closely to the scission configuration, such as fragment mass or charge distributions using a stochastic Langevin modeling of classical trajectories. In contrast, barrier penetration takes place at significantly lower elongations around the fission barrier (see, Ref. (59)).

As depicted in Figure 13.1, the inertia components B_{22} and B_{33}, which play a vital role in barrier penetration, are considerably smaller near the barrier region compared to those near the scission. Nonetheless, it is important to recall that the pure hydrodynamical approach, in its original form, is not ideal for accurately describing effective inertia near the barrier.

The phenomenological mass parameter (13.2), however, comprises the rigid-body inertia as a contribution, along with a term (regulated by the parameter k) defined by the difference between the rigid body and the irrotational flow inertia, consequently enhancing its credibility in the fission-barrier region.

Investigating the results from Fig. 13.3, our approach using pure hydrodynamical inertia tensor appears capable of reproducing the experimental fission half-lives for actinides. However, there are a few cases that deviate significantly from their isotopic systematics, such as certain isotopes of Cm and the heaviest Cf nuclei, which require further understanding.

To account for these differences, it is possible to reference a recent study (7). The study recalls a simple analytical 1D WKB approach, modeled on the Swiatecki-like systematics (5) of spontaneous fission half-lives. It demonstrates that the primary factor deciding the

magnitude of the fission half-life is the height of the fission barrier, E_B. The function $f(E_B)$ (provided in equations (10.5) and (10.6) of Ref. (7)), which is utilized universally for heavy and super-heavy elements, already accounts for the impact of the other fission barrier's properties, including the barrier width.

At this juncture, it may be worth recalling a truth known for years that even a minor change in the fission barrier height results in a significant reduction or augmentation of the tunneling probability. This, in turn, generates adequate variations of fission half-lives.

Another noteworthy instance is that of the $^{232-234}$U isotopes, in which our macroscopic-microscopic model undervalues the fission barrier heights by approximately $1 - 2$ MeV (see, Ref. (60) as well), leading to a reduction in the half-life of fission by up to 2-4 orders of magnitude. A comparable effect can be observed for the $^{242-246}$Cm isotopes, where the differences between the experimental and theoretical first and second barriers are most significant across the entire isotopic chain.

The lifetime overestimation in superheavy isotopes $^{258-262}$No and $^{256-260}$Rf may be similar to that of the actinides. However, quantitative comparisons cannot be made yet because the experimental barriers remain unknown.

It is worth noting that Fig. 13.3 presents the half-life calculations for actinide nuclei achieved using the phenomenological inertia of Eq. (13.2) at the three-dimensional PES. In this PES, the total 4D energy function is minimized for a particular (q_2, q_3, q_4) coordinate with respect to the non-axiality parameter q_1, giving effectively the deformation space of 3 dimensions.

Comparing the masses obtained using the above mentioned two approximations, the half-lives calculated through the full 4D WKB dynamics and complete hydrodynamical inertia tensor using a scaling factor of $\beta = 5$ (uniform across all tensor components) are significantly closer to the experimental data than those obtained through the phenomenological scalar mass described by Eq. (13.2). This indicates that taking into account the complete description of a system's inertial properties at every deformation point, as well as including as many relevant degrees of freedom for fission dynamics as possible, results in a significant enhancement of fission lifetime estimations.

13.3.1   WKB dynamics without non-axial deformation

In the following discussion, we show the results of half-live calculations for the same set of nuclei as before, but with the non-axial degrees of freedom treated in a static way. This means that the path of the least action is defined in a deformation space containing only 3 independent key deformation variables, i.e. $\{q_2, q_3, q_4\}$. Obviously, the non-axiality q_1 is taken into account but it is done in such a way that the full potential energy function $E(q_1, q_2, q_3, q_4)$ is minimized with respect to this variable at each deformation point (q_2, q_3, q_4). Thus, one can say, that we are dealing with a kind of "hybrid" fission path, where its branch of least-action is defined in the 3D $\{q_1^0; q_2, q_3, q_4\}$ collective subspace while the branch $q_1^0(q_2)$ leads through the least-energy configurations $E(q_1^0; q_2, q_3, q_4)$ between the equilibrium and exit states.
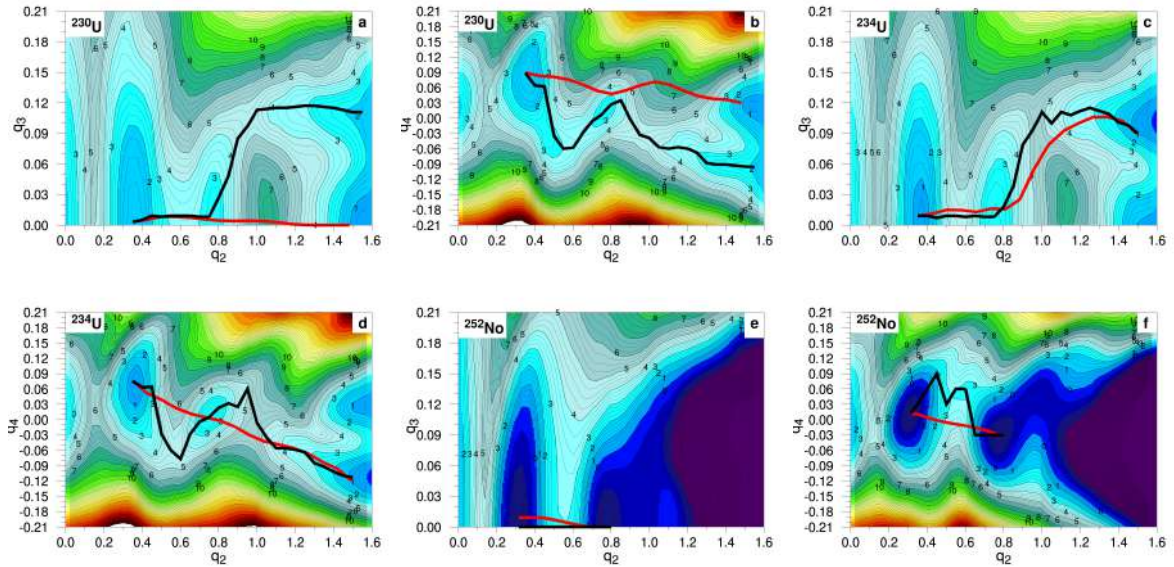
Figure 13.4: Potential energy surfaces for ^{230}U (a,b), ^{234}U (c,d) and ^{252}No (e,f) isotopes projected onto the (q_2, q_3) deformation subspace with minimization with respect to η and q_4 (left column), and onto the (q_2, q_4) subspace, with minimization with respect to η and q_3 (right column). The solid red and black curves correspond respectively to the LAP obtained with the hydrodynamical mass tensor and the least-energy path (LEP) obtained with the phenomenological mass parameter of Eq. (13.2).

In Figs. 13.4 we present, for ^{230}U, ^{234}U and ^{252}No, the projections of the full 4-dimensional PES onto the 2D sub-spaces (q_2, q_3) and (q_2, q_4) with minimization with respect to the two remaining deformation parameters $(q_4, \eta$ and q_3, η, respectively). The evolution of the LAP obtained when using the above discussed hydrodynamical mass tensor in these landscapes is indicated by the thick red line. These isotopes have been chosen to cover

the region from light to heavy actinides. As can be seen, the PES and the associated LAP in these extreme cases have different characteristics. In the lighter actinides, due to the importance of the shell effects, the PES shows a stronger deformation dependence than in the heavy No isotope. Consequently, the fission barrier in uranium, unlike in nobelium, is higher and shows two minima and two saddle points before reaching the scission configuration. Already from this quick qualitative analysis, one can expect a shorter half-life for nobelium as compared to uranium, an analysis which turns out to be consistent with the experiment.

As one can see from part (c) of Fig. 13.4 the LAP for ^{234}U starts from the mass-symmetric ground state, stays left-right symmetric ($q_3 = 0$) up to the second minimum and then rapidly evolves towards asymmetric shapes around $q_2 \approx 0.8$, leading finally to an asymmetric fission valley at a value of $q_3 \approx 0.11$. One thus concludes that it is absolutely crucial to take into account the mass asymmetry degree of freedom beyond the second minimum ($0.75 \lesssim q_2 \lesssim 1$). One notices that for the ^{234}U nucleus the LEP and the LAP stay close to each other in the (q_2, q_3) plane. When looking at the (q_2, q_4) plane for the same nucleus (see panel (d) of Fig. 13.4), one finds that the LAP shows an almost linearly behaviour between a compact ground-state shape at $q_4 \approx 0.07$ and a medium-elongated necked shapes at $q_4 \approx -0.12$. For the ^{230}U (panels (a) and (b)) and the ^{252}No nucleus (panels (e),(f)), on the contrary, the q_3 deformation is almost negligible for the LAP, whereas the LEP, unlike the LAP, passes, beyond the second minimum, through significantly mass-asymmetric shapes, in particular for ^{230}U, leading there towards a fission valley at $q_3 \approx 0.12$. In all three cases (panels (b), (d) and (f)) the LAP shows in the (q_2, q_4) plane an almost linear decrease of the neck parameter q_4 with elongation. In all, the evolution of the LAP and LEP in the deformation-energy landscapes is a clear indication that **at least**, the q_3, as well as the q_4 deformation degrees of freedom, are indispensable for a correct description of the fission process.

Now we come to the comparison of the half-lives generated in, say (3+1)D, WKB dynamical approach, presented in Fig. 13.5 and the results based on the full 4D WKB dynamical simulations, visualized in Fig.13.3. We can immediately see that they are generally similar within 2-3 orders of magnitude. In more detail, there are cases where the dynamic treatment of non-axiality improves the predictions with respect to the experimental results,

but there are also several nuclei for which, on the contrary, the theoretical values have moved somewhat away from their experimental counterparts.

For example, there are cases as ^{236}U, ^{242}Fm and ^{262}No, which in 3D calculations protruded dramatically beyond the half-lives trend line, and which, given the non-axiality, managed to approach it. Unfortunately, for the entire Cf isotope series, a slightly larger deviation from the experimental values can be observed when one allows the system to have inertia in the direction of the non-axial deformation.

For the other isotopes studied, the results with and without non-axiality as a dynamic variable in Eq. 13.1 are, as mentioned above, very similar. Therefore, one may venture to say that the non-axiality coordinate can be seen as being of a second order of importance compared to elongation, mass asymmetry and neck width in determining fission half-lives in heavy and super-heavy nuclei.
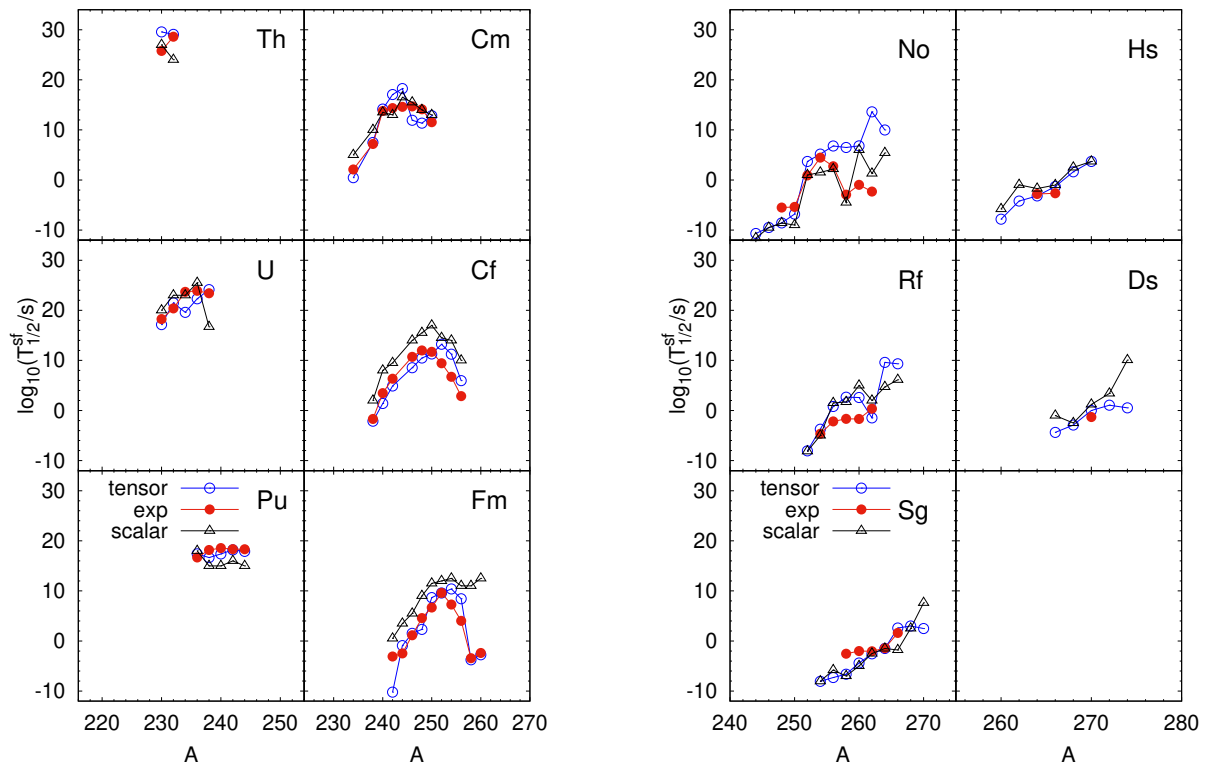
Figure 13.5: (Top panel) Spontaneous fission half-lives for actinides obtained in above outlined (3+1)D WKB approach with the irrotational flow hydrodynamical mass tensor (open circles) and the phenomenological inertia, Eq. (13.2) (open triangles). The experimental data are represented by full red circles. (Bottom panel) same but for super-heavy elements from nobelium to darmstadtium.

13.4   Conclusions

Taking into account the applied with great success "water flow" method, the energies and corresponding deformations of the saddle points of the potential energy functions in the four-dimensional Fourier deformation space are found. When, in addition, the ground state and isomeric energy minima have been determined using standard numerical gradient minimisation techniques in multi-dimensional spaces, one was also able to calculate the barrier heights for the fission process for even-even and odd nuclei and compare with available empirical values.

Spontaneous fission half-lives have been calculated for nuclei with $90 \leq Z \leq 104$ utilizing the macroscopic-microscopic approach, together with the Lublin-Strasbourg Drop model. A mean field was generated using a Yukawa-folding method and a constant G seniority BCS pairing treatment with a GCM+GOA particle-number projection. The strength of pairing interaction G has been re-fitted using as a database all 39 actinide nuclei in which the experimental ground-state masses are known.

The fission dynamics has been simulated using the semiclassical WKB method. The least-action integral as a result of these simulations, describes the evolution of the nucleus in a four-dimensional deformation space where the surface of a nucleus is decomposed into a Fourier series in a cylindrical coordinate system. These coefficients of the Fourier series represent the collective elongation, mass asymmetry, non-axiality, and neck degrees of freedom.

In order to consider the change in collective inertia along the fission pathway, we incorporated the irrotational flow mass tensor with a scaling factor of 5 into the action-integral expression. This replicates the fission half-lives in the actinide region with accuracy.

Since the resulting least-action path towards fission has a tendency, to some extent, to exclude states in which the inertia changes drastically, owing to the presence of shell effects, the use of this ostensibly macroscopic collective inertia model appears to be highly appropriate. For comparison purposes, we have also conducted comparable calculations of fission lifetimes using a collective mass parameter, as described in Eq. (13.2), which has resulted in reasonably accurate replication of fission half-lives across a broad spectrum of

actinide and super-heavy nuclei.

One can observe that both of these inertia approaches tend to produce very similar values of the spontaneous fission half-lives $T_{1/2}$, especially in super-heavy nuclei and in the actinide isotopes of thorium, uranium, plutonium, and curium. However, when it comes to californium and fermium, the use of the collective mass parameter Eq. (13.2) and 3D PES results in a mean deviation that exceeds the experimental data by several orders of magnitude.

One should note that the phenomenological mass formula (13.2) is a hybrid approach. This approach combines the hydrodynamical and rigid-body approaches to evaluate nuclear collective inertia and requires 3 adjustable parameters to reproduce spontaneous fission half-lives. In contrast, our approach using the irrotational flow mass tensor yields better results with a single adjustable parameter, the parameter β, in the expression (13.1) for the action integral.

Let us note here that our approach does not require any correction for zero-point energy, and to do so would conflict with the philosophy of our macroscopic-microscopic model. This model, which is similar to the mean-field Hartree-Fock type framework, uses a variational approach to describe nuclear energy, and thus there is no room for artificial elevations or reductions of ground-state energy.

One should bear in mind that spontaneous fission is but one potential nuclear decay route, contending with the release of light particles (such as neutron or proton or γ quanta), or the discharge of light clusters (such as α particles). We are currently exploring the interplay between fission and these other mechanisms, which will be detailed in an upcoming publication.

A   Appendix: Tables with values of GS, saddle points and barrier heights

In this appendix, we show in form of tables the numerical results of the energies obtained in our calculation of important points such as the ground-state, the saddle points and the barrier heights. The calculation was performed in the 4D deformation space using the elongation q_2, left-right asymmetry q_3, neck q_4 and non-axial η parameters. A grid composed of 202500 different deformation points for each of 118 even-even nuclei from thorium to rutherfordium. It means that the results shown in the following tables are obtained by evaluating the macroscopic and microscopic model 24.000.000 points. The analysis of this huge amount of data which brought results in the tables was a kind of "Benedictine works" done mostly by the author.

The following notation is used in the tables:

- **GS:** ground state energy (MeV)

- **2M:** second minimum energy (MeV)

- **1SP:** first saddle point energy (MeV)

- **2SP:** second saddle point energy (MeV)

- **BA1:** first saddle point energy - ground state energy (MeV)

- **BA2:** second saddle point energy - ground state energy (MeV)

- **BB1:** first saddle point energy - second minimum energy (MeV)

- **BB2:** second saddle point energy - second minimum energy (MeV)

- **2M-GS:** second minimum energy - ground state energy (MeV)

- **HB:** highest barrier (MeV)

- **Exp:** experimental values (MeV)(61)

Our estimates of all above mentioned stationary points are shown in eight tables separated for each element from Th to Rf. Available experimental data for the fission barrier heights are shown in the last column of each table.

Table A.1: Thorium

A	GS	2M	1SP	2SP	BA1	BA2	BB1	BB2	2M-GS	HB	Exp
200	1.80	2.28	3.12	2.77	1.33	0.98	0.85	0.50	0.48	1.33	
202	2.21	2.46	2.91	3.90	0.70	1.69	0.45	1.44	0.25	1.69	
204	1.28	2.04	3.58	5.21	2.30	3.93	1.54	3.17	0.75	3.93	
206	0.93	2.06	4.14	6.24	3.21	5.31	2.08	4.18	1.13	5.31	
208	-0.36	1.97	4.27	6.16	4.63	6.52	2.30	4.19	2.33	6.52	
210	-1.16	2.23	4.26	6.66	5.42	7.82	2.03	4.43	3.39	7.82	
212	-1.87	2.67	4.49	7.18	6.36	9.05	1.82	4.51	4.54	9.05	
214	-2.79	2.65	4.61	7.91	7.40	10.69	1.96	5.26	5.44	10.69	
216	-3.99	2.95	4.50	8.36	8.49	12.35	1.55	5.41	6.94	12.35	
218	2.94	3.05	4.41	8.47	1.47	5.53	1.36	5.43	0.10	5.53	
220	0.71	2.91	4.26	7.77	3.55	7.06	1.35	4.85	2.20	7.06	
222	1.29	2.43	3.95	7.06	2.66	5.77	1.52	4.63	1.14	5.77	
224	2.06	2.94	4.57	6.90	2.52	4.84	1.64	3.96	0.88	4.84	
226	2.45	3.13	4.64	6.73	2.19	4.27	1.51	3.60	0.68	4.27	6.2
228	1.96	3.54	4.34	6.64	2.38	4.68	0.80	3.10	1.58	4.68	6.1
230	1.56	3.19	4.69	7.17	3.13	5.61	1.51	3.99	1.63	5.61	5.8
232	1.75	2.92	5.32	6.82	3.57	5.07	2.40	3.90	1.17	5.07	6.1
234	1.32	2.80	5.28	6.73	3.97	5.41	2.49	3.93	1.48	5.41	
236	1.34	2.65	6.50	7.04	5.16	5.70	3.85	4.39	1.31	5.70	
238	1.10	3.04	6.71	7.18	5.62	6.08	3.67	4.14	1.94	6.08	
240	0.81	3.10	6.65	7.51	5.84	6.70	3.55	4.41	2.29	6.70	

Table A.2: Uranium

A	GS	2M	1SP	2SP	BA1	BA2	BB1	BB2	2M-GS	HB	Exp
220	2.32	2.28	3.23	6.61	0.91	4.29	0.95	4.32	-0.03	4.29	
222	2.45	2.22	4.26	6.53	1.80	4.08	2.03	4.31	-0.23	4.08	
224	2.44	1.71	3.62	5.71	1.18	3.27	1.91	4.00	-0.73	3.27	
226	2.35	2.35	3.81	5.75	1.45	3.40	1.45	3.40	0.00	3.40	
228	1.87	2.59	3.88	5.60	2.01	3.73	1.29	3.01	0.72	3.73	
230	1.56	2.96	3.62	5.50	2.06	3.94	0.67	2.54	1.39	3.94	
232	1.14	2.61	4.58	5.56	3.43	4.42	1.97	2.95	1.47	4.42	5.4
234	1.12	2.47	5.16	5.87	4.04	4.75	2.69	3.41	1.35	4.75	5.9
236	0.67	2.34	5.87	5.99	5.20	5.33	3.53	3.66	1.67	5.33	5.6
238	0.69	2.09	6.43	6.06	5.74	5.38	4.34	3.97	1.41	5.74	6
240	0.56	2.49	6.78	6.45	6.22	5.89	4.28	3.96	1.93	6.22	6.1
242	0.46	2.34	6.71	6.96	6.25	6.50	4.37	4.61	1.88	6.50	
244	0.90	2.99	6.25	7.40	5.35	6.51	3.26	4.41	2.09	6.51	
246	1.21	3.23	6.61	7.66	5.40	6.45	3.38	4.43	2.02	6.45	
248	1.50	3.67	6.10	7.67	4.60	6.17	2.43	4.00	2.17	6.17	

Table A.3: Plutonium

A	GS	2M	1SP	2SP	BA1	BA2	BB1	BB2	2M-GS	HB	Exp
222	0.63	2.01	2.74	5.19	2.11	4.56	0.73	3.18	1.39	4.56	
224	1.91	2.40	2.57	5.22	0.66	3.31	0.17	2.82	0.49	3.31	
226	1.93	2.60	3.36	4.49	1.43	2.56	0.75	1.89	0.68	2.56	
228	2.02	2.82		4.48		2.46		1.66	0.80	2.46	
230	1.35	2.26		4.36		3.01		2.10	0.91	3.01	
232	0.78	2.12	3.79	4.03	3.01	3.26	1.67	1.92	1.34	3.26	
234	1.14	1.81	4.77	4.37	3.63	3.23	2.96	2.56	0.67	3.63	
236	0.23	1.68	5.36	4.60	5.13	4.37	3.69	2.92	1.44	5.13	5.7
238	-0.21	1.64	6.17	4.71	6.38	4.93	4.52	3.07	1.86	6.38	5.9
240	-0.18	1.43	6.34	4.89	6.52	5.07	4.92	3.47	1.61	6.52	5.8
242	-0.32	1.81	6.27	5.46	6.59	5.77	4.46	3.65	2.13	6.59	5.7
244	-0.48	1.77	6.37	5.85	6.85	6.33	4.61	4.09	2.24	6.85	5.5
246	-0.16	2.27	5.87	6.15	6.03	6.31	3.60	3.87	2.44	6.31	5.4
248	0.03	2.53	6.12	6.33	6.09	6.30	3.59	3.80	2.50	6.30	
250	0.52	2.64	5.55	6.40	5.03	5.88	2.91	3.77	2.12	5.88	

Table A.4: Curium

A	GS	2M	1SP	2SP	BA1	BA2	BB1	BB2	2M-GS	HB	Exp
224	1.87	1.90	2.28	3.53	0.41	1.66	0.37	1.63	0.04	1.66	
226	1.65	1.73	2.68	3.66	1.03	2.01	0.95	1.93	0.08	2.01	
228	1.44	1.62	3.01	3.40	1.57	1.96	1.39	1.78	0.18	1.96	
230	1.21	1.71	2.82	3.48	1.61	2.27	1.11	1.77	0.50	2.27	
232	0.68	1.29	3.19	3.36	2.51	2.68	1.90	2.07	0.61	2.68	
234	0.57	1.10	3.94	2.84	3.38	2.28	2.84	1.74	0.54	3.38	
236	0.22	0.76	4.96	2.93	4.74	2.71	4.20	2.17	0.54	4.74	
238	0.05	0.60	5.57	3.18	5.52	3.13	4.97	2.58	0.55	5.52	
240	-0.44	0.47	5.86	3.15	6.30	3.59	5.39	2.68	0.91	6.30	
242	-0.50	0.23	5.76	3.30	6.26	3.79	5.53	3.06	0.73	6.26	6
244	-0.75	0.59	5.84	3.91	6.58	4.66	5.24	3.32	1.34	6.58	6.1
246	-1.00	0.50	5.75	4.36	6.76	5.36	5.26	3.86	1.50	6.76	6
248	-0.74	1.04	5.61	4.86	6.35	5.60	4.57	3.82	1.78	6.35	5.9
250	-0.60	1.29	5.45	5.19	6.06	5.79	4.16	3.89	1.90	6.06	5.4
252	-0.19	1.41	4.78	5.00	4.96	5.19	3.37	3.60	1.59	5.19	

Table A.5: Californium

A	GS	2M	1SP	2SP	BA1	BA2	BB1	BB2	2M-GS	HB	Exp
238	-0.50	-0.91	4.53	1.36	5.03	1.86	5.44	2.27	-0.41	5.03	
240	-0.85	-0.87	4.76	1.29	5.61	2.14	5.63	2.16	-0.02	5.61	
242	-1.27	-0.91	5.05	1.18	6.32	2.45	5.96	2.09	0.36	6.32	
244	-1.32	-1.06	5.21	1.66	6.52	2.98	6.26	2.72	0.26	6.52	
246	-1.72	-0.70	5.29	2.28	7.01	4.00	5.99	2.97	1.02	7.01	
248	-2.03	-0.83	5.35	2.86	7.38	4.89	6.18	3.69	1.21	7.38	
250	-1.76	-0.29	5.11	3.51	6.87	5.27	5.41	3.80	1.47	6.87	5.6
252	-1.64	-1.53	4.88	3.83	6.52	5.47	6.41	5.35	0.12	6.52	5.3
254	-1.19	0.07	4.49	3.37	5.68	4.56	4.42	3.30	1.26	5.68	
256	-0.84	0.35	4.44	2.52	5.29	3.36	4.09	2.17	1.19	5.29	
258	-0.99	0.37	4.42	1.71	5.41	2.69	4.05	1.34	1.36	5.41	
260	-0.60	0.40	4.42	1.20	5.02	1.80	4.02	0.80	1.01	5.02	

Table A.6: Fermium

A	GS	2M	1SP	2SP	BA1	BA2	BB1	BB2	2M-GS	HB	Exp
240	-0.19	-2.13	3.92	-0.90	4.11	-0.71	6.04	1.23	-1.94	4.11	
242	-0.64	-2.02	4.12	-0.49	4.76	0.16	6.13	1.53	-1.37	4.76	
244	-1.10	-1.87	4.21	-0.55	5.31	0.55	6.08	1.32	-0.77	5.31	
246	-1.20	-1.94	4.46	0.07	5.66	1.27	6.41	2.02	-0.75	5.66	
248	-1.71	-1.53	4.43	0.46	6.14	2.17	5.97	1.99	0.17	6.14	
250	-2.10	-1.69	4.36	1.05	6.45	3.14	6.05	2.74	0.40	6.45	
252	-1.98	-1.28	4.43	1.75	6.42	3.73	5.71	3.03	0.70	6.42	
254	-1.94	-1.09	4.06	2.02	5.99	3.96	5.14	3.11	0.85	5.99	
256	-1.57	-1.14	3.71	1.28	5.28	2.85	4.85	2.42	0.43	5.28	
258	-1.38	-0.86	3.70	0.89	5.08	2.26	4.56	1.75	0.52	5.08	
260	-1.63	-1.15	3.86	0.19	5.49	1.83	5.00	1.34	0.49	5.49	
262	-1.39	-1.35	3.96	0.21	5.35	1.60	5.31	1.56	0.05	5.35	

Table A.7: Nobelium

A	GS	2M	1SP	2SP	BA1	BA2	BB1	BB2	2M-GS	HB	Exp
242	-0.41	-3.60	3.21	-2.01	3.62	-1.60	6.81	1.59	-3.19	6.81	
244	-0.86	-3.39	3.34	-2.34	4.20	-1.48	6.72	1.05	-2.53	6.72	
246	-1.39	-3.36	3.46	-2.36	4.84	-0.97	6.81	1.00	-1.97	6.81	
248	-1.55	-3.37	3.63	-1.71	5.18	-0.16	7.00	1.66	-1.82	7.00	
250	-2.18	-2.95	3.64	-1.33	5.82	0.85	6.60	1.62	-0.78	6.60	
252	-2.72	-3.09	3.68	-0.86	6.41	1.87	6.78	2.24	-0.37	6.78	
254	-2.64	-2.71	3.61	-0.28	6.24	2.36	6.32	2.43	-0.08	6.32	
256	-2.68	-2.61	3.47	0.00	6.14	2.68	6.08	2.61	0.07	6.14	
258	-2.42	-2.70	3.61	0.21	6.03	2.63	6.31	2.90	-0.28	6.31	
260	-2.30	-2.34	3.69	-0.24	5.99	2.06	6.02	2.10	-0.03	6.02	
262	-2.68	-2.60	3.82	-1.50	6.50	1.19	6.42	1.11	0.08	6.50	
264	-2.53	-2.74	3.92	-1.74	6.45	0.79	6.66	1.00	-0.21	6.66	

Table A.8: Rutherfordium

A	GS	2M	1SP	2SP	BA1	BA2	BB1	BB2	2M-GS	HB	Exp
250	-13.29	-18.21	-9.16	-4.89	4.13	8.41	9.04	13.32	-4.91	13.32	
252	-12.81	-17.95	-9.20	-4.62	3.60	8.19	8.75	13.33	-5.15	13.33	
254	-12.21	-17.67	-9.20	-4.22	3.01	7.99	8.47	13.45	-5.46	13.45	
256	-12.00	-17.43	-9.11	-3.74	2.89	8.26	8.32	13.69	-5.43	13.69	
258	-11.72	-17.51	-9.32	-3.47	2.40	8.25	8.19	14.04	-5.79	14.04	
260	-11.76	-17.58	-9.06	-3.33	2.70	8.44	8.52	14.26	-5.82	14.26	
262	-11.50	-17.91	-9.19	-3.36	2.31	8.14	8.72	14.55	-6.41	14.55	
264	-11.31	-17.63	-9.00	-3.38	2.31	7.93	8.63	14.25	-6.32	14.25	
266	-10.81	-17.51	-9.25	-3.74	1.57	7.08	8.26	13.78	-6.70	13.78	
268	-10.15	-18.50	-10.00	-3.91	0.15	6.24	8.50	14.59	-8.35	14.59	
270	-9.90	-20.00	-10.32	-3.97	-0.43	5.92	9.67	16.02	-10.10	16.02	
272	-9.48	-20.88	-10.03	-3.94	-0.55	5.54	10.85	16.94	-11.40	16.94	
274	-9.28	-21.89	-9.78	-3.76	-0.50	5.52	12.11	18.13	-12.61	18.13	
276	-9.13	-22.37	-10.12	-3.67	-0.99	5.46	12.26	18.70	-13.24	18.70	
278	-9.13	-22.55	-10.39	-3.85	-1.27	5.27	12.15	18.69	-13.42	18.69	
280	-9.06	-22.33	-10.29	-4.17	-1.22	4.90	12.04	18.16	-13.26	18.16	
282	-9.39	-22.16	-10.66	-3.83	-1.27	5.56	11.50	18.33	-12.77	18.33	
284	-9.48	-21.20	-11.25	-4.07	-1.77	5.42	9.95	17.14	-11.72	17.14	

B Appendix: Fission barrier heights and the GS and the saddle point positions obtained with the new pairing strength

With this new adjustment of the pairing correction, we have recalculated the equilibrium energies of the nucleus, as well as the saddle point and the energy of the highest barrier, adding also the value of the coordinates q_1, q_2, q_3 and q_4 for both the ground state and the highest energy saddle. All energies are in MeV units.

The following notation is used in the tables:

- q_1: coordinate q_1 of GS.

- q_2: coordinate q_2 of GS.

- q_3: coordinate q_3 of GS.

- q_4: coordinate q_4 of GS.

- E_{eq}: energy of GS (MeV).

- q_{1s}: coordinate q_1 of the highest point saddle point.

- q_{2s}: coordinate q_2 of the highest point saddle point.

- q_{3s}: coordinate q_3 of the highest point saddle point.

- q_{4s}: coordinate q_4 of the highest point saddle point.

- E_{sad}: energy of the highest point saddle point (MeV).

- E_{bar}: difference of energies of the highest saddle point and GS (MeV).

Table B.1: Thorium

A	q_1	q_2	q_3	q_4	E_{eq}	q_{1s}	q_{2s}	q_{3s}	q_{4s}	E_{sad}	E_{bar}
200	0.07	-0.28	0	0	0.73	0	1.05	0	-0.03	2.48	1.75
202	0.05	-0.29	0	-0.01	0.71	0	1	0	0	2.83	2.12
204	0.07	0.21	0	0	0.29	0	1	0	-0.03	3.69	3.41
206	0.09	0.12	0	0	0.03	0	1	0	-0.03	4.86	4.84
208	0	-0.2	0	-0.01	-1.11	0.06	1	0.09	0	5.35	6.46
210	0.04	0.07	0	-0.01	-1.54	0.06	1	0.09	0	5.92	7.46
212	0	-0.07	0	0	-2.47	0	1	0.15	0.03	6.57	9.04
214	0	0.02	0	0	-3.2	0	1	0.12	0	7.53	10.73
216	0	0.03	0	0	-4.34	0	1	0.12	0	8.06	12.4
218	0	0.11	0	0	-1.91	0	1	0.12	0	8.57	10.48
220	0	0.13	0.13	0.01	0.17	0	1	0.12	-0.06	6.99	6.82
222	0	0.23	0.16	0.04	0.71	0	1	0.12	-0.03	6.53	5.82
224	0	0.25	0.15	0.04	1.53	0	1	0.12	-0.06	6.47	4.94
226	0	0.3	0	0.1	1.82	0	1	0.12	-0.06	6.27	4.45
228	0	0.35	0	0.11	1.38	0	1	0.12	-0.03	6.18	4.8
230	0	0.34	0	0.1	1.01	0	1	0.12	0	6.79	5.78
232	0	0.35	0	0.09	1.3	0	1	0.12	0	6.63	5.32
234	0	0.35	0	0.08	0.74	0	1.05	0.12	0	6.64	5.9
236	0	0.34	0	0.07	0.75	0	1.05	0.09	-0.06	6.97	6.21
238	0	0.33	0	0.05	0.62	0	1.05	0.09	-0.06	7.15	6.53
240	0	0.34	0	0.04	0.44	0	1.05	0.09	-0.06	7.48	7.04

Table B.2: Uranium

A	q_1	q_2	q_3	q_4	E_{eq}	q_{1s}	q_{2s}	q_{3s}	q_{4s}	E_{sad}	E_{bar}
220	0	0	0.03	0	-0.91	0.03	0.95	0.09	-0.03	5.6	6.51
222	0	0.12	0.14	0.01	0.74	0	0.95	0.12	-0.03	5.5	4.77
224	0	0.22	0.17	0.03	1.48	0	0.95	0.12	-0.06	5.06	3.58
226	0.07	0.39	0	0.06	1.49	0	0.95	0.09	-0.06	5.14	3.65
228	0.06	0.39	0	0.06	1.07	0	0.95	0.09	-0.03	4.91	3.84
230	0	0.36	0	0.1	0.98	0	1	0.12	-0.03	4.75	3.77
232	0	0.35	0	0.09	0.56	0	1	0.09	-0.03	5.15	4.58
234	0.04	0.37	0	0.06	0.59	0	1	0.12	0	5.28	4.69
236	0	0.35	0	0.07	0.03	0	1	0.09	0	5.54	5.51
238	0	0.35	0	0.06	-0.07	0	0.55	0	-0.06	5.66	5.74
240	0	0.34	0	0.06	-0.16	0.03	0.55	0	-0.03	6.05	6.21
242	0	0.34	0	0.04	-0.24	0	1	0.09	0.06	6.42	6.66
244	0	0.33	0	0.03	0.03	0	1	0.09	0.06	6.78	6.75
246	0	0.31	0	0.02	0.13	0.03	1	0.09	0	7.14	7.01
248	0	0.29	0	0.01	0.61	0.03	1	0.09	0	7.32	6.71

Table B.3: Plutonium

A	q_1	q_2	q_3	q_4	E_{eq}	q_{1s}	q_{2s}	q_{3s}	q_{4s}	E_{sad}	E_{bar}
222	0	0.07	0.11	0	-0.26	0.06	0.95	0.06	-0.03	3.97	4.23
224	0	0.19	0.13	0.03	1.29	0	0.95	0.09	-0.03	4.07	2.79
226	0	0.32	0	0.09	1.37	0	0.95	0.09	-0.03	3.7	2.33
228	0	0.32	0	0.08	1.27	0	0.95	0.09	-0.03	3.83	2.55
230	0	0.34	0	0.09	0.71	0	0.95	0.09	-0.06	3.74	3.03
232	0	0.35	0	0.09	0.21	0	0.95	0.09	-0.03	3.37	3.16
234	0	0.35	0	0.09	-0.2	0	0.55	0	-0.06	3.91	4.11
236	0	0.35	0	0.08	-0.12	0	0.55	0	-0.06	4.5	4.61
238	0	0.35	0	0.08	-0.71	0.03	0.55	0	-0.03	5.24	5.95
240	0	0.34	0	0.06	-0.81	0.06	0.55	0	-0.03	5.5	6.31
242	0	0.33	0	0.05	-0.92	0.06	0.55	0	-0.03	5.55	6.47
244	0	0.33	0	0.04	-1.03	0.06	0.55	0	0.03	5.65	6.68
246	0	0.32	0	0.03	-0.8	0.03	1	0.09	0	5.53	6.33
248	0	0.31	0	0.02	-0.71	0	0.95	0.06	0.03	5.8	6.51
250	0	0.3	0	0.02	-0.15	0	0.95	0.06	0.03	5.99	6.14

Table B.4: Curium

A	q_1	q_2	q_3	q_4	E_{eq}	q_{1s}	q_{2s}	q_{3s}	q_{4s}	E_{sad}	E_{bar}
224	0	0.08	0.12	0	0.11	0.03	0.95	0.06	-0.06	2.46	2.35
226	0.11	-0.35	0	-0.01	0.33	0	0.95	0.09	-0.03	2.55	2.22
228	0.11	-0.35	0	-0.02	0.24	0.09	0.9	0	0.03	2.71	2.48
230	0.11	-0.34	0	-0.01	0.21	0	0.9	0.09	-0.03	2.71	2.5
232	0.06	0.39	0	0.05	-0.02	0	0.6	0	-0.06	3.04	3.06
234	0.04	0.38	0	0.06	0.11	0	0.55	0	-0.06	3.14	3.03
236	0	0.35	0	0.08	-0.25	0	0.55	0	-0.03	3.92	4.17
238	0.05	0.37	0	0.03	-0.44	0	0.55	0	-0.06	4.63	5.07
240	0	0.35	0	0.07	-0.87	0.12	0.55	0	0.06	5.08	5.95
242	0	0.34	0	0.06	-1.01	0	0.6	0	-0.06	4.96	5.97
244	0	0.33	0	0.04	-1.22	0	0.6	0	-0.06	5.25	6.48
246	0	0.34	0	0.03	-1.43	0	0.6	0	-0.06	5.28	6.7
248	0	0.32	0	0.02	-1.22	0.03	0.6	0	0	4.91	6.13
250	0	0.31	0	0.02	-1.22	0.06	0.6	0	0.03	4.84	6.06
252	0	0.3	0	0.01	-0.74	0.06	1	0.06	-0.03	4.69	5.43

Table B.5: Californium

A	q_1	q_2	q_3	q_4	E_{eq}	q_{1s}	q_{2s}	q_{3s}	q_{4s}	E_{sad}	E_{bar}
238	0	0.34	0	0.07	-0.87	0.09	0.55	0.03	0.03	3.6	4.47
240	-0.02	0.35	0	0.05	-1.2	0.09	0.55	0	0.03	3.91	5.11
242	0	0.34	0	0.05	-1.69	0.09	0.55	0	0.03	4.22	5.9
244	0	0.33	0	0.04	-1.82	0	0.6	0	-0.06	4.39	6.21
246	0	0.33	0	0.04	-2.17	0	0.6	0	-0.03	4.52	6.69
248	0	0.33	0	0.03	-2.45	0	0.6	0	-0.03	4.57	7.02
250	0	0.32	0	0.02	-2.29	0.06	0.6	0	0	4.31	6.6
252	0	0.31	0	0.02	-2.33	0.06	0.6	0	0.06	4.11	6.44
254	0	0.29	0	0	-1.85	0.06	0.6	0	0.06	3.82	5.67
256	0	0.28	0	-0.01	-1.55	0.06	0.6	0	0.06	3.48	5.03
258	0	0.27	0	-0.02	-1.65	0.03	0.5	0	0.06	3.61	5.27
260	0	0.26	0	-0.03	-1.39	0	0.45	0.06	0.06	3.7	5.09

Table B.6: Fermium

A	q_1	q_2	q_3	q_4	E_{eq}	q_{1s}	q_{2s}	q_{3s}	q_{4s}	E_{sad}	E_{bar}
240	0.06	0.36	0	0.02	-0.72	0.09	0.55	0.03	0.06	3.07	3.79
242	0	0.34	0	0.04	-0.91	0	0.6	0	-0.03	3.27	4.18
244	0	0.33	0	0.04	-1.41	0.09	0.6	0.03	0.03	3.42	4.82
246	0	0.33	0	0.04	-1.55	0.09	0.55	0.06	0.06	3.63	5.19
248	0	0.32	0	0.03	-2	0.12	0.6	0	0.03	3.67	5.66
250	0	0.32	0	0.02	-2.38	0.12	0.6	0	0.06	3.7	6.08
252	0	0.31	0	0.01	-2.23	0.09	0.6	0	0.06	3.68	5.92
254	0	0.3	0	0	-2.45	0.09	0.6	0	0.06	3.4	5.85
256	0	0.28	0	0	-2.1	0.06	0.6	0	0.03	3	5.1
258	0	0.27	0	-0.02	-1.96	0.06	0.55	0.03	0.06	2.95	4.91
260	0	0.26	0	-0.03	-2.19	0.06	0.5	0	0.03	3.2	5.39
262	0	0.25	0	-0.04	-2.02	0.06	0.5	0	0.03	3.43	5.45

Table B.7: Nobelium

A	q_1	q_2	q_3	q_4	E_{eq}	q_{1s}	q_{2s}	q_{3s}	q_{4s}	E_{sad}	E_{bar}
242	0.01	0.33	0	0.03	-0.93	0.09	0.55	0	0.03	2.32	3.25
244	0	0.34	0	0.03	-1.36	0.09	0.6	0	0.06	2.47	3.83
246	0	0.33	0	0.03	-1.88	0.09	0.6	0	0.03	2.57	4.46
248	0	0.32	0	0.03	-2.04	0.12	0.55	0	0.03	2.89	4.93
250	0	0.32	0	0.02	-2.59	0.12	0.6	0	0.06	2.81	5.41
252	0	0.32	0	0.01	-3.04	0.12	0.6	0	0.06	2.92	5.96
254	0	0.31	0	0	-2.9	0.09	0.6	0	0.06	2.93	5.82
256	0	0.3	0	0	-3.2	0.09	0.55	0	0.06	2.83	6.04
258	0	0.28	0	-0.02	-2.92	0.09	0.5	0	0.03	2.9	5.82
260	0	0.28	0	-0.02	-2.81	0.06	0.5	0	0.03	2.95	5.76
262	0	0.26	0	-0.03	-3.1	0	0.45	0.09	0.03	3.22	6.32
264	0	0.25	0	-0.04	-2.97	0.09	0.45	0	0	3.37	6.34

Table B.8: Rutherfordium

A	q_1	q_2	q_3	q_4	E_{eq}	q_{1s}	q_{2s}	q_{3s}	q_{4s}	E_{sad}	E_{bar}
250	0	0.31	0	0.02	-2.13	0.12	0.5	0	0.03	1.83	3.97
252	0	0.31	0	0.01	-2.77	0.09	0.5	0.06	0.03	1.82	4.59
254	0	0.31	0	0	-3.36	0.12	0.6	0	0.06	1.92	5.28
256	0	0.3	0	0	-3.15	0.06	0.6	0	0.06	2.06	5.21
258	0	0.29	0	-0.01	-3.62	0.06	0.5	0	0.06	2	5.62
260	0	0.28	0	-0.02	-3.45	0.09	0.5	0	0.03	1.93	5.38
262	0	0.27	0	-0.03	-3.36	0	0.45	0.03	0.06	2.37	5.73
264	0	0.26	0	-0.04	-3.76	0.09	0.45	0	0	2.6	6.36
266	0	0.25	0	-0.05	-3.7	0.09	0.45	0	0	2.74	6.44
268	0	0.24	0	-0.05	-3.1	0.09	0.45	0	0	2.74	5.84
270	0	0.21	0	-0.05	-2.53	0.06	0.5	0	0.03	2.69	5.23
272	0	0.19	0	-0.04	-1.85	0.09	0.45	0.03	0	2.73	4.58
274	0	0.16	0	-0.01	-1.97	0	0.45	0	0.03	2.69	4.66
276	0	0.14	0	-0.02	-2.2	0	0.3	0.03	-0.03	2.64	4.84
278	0	0.12	0	-0.03	-2.13	0	0.35	0	0	3.12	5.24
280	0	0.1	0	-0.03	-1.87	0	0.35	0	0	3.36	5.23
282	0	-0.1	0	-0.01	-1.85	0	0.35	0	0	3.63	5.48
284	0	-0.04	0	0	-1.71	0	0.35	0	0	3.75	5.46

Table B.9: Seaborgium

A	q_1	q_2	q_3	q_4	E_{eq}	q_{1s}	q_{2s}	q_{3s}	q_{4s}	E_{sad}	E_{bar}
252	0	0.29	0	0.01	-2.29	0.12	0.5	0	0.03	1	3.29
254	0	0.3	0	0	-2.99	0.12	0.5	0.03	0.03	1.11	4.09
256	0	0.29	0	-0.01	-3.69	0	0.45	0.06	0.06	1.32	5.01
258	0	0.29	0	-0.02	-3.5	0	0.45	0	0.06	1.41	4.91
260	0	0.28	0	-0.02	-4.17	0	0.45	0.06	0.06	1.83	6
262	0	0.27	0	-0.03	-4.21	0	0.45	0	0.06	1.73	5.94
264	0	0.26	0	-0.04	-4.26	0	0.45	0.03	0.06	2.24	6.5
266	0	0.25	0	-0.05	-4.82	0.12	0.45	0	-0.03	2.3	7.11
268	0	0.25	0	-0.06	-4.87	0.12	0.45	0	-0.03	2.37	7.23
270	0	0.24	0	-0.06	-4.26	0.12	0.45	0	-0.03	2.49	6.74
272	0	0.22	0	-0.06	-3.59	0.09	0.45	0	0	2.52	6.11
274	0	0.19	0	-0.04	-2.69	0.09	0.45	0	0	2.56	5.25
276	0	0.16	0	-0.03	-2.77	0	0.45	0	0.03	2.36	5.13
278	0	0.13	0	-0.02	-2.96	0	0.35	0.03	-0.03	2.8	5.76
280	0	0.12	0	-0.03	-2.92	0	0.35	0	-0.03	3.27	6.2
282	0	0.09	0	-0.03	-2.68	0	0.35	0	0	3.61	6.29
284	0	-0.09	0	-0.01	-2.62	0.15	0.35	0	0.03	3.83	6.45
286	0	-0.04	0.01	-0.01	-2.58	0.15	0.35	0	0	3.99	6.57

Table B.10: Hassium

A	q_1	q_2	q_3	q_4	E_{eq}	q_{1s}	q_{2s}	q_{3s}	q_{4s}	E_{sad}	E_{bar}
254	0	0.29	0	0	-2.07	0.09	0.45	0.06	0	0.47	2.54
256	0	0.3	0	0	-2.79	0.09	0.45	0	0	0.49	3.28
258	0	0.29	0	-0.02	-3.54	0.09	0.5	0	0.03	0.7	4.24
260	0	0.28	0	-0.02	-3.3	0.09	0.45	0	0	1.1	4.4
262	0	0.27	0	-0.03	-4.02	0.09	0.45	0.03	0	1.34	5.36
264	0	0.26	0	-0.03	-4.22	0.12	0.45	0	0	1.44	5.67
266	0	0.25	0	-0.04	-4.36	0.12	0.45	0	0	1.84	6.19
268	0	0.24	0	-0.05	-5.04	0.12	0.45	0	-0.03	1.82	6.85
270	0	0.24	0	-0.06	-5.22	0.12	0.45	0.03	-0.03	1.97	7.19
272	0	0.22	0	-0.07	-4.76	0.12	0.45	0.03	-0.03	2.11	6.87
274	0	0.21	0	-0.07	-4.28	0	0.4	0.09	0	2.25	6.52
276	0	0.19	0	-0.06	-3.39	0	0.4	0.09	0	2.63	6.02
278	0	0.15	0	-0.02	-3.52	0	0.4	0.06	0	2.47	6
280	0	0.13	0	-0.02	-3.86	0	0.35	0	0	2.66	6.52
282	0	0.11	0	-0.03	-3.87	0	0.35	0	-0.03	3.1	6.97
284	0	0.09	0	-0.04	-3.76	0	0.35	0	-0.03	3.41	7.16
286	0	0.05	0	-0.01	-3.63	0.15	0.35	0	0.03	3.4	7.02
288	0	-0.02	0	0	-3.74	0.15	0.35	0	0.03	3.56	7.3

Table B.11: Darmstadtium

A	q_1	q_2	q_3	q_4	E_{eq}	q_{1s}	q_{2s}	q_{3s}	q_{4s}	E_{sad}	E_{bar}
262	0	0.27	0	-0.02	-2.87	0.09	0.45	0	0	0.46	3.33
264	0	0.26	0	-0.02	-3.68	0.09	0.45	0.03	0	0.75	4.42
266	0	0.25	0	-0.03	-3.99	0.12	0.45	0	0	0.68	4.67
268	0	0.24	0	-0.04	-4	0.12	0.45	0	0	1.15	5.15
270	0	0.24	0	-0.06	-4.75	0	0.4	0.09	0	1.4	6.15
272	0	0.23	0	-0.07	-4.97	0.09	0.4	0	-0.03	1.55	6.52
274	0	0.22	0	-0.07	-4.53	0.12	0.4	0	-0.03	1.86	6.39
276	0	0.19	0	-0.06	-4.17	0.09	0.4	0	-0.03	2	6.17
278	0.04	-0.05	0	0	-4.23	0	0.4	0.03	0	2.24	6.47
280	0.03	-0.09	0	0.01	-4.58	0	0.35	0	-0.03	2.3	6.88
282	0	0.1	0	-0.01	-5.03	0.15	0.35	0	0.03	2.47	7.5
284	0	0.09	0	-0.01	-4.93	0.15	0.35	0	0.03	2.35	7.28
286	0	-0.07	0	0	-5	0.15	0.35	0	0.03	2.52	7.52
288	0	0	0	0	-5.19	0.15	0.35	0	0.03	2.27	7.46
290	0	-0.02	0	0	-5.13	0.15	0.35	0	0.03	2.43	7.56
292	0	0	0	0	-4.57	0.15	0.35	0	0	2.56	7.13
294	0	0	0	0	-3.74	0.15	0.35	0	0	2.63	6.37
296	0	0	0	0	-1.75	0.15	0.35	0	0	2.6	4.35

Table B.12: Copernicium

A	q_1	q_2	q_3	q_4	E_{eq}	q_{1s}	q_{2s}	q_{3s}	q_{4s}	E_{sad}	E_{bar}
264	0	0.28	0	-0.02	-2.47	0.09	0.45	0	0	0.16	2.63
266	0	0.26	0	-0.03	-3.33	0.09	0.45	0	0	0.45	3.78
268	0	0.24	0	-0.04	-3.73	0.12	0.45	0	0	0.4	4.13
270	0	0.24	0	-0.05	-3.71	0.12	0.45	0	0	0.92	4.62
272	0	0.23	0	-0.06	-4.52	0	0.4	0.09	0	1.15	5.67
274	0	0.22	0	-0.07	-4.79	0.09	0.4	0	-0.03	1.31	6.09
276	0	0	0	0	-4.88	0	0.4	0.09	0	1.67	6.55
278	0	0.01	0	0	-5.64	0.09	0.4	0	-0.03	1.77	7.41
280	0	0.07	0	0.02	-5.54	0	0.4	0.03	0	1.99	7.53
282	0	-0.1	0	0.02	-5.75	0.15	0.35	0	0	1.98	7.73
284	0	0.09	0	-0.01	-6.08	0.15	0.35	0	0.03	2.08	8.16
286	0.02	0.04	0	0	-6.11	0.15	0.35	0	0.03	1.97	8.08
288	0	0	0	0	-6.54	0.15	0.35	0	0	2.09	8.63
290	0	0	0	0	-6.78	0.15	0.35	0	0.03	1.9	8.69
292	0	-0.01	0	0	-6.7	0.15	0.35	0	0.03	2.07	8.77
294	0	0	0	0	-6.12	0.15	0.35	0	0	2.15	8.27
296	0	0	0	0	-5.26	0.15	0.35	0	0	2.22	7.48
298	0	0	0	0	-3.29	0.15	0.35	0	0	2.21	5.5

Table B.13: Flerovium

A	q_1	q_2	q_3	q_4	E_{eq}	q_{1s}	q_{2s}	q_{3s}	q_{4s}	E_{sad}	E_{bar}
266	0	0.22	0	-0.01	-2.16	0	0.4	0	0.03	-0.47	1.69
268	0	0.23	0	-0.02	-2.79	0.03	0.45	0	0.03	-0.12	2.67
270	0	0.22	0	-0.02	-3.25	0.15	0.45	0	0	-0.07	3.18
272	0	0.21	0	-0.04	-3.06	0	0.45	0.03	0.03	0.45	3.51
274	0	0.21	0	-0.05	-3.78	0.12	0.45	0	-0.03	0.49	4.28
276	0	0	0	0	-4.74	0.12	0.45	0	-0.03	0.57	5.3
278	0	0	0	0	-5.35	0.18	0.4	0	0	1.03	6.38
280	0	0.03	0	0.01	-6.02	0.18	0.4	0	0	1.63	7.66
282	0	0.07	0	0.02	-5.96	0	0.4	0	0	1.72	7.68
284	0.02	-0.09	0	0.01	-6.13	0	0.4	0.03	0	1.59	7.72
286	0	0.1	0	-0.01	-6.44	0	0.4	0	0	1.6	8.04
288	0.02	0.05	0	0	-6.39	0	0.4	0	0	1.23	7.62
290	0	-0.02	0	0	-6.71	0.15	0.35	0	0	1.4	8.11
292	0	0	0	0	-6.89	0	0.4	0.03	0	1.2	8.1
294	0	-0.01	0	0	-6.81	0	0.4	0	0	1.42	8.23
296	0	0	0	0	-6.16	0.15	0.35	0	0	1.48	7.65
298	0	0	0	0	-5.26	0	0.4	0	0	1.57	6.83
300	0	0	0	0	-3.29	0.15	0.4	0	0.03	1.7	4.99

Table B.14: Livermorium

A	q_1	q_2	q_3	q_4	E_{eq}	q_{1s}	q_{2s}	q_{3s}	q_{4s}	E_{sad}	E_{bar}
274	0.01	0.19	0	-0.03	-2.67	0	0.45	0	0.03	-0.28	2.39
276	0	0.01	0	0	-3.97	0.12	0.45	0	-0.03	-0.17	3.8
278	0	0.01	0	0	-5.68	0.18	0.4	0	0	0.07	5.74
280	0	0	0	0	-6.21	0.21	0.4	0	0	0.35	6.56
282	0	0.02	0	0	-6.82	0.21	0.4	0	0.03	0.74	7.56
284	0	0.08	0	0.01	-6.78	0.21	0.4	0	0.03	0.8	7.57
286	0.03	0.09	0	0	-6.79	0.21	0.4	0	0.03	1	7.79
288	0.03	-0.05	0	0	-7.03	0	0.4	0	0	1.11	8.14
290	0	0.06	0	-0.01	-7.03	0	0.4	0	0	0.7	7.73
292	0	0.04	0	-0.01	-7.13	0	0.4	0	0	0.69	7.82
294	0	0.01	0	0	-7.2	0	0.4	0	0	0.57	7.77
296	0	-0.01	0	0	-7.02	0	0.4	0	0	0.8	7.82
298	0	0.01	0	0	-6.2	0	0.4	0	0	0.76	6.96
300	0	0	0	0	-5.24	0	0.4	0	-0.03	0.97	6.21
302	0	0.01	0	0	-3.33	0.03	0.4	0	-0.03	1.29	4.62
304	0	0.01	0	0	-1.01	0.03	0.4	0	0	1.32	2.33
306	0	-0.25	0	-0.02	0.07	0.12	0.35	0	0.06	1.08	1.01
308	0	-0.26	0	-0.01	0.73	0.15	0.25	0	0	1.44	0.71

Table B.15: Oganesson

A	q_1	q_2	q_3	q_4	E_{eq}	q_{1s}	q_{2s}	q_{3s}	q_{4s}	E_{sad}	E_{bar}
276	0	0.13	0	-0.01	-2.48	0	0.45	0	0.03	-1	1.48
278	0	0.07	0	0	-3.18	0	0.45	0	0.03	-0.74	2.44
280	0	0	0	0	-4.9	0	0.45	0	0.03	-0.77	4.13
282	0	-0.01	0	0	-5.41	0.21	0.4	0	0	-0.35	5.05
284	0	0	0	0	-6.01	0.21	0.4	0	0.03	-0.04	5.97
286	0	0.1	0	0.02	-6.32	0.21	0.4	0.03	0.03	0.02	6.34
288	0	-0.12	0	0.01	-6.4	0.21	0.4	0	0.03	0.24	6.64
290	0	0.1	0	-0.01	-6.64	0	0.4	0	0	0.63	7.27
292	0	-0.1	0	0.01	-6.47	0	0.4	0	0	0.22	6.69
294	0.03	0.04	0	0.01	-6.41	0	0.4	0	0	0.17	6.58
296	0	-0.02	0	0	-6.43	0	0.4	0	0	0.05	6.49
298	0	-0.02	0	0	-6.31	0	0.4	0	0	0.3	6.62
300	0	0	0	0	-5.41	0	0.4	0	0	0.24	5.65
302	0	0	0	0	-4.46	0	0.4	0	0	0.45	4.91
304	0	0	0	0	-2.58	0	0.4	0	0	0.85	3.43
306	0	-0.24	0	0	-0.89	0.03	0.4	0	0	0.92	1.82
308	0	-0.26	0	-0.02	-0.13	0.03	0.4	0	0.03	0.87	1
310	0	-0.27	0	-0.02	0.48	0.09	0.1	0	0	0.95	0.47

Table B.16: Unbinilium

A	q_1	q_2	q_3	q_4	E_{eq}	q_{1s}	q_{2s}	q_{3s}	q_{4s}	E_{sad}	E_{bar}
278	0.03	0.16	0	-0.02	-1.7	0	0.45	0	0.03	-1.67	0.03
280	0.02	0.04	0	0	-2.42	0	0.45	0.03	0.03	-1.4	1.02
282	0	0.02	0	0	-4.05	0	0.45	0.03	0.03	-1.43	2.62
284	0	-0.01	0	0	-4.51	0	0.45	0	0.03	-1.29	3.22
286	0	0.02	0	0	-5.26	0	0.45	0.03	0.03	-1.28	3.98
288	0.03	-0.04	0	0	-5.41	0.21	0.4	0.06	0.03	-1.24	4.17
290	0	-0.16	0	0.01	-5.82	0.21	0.4	0	0.03	-0.93	4.89
292	0.03	-0.05	0	0	-5.68	0.21	0.4	0.06	0.03	-0.16	5.52
294	0	-0.12	0	0	-5.73	0	0.4	0	0	-0.26	5.47
296	0	-0.06	0	0	-5.63	0	0.4	0	0	-0.32	5.31
298	0	-0.01	0	0	-5.65	0	0.4	0	0	-0.36	5.29
300	0	-0.02	0	0	-5.56	0.15	0.35	0	0.03	0	5.56
302	0	0	0	0	-4.64	0.18	0.35	0	0.03	0.17	4.8
304	0	0	0	0	-3.7	0.12	0.35	0	0.09	0.12	3.81
306	0	0	-0.02	0	-1.89	0	0.4	0	-0.03	0.34	2.22
308	0	-0.25	0	-0.01	-1.11	0.03	0.4	0	0	0.44	1.56
310	0	-0.26	0	-0.02	-0.41	0.12	0.4	0	0.09	0.34	0.75
312	0.11	0.38	0	0.07	0.14	0.03	0.4	0	-0.03	0.29	0.15

C Appendix: Search for minima, maxima and saddle points in multidimensional deformation space

In calculating the energy evolution of spontaneous fission in $N = 4$ dimensional deformation space, we have implemented a simple but very effective method for finding maxima and minima along fission paths. The energy as a function of the coordinates considered is determined at discrete, equidistant grid points. To find the energy maximum or minimum, we compare the energy at a given point on this grid with the 2^N energy values in its immediate neighbourhood. If all neighbouring configurations have a higher energy than the given point, we have a local minimum. If the opposite is true, it means that the point under consideration is a local maximum. If the point in question is neither a minimum nor a maximum, it is probably a saddle point. To verify this explicitly, we apply a very simple test that simulates the filling of a minimum (or strictly speaking a splitting valley) with water. The water level rises until it overflows at a certain point, what proves that this suspected point is truly the interesting saddle point located behind the potential energy well corresponding to the ground state or isomeric configuration. This is schematically shown in the graph C.1 in the one dimensional case.
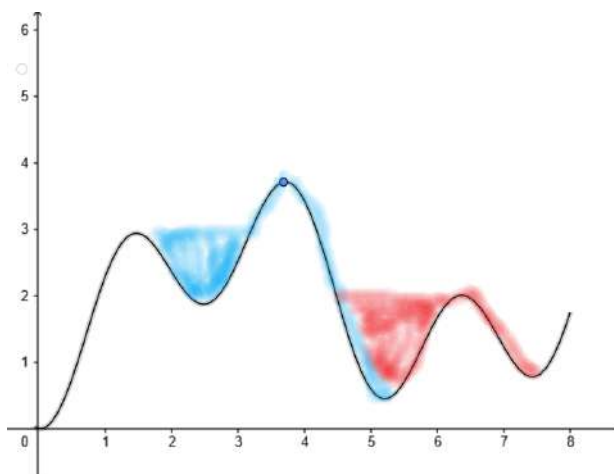

Figure C.1: 1D example of the water-flow method.

D   References

References

[1] O. Hahn, F. Straßmann, Naturwiss, **27**, 11, (1939).

[2] L. Meitner, O. R. Frisch, Nature **143**, 239 (1939).

[3] G. N. Flerov, K. A. Petrzhak, Phys. Rev. **58**, 89 (1940).

[4] N. Bohr, J. A. Wheeler, Phys. Rev. **56**, 426 (1939).

[5] W. J. Swiatecki, Phys. Rev. **100**, 937 (1955).

[6] K. Pomorski, M. Warda, A. Zdeb, Phys. Scr. **90**, 114013 (2015).

[7] K. Pomorski, A. Dobrowolski, B. Nerlo-Pomorska, M. Warda, J. Bartel, Z. Xiao, Y. Chen, L. Liu, J. L. Tian, X. Diao, Eur. Phys. J. A **58**, 77 (2022).

[8] K. Pomorski, J. Dudek, Phys. Rev. C **67**, 044316 (2003).

[9] A. Baran, A. Staszczak, W. Nazarewicz, Int. Journ. Mod. Phys. E **20**, 02 (2011).

[10] J. Sadhukhan, K. Mazurek, A. Baran, J. Dobaczewski, W. Nazarewicz, J. A. Sheikh, Phys. Rev. C **88**, 064314 (2013).

[11] R. Rodríguez-Guzmán, L. M. Robledo, Eur. Phys. J. A **53**, 245 (2017).

[12] R. Rodríguez-Guzmán, L. M. Robledo, Phys. Rev. C **98**, 034308 (2018).

[13] S. A. Giuliani, L. M. Robledo, Phys. Lett. **787**, 134 (2018).

[14] S. G. Nilsson, C. F. Tsang, A. Sobiczewski, Z. Szymański, S. Wycech, C. Gustafson, I. L. Lamm, P. Möller, B. Nilsson, Nucl. Phys. A **131**, 1 (1969).

[15] M. Brack, J. Damgaard, A. S. Jensen, H. C. Pauli, V. M. Strutinsky, C. Y. Wong, Rev. Mod. Phys. **44**, 320 (1972).

[16] A. Góźdź, K. Pomorski, M. Brack, E. Werner, Nucl. Phys. A **442**, 26 (1985).

[17] K. Pomorski, B. Nerlo-Pomorska, A. Dobrowolski, J. Bartel, C. M. Petrache, Eur. Phys. Journ. A **56**, 107 (2020).

[18] K.T.R. Davies, A.J. Sierk, J.R. Nix, Phys. Rev. C **13**, 2385 (1976).

[19] J. Bartel, B. Nerlo-Pomorska, K. Pomorski, A.Dobrowolski, Comp. Phys. Comm. **241**, 139 (2019).

[20] G. Wentzel, Zeit. Phys. **38**, 518 (1926).

[21] H. A. Kramers, Zeit. Phys. **39**, 828 (1926).

[22] L. Brillouin, Comp. Rend. Acad. Scien. **183**, 24 (1926).

[23] P. Müller, A. J. Sierk, T. Ichikawa, A. Iwamoto, M. Mumpower, Phys. Rev. C **91**, 024310 (2015).

[24] C. F. v. Weizsäcker, Z. Phys. **96** (1935) 431.

[25] H. A. Bethe, F. Bacher, Rev. Mod. Phys **8** (1936) 426.

[26] D.L. Hill and J. A. Wheeler, Phys. Rev. **89** (1953) 1102.

[27] W. D. Myeres, W. Swiatecki, Ark. Phys **36** (1967) 343.

[28] W. D. Myeres, W. Swiatecki, Ann. Phys. **55** (1970) 395.

[29] W. D. Myeres, W. Swiatecki, Nucl. Phys. **A81** (1966) 1.

[30] H. V. Groote and E. Hilf, Nucl. Phys. **129** (1969) 513.

[31] A. J. Sierk, Phys. Rev. **33** (1986) 2039.

[32] K. Pomorski, J. Dudek, Phys. rev. **67** 044316 (2003.)

[33] M. S. Antony, Nuclide Chart 2002, Strasbourg 2002, Impresions.

[34] P. Möller, W. D. Myers W. J. Swiatecki, J. Treiner, At. Data Nucl. Data Tables **39** (1988) 225.

[35] W. D. Myers W. J. Swiatecki, Nucl. Phys. A **601**, 141 (1996).

[36] M. Brack, J. Damgaard, A.S. Jensen, H. C. Pauli, V. M. Strutinsky, C. Y. Wong, Rev. Mod. Phys. **44** (1972) 320.

[37] K. T. R. Davies, J. R. Nix, Phys. Rev. **14** (1976) 1977.

[38] W. J. Swiatecki, Proceedings of the Second International Conference on Nuclidic Masses, Vienna, 1963 (Springer, Vienna)

[39] V. M. Strutinsky, Sov. J. Nucl. Phys. **3** (1966) 449; Nucl. Phys. **A95** (1967) 420.

[40] P. Möller, J. R Nix, Atomic Data and Nuclear Data Tables **59** 185-381 (1995)

[41] P. Möller, J. R. Nix, Atomic Data and Nuclear Data Tables **59**, 185 (1995).

[42] S. Ćwiok, J. Dobaczewski, P. H. Heenen, P. Magierski, W. Nazarewicz, Nucl. Phys. A **611**, 211 (1996).

[43] S. Piłat, K. Pomorski, A. Staszczak, Zeit. Phys. A **332**, 259 (1989).

[44] R. A. Gherghescu, J Skalski, Z Patyk, A Sobiczewski, Nucl. Phys. A **651**, 237 (1999).

[45] A. Góźdź, K. Pomorski, Nucl. Phys. A **451**, 1 (1986).

[46] K. Pomorski, B. Nerlo-Pomorska, J. Bartel, Int. Journ., Mod. Phys. E **16**, 566 (2007).

[47] Z. Łojewski, A. Staszczak, Nucl. Phys. A **657**, 134 (1999).

[48] Z. Łojewski, A. Baran, K. Pomorski, Acta Phys. Pol. B **34**, 1801 (2003).

[49] J. Randrup, S. E. Larsson, P. Möller, S. G. Nilsson, K. Pomorski, A. Sobiczewski, Phys. Rev. C **13**, 229 (1976).

[50] W. Ritz, J. Math. **135**, 1 (1909).

[51] A. Baran, Phys. Lett. B **76**, 8 (1978).

[52] A. Baran, K. Pomorski, A. Łukasiak, A. Sobiczewski, Nucl. Phys. A **361**, 83 (1981).

[53] R. Smolańczuk, J. Skalski, A. Sobiczewski, Phys. Rev. C **52**, 1871 (1995).

[54] NUDAT Data Base 2021.https://www.nndc.bnl.gov/nudat3

[55] G. N. Smirenkin, IAEA Report No. INDC(CCP)-359, Vienna, 1993.

[56] M. Warda, J. L. Egido, Phys. Rev. C **86**, 014322 (2012).

[57] K. Pomorski, A. Dobrowolski, B. Nerlo-Pomorska, M. Warda, J. Bartel, Z. G. Xiao, Y. J. Chen, L. L. Liu, J.-L. Tian, X. Y. Diao , Eur. Phys. Journ. A **58**, 77 (2022).

[58] A. Góźdź, K. Pomorski, M. Brack, E. Werner, Nucl. Phys. A **442**, 26 (1985).

[59] L. L. Liu, Y. J. Chen, X. Z. Wu, Z. X. Li, Z. G. Ge, K. Pomorski, Phys. Rev. C **103**, 044601 (2021).

[60] K. Pomorski, J. M. Blanco, P. V. Kostryukov, A. Dobrowolski, B. Nerlo-Pomorska, M. Warda, Z. G. Xiao, Y. J. Chen, L. L. Liu, J. L. Tian, X. Y. Diao, Q. H. Wu, Chin. Phys. C **45**, 054109 (2021).

[61] P. Jachimowicz, M. Kowal, J. Skalski, Phys. Rev. C **101**, 014311 (2020).